Impact of Non-associativity of Soil Plastic Flow on Stability of Geotechnical Structures

by

Yeon Sam Kim

A dissertation submitted in partial fulfillment
of the requirements for the degree of
Doctor of Philosophy
(Civil Engineering)
in the University of Michigan
2026

Doctoral Committee:

Professor Radoslaw L. Michalowski, Chair
Assistant Professor Jonathan B. Estrada
Assistant Professor Fernando E. Garcia
Professor Roman D. Hryciw

Yeon Sam Kim

yeonsam@umich.edu

ORCID iD: 0009-0001-2877-2577

© Yeon Sam Kim 2026

Dedication

To my two families,
the Kim and Cheong families

Acknowledgements

I owe my deepest gratitude to my advisor, Professor Radoslaw L. Michalowski, for guiding me through this Ph.D. with a combination of intellectual rigor and continuous support. From the earliest sketches of this project to the final revisions, Prof. Michalowski consistently challenged me to pursue clarity over convenience and depth over speed. What I appreciated the most was not only the sharpness of scientific instincts, but also the seriousness with which he treated the craft of research: how to ask a meaningful question, how to make an argument that holds up, how to hold my work to a higher standard. That training has shaped how I think far beyond the scope of this dissertation. I will always remember Prof. Michalowski's patience throughout this journey. He gave me the time and space to struggle productively. Even when my progress was slow, he remained calm, thoughtful, and fully engaged.

I am also sincerely grateful to my committee members serving on my dissertation committee and for their kindness and support throughout my time in the program. Beyond formal roles, each of you made a point to create space for me to grow with confidence. Prof. Roman Hryciw's insightful teaching sharpened how I think about foundation engineering. Prof. Estéfan Garcia always made time to check in and offer encouragement. Prof. Jonathan Estrada's perspective of continuum mechanics helped me keep the broader context in view.

To my friends, I'm grateful for the late-night check-ins and the casual "you've got this" that somehow carried real weight. In particular, I want to thank JB, Lei, Austin, Daniel, Jacob, Rich, Jason, Ben, Iason, Deba, Songjie, Tianming, Minghui, and all DPMers including John, Juhyeon, and Gunwoo.

My deepest personal thanks go to my love, Anna, who has been my anchor throughout this journey and is soon becoming my wife. Thank you for believing in me. I'm also profoundly grateful to my two families, the Kim and Cheong families, for warmth, generosity, and love. To my parents and family, thank you for your steady support and for trusting me to find my own path. To my future in-laws, thank you for welcoming me so fully and for treating me as family long before I had a right to claim that word. I am very lucky to have both homes in two countries.

Finally, financial support provided by the Department of Civil and Environmental Engineering at the University of Michigan and the National Science Foundation (CMMI-1901582) is gratefully acknowledged.

Table of Contents

Dedication ii

Acknowledgements iii

List of Tables vi

List of Figures viii

Abstract xii

Chapter 1 Introduction 1

1.1 General Background 1

1.2 Non-associativity of plastic flow in soils 6

Chapter 2 Objectives 13

Chapter 3 Plasticity of Geomaterials 14

3.1 Stress-strain behavior of soils and rocks 14

3.2 Yield criteria and flow rules 21

3.2.1 Statics of the limit state 22

3.2.2 Kinematics of the limit state 25

3.3 Plasticity models 29

Chapter 4 Limit Analysis 41

4.1 Admissible stress fields and mechanisms 41

4.2 Theorems of limit analysis 44

4.3 Limit analysis for non-associative soils and rock masses 48

Chapter 5 Impact of Non-associativity on Stability of Geotechnical Structures 63

5.1 Slopes 63

5.1.1 Plane strain analysis 64
5.1.2 Spatial collapse in slopes 68
5.1.3 Impact of non-associativity on stability of slopes 73
5.2 Loads on retaining structures 74
5.2.1 Active load 75
5.2.2 Passive load 80
5.2.3 Impact of non-associativity on retaining wall loads 85
5.3 Shallow foundations 95
5.3.1 Translational mechanisms 95
5.3.2 Rotational and mixed mechanisms 99
5.3.3 Combined loads on footings 102
5.3.4 Impact of non-associativity on bearing capacity of footings 106
5.4 Discussion of impact 109
Chapter 6 Summary and Conclusions 111
Appendices 115
Bibliography 117

List of Tables

Table 3.1: Internal friction angle and dilation angle for Sacramento River sand specimens subjected to different confinements (all values were calculated from the raw test data of Lee and Seed 1967) 16

Table 3.2: Internal friction angle and dilation angle for Antelope Valley sand specimens subjected to different confinements (all values were calculated from the raw test data of Lade 2016) 18

Table 3.3: Predicted and observed rupture angle for Amarelo País granite specimens at different stress states (all values were calculated from the raw test data of Arzúa and Alejano 2013) 20

Table 5.1: Non-associativity impact factor λ_F for factor of safety of slopes calculated for different internal friction and dilation angles 74

Table 5.2: Active earth pressure coefficient K_a for different internal friction angle ϕ and soil-wall interface friction angle ϕ_w 79

Table 5.3: Passive earth pressure coefficient K_p for different internal friction angle ϕ, wall angle α, backfill inclination angle β, and soil-wall interface friction angle ϕ_w 84

Table 5.4: Non-associativity impact factor λ_a for retaining wall active loads calculated for different internal friction and dilation angles 86

Table 5.5: Active earth pressure coefficient K_a for different dilation angle ϑ, friction angle ϕ, wall angle α, backfill inclination angle β, and soil-wall interface friction angle ϕ_w 87

Table 5.6: Non-associativity impact factor λ_p for retaining wall passive loads calculated using the Coulomb's method for different internal friction and dilation angles 89

Table 5.7: Non-associativity impact factor λ_p for retaining wall passive loads calculated using the multi-block mechanism for different internal friction and dilation angles 90

Table 5.8: Passive earth pressure coefficient K_p obtained by Coulomb's analysis for different dilation angle ϑ, internal friction angle ϕ, wall angle α, backfill inclination angle β, and soil-wall interface friction angle ϕ_w 91

Table 5.9: Passive earth pressure coefficient K_p obtained by the multi-block mechanism for different dilation angle ϑ, internal friction angle ϕ, wall angle α, backfill inclination angle β, and soil-wall interface friction angle ϕ_w 93

Table 5.10: Bearing capacity factor N_c for footings subjected to a vertical load calculated using multi-block mechanism for different internal friction angles and dilation angles..... 106

Table 5.11: Bearing capacity factor N_q for footings subjected to a vertical load calculated using multi-block mechanism for different internal friction angles and dilation angles..... 107

Table 5.12: Bearing capacity factor N_γ for footings subjected to a vertical load calculated using multi-block mechanism for different internal friction angles and dilation angles..... 107

List of Figures

Figure 1.1: Tresca yield criterion in (a) $\sigma_n - \tau$ space, and (b) in the Haigh-Westergaard space .. 2

Figure 1.2: Huber-Mises yield criterion and Tresca yield criterion in the Haigh-Westergaard space (after Huber 1904 and Von Mises 1913) 3

Figure 1.3: Schematic of punch indentation into a plastic material (after Prandtl 1920) 4

Figure 1.4: Rigid footing subjected to an inclined eccentric load (Sloan 2013)..... 5

Figure 1.5: A schematic of bearing capacity problem with non-associative soil: stress characteristics (dashed lines) and velocity characteristics (solid lines) for incompressible soil (from Davis 1968)..... 7

Figure 1.6: (a) Associated modified Cam clay model, (b) associated original Cam clay model, and (c) non-associated flow rule – Cam clay yield criterion and modified Cam clay model for plastic potential (Banerjee and Stipho 1978) 8

Figure 1.7: (a) Porewater pressure observation and predictions for a normally consolidated specimen and (b) Observed and predicted undrained stress paths in compression and extension tests for normally consolidated samples (Banerjee and Stipho 1978) 9

Figure 1.8: Factor of safety versus ϑ chart developed by SSRFEM and FELA (Chen et al. 2020) 10

Figure 1.9: Geometry and boundary conditions with 99 triangular finite element mesh (after Chaaba et al. 2010) 11

Figure 1.10: Variation of the bearing capacity factor N_c with dilatancy angle (Chaaba et al. 2010) 12

Figure 3.1: Stress-strain-volume change data for Sacramento River sand (after Lee and Seed 1967) 15

Figure 3.2: Results of drained triaxial compression tests on dense Antelope Valley sand (Lade 2016)..... 17

Figure 3.3: Complete stress-strain curves for Amarelo País granite (from Arzúa and Alejano 2013)..... 19

Figure 3.4: Hoek-Brown yield criterion from Arzúa and Alejano (2013) (black solid curve), superimposed with stress states extracted from the raw test data of Arzúa and Alejano (2013).. 20

Figure 3.5: Yield function and plastic strain rate..... 21

Figure 3.6: (a) Mohr-Coulomb failure criterion, (b) orientation of major principal stress in the physical space, and (c) Mohr-Coulomb failure criterion in the Haigh-Westergaard space..... 23

Figure 3.7: Yield function and plastic strain rate for non-associative flow rule..... 26

Figure 3.8: 1-D stress-strain relationship of elastic-perfectly plastic model 30

Figure 3.9: 1-D stress-strain relationship for elastic-plastic model with hardening 33

Figure 3.10: Yield surface in Cam clay model 34

Figure 3.11: Conventional triaxial compression test for lightly preconsolidated clay using Cam clay model: (a) yield surfaces on plane $p'-q$, (b) deviatoric stress-strain response, (c) relationship between specific volume v and effective mean stress p', and (d) relationship between specific volume v and deviatoric strain ε_q 39

Figure 3.12: Conventional triaxial compression test for overconsolidated clay using Cam clay model: (a) yield surfaces on plane $p'-q$, (b) deviatoric stress-strain response, (c) relationship between specific volume v and effective mean stress p', and (d) relationship between specific volume v and deviatoric strain ε_q 40

Figure 4.1: (a) Admissible plastic stress field for a shallow footing problem, and (b) plastic stress states in the respective regions..... 42

Figure 4.2: (a) Admissible mechanism of a shallow foundation problem, and (b) hodograph 43

Figure 4.3: (a) Continuum body subjected to surface traction and body force, and (b) plastic deformation of the continuum body..... 44

Figure 4.4: Yield function, stress, and strain rate for the lower-bound approach of limit analysis..... 45

Figure 4.5: Yield function, stress, and strain rate for the upper-bound approach of limit analysis..... 47

Figure 4.6: Construction of plastic potential (g-function) using yield surface and strain increments (from Palmer 1966) 50

Figure 4.7: (a) Rigid quadrangle block with tractions, velocities, and velocity jumps, (b) hodograph, and (c) polygon of forces 51

Figure 4.8: Tractions and velocity jumps for Mohr-Coulomb yield criterion with associative and non-associative flow rule 53

Figure 4.9: Prandtl-type mechanism for calculation of N_c and N_q; (a) rigid block translation, (b) hodograph, (c) continual deformation, and (d) its hodograph..... 56

Figure 4.10: Bearing capacity factors computed using different number of blocks for rigid block in a translation mechanism; (a) N_c, and (b) N_q..... 57

Figure 4.11: Hoek-Brown yield criterion (a) in Haigh-Westergaard space; (b) on $\sigma_n - \tau$ plane with tractions T and velocity discontinuity vectors v on kinematic discontinuities, conforming to the associative flow rule 58

Figure 4.12: Tractions and velocity jumps for Hoek-Brown yield criterion with non-associative flow rule..... 60

Figure 4.13: Hoek-Brown yield criterion and substitution Hoek-Brown yield criterion for non-associative rock (m_i=5, D=0, GSI=65, ϑ=0°)..... 62

Figure 5.1: Comparison of mechanisms for slope stability: (a) strain rate field from FELA (red/blue – max/min), and (b) contours of optimized collapse mechanism from classical limit analysis with superimposed velocities from FELA 65

Figure 5.2: Independence of parameter c cotϕ of the safety factor..... 66

Figure 5.3: Stability chart for uniform slopes (2D plane strain analysis) obtained from FELA and classical limit analysis method..... 68

Figure 5.4: Three-dimensional mechanism generated by the rotation of a circle with a variable diameter (after Michalowski 2010)..... 69

Figure 5.5. Boundary conditions of a slope in 3D FELA 70

Figure 5.6: Contours of velocity magnitudes from 3D FELA, uniform slopes of β=45°, B/H=2, and $c/(\gamma H)$=0.5: (a) ϕ=30° and (b) ϕ=40°..... 71

Figure 5.7: Stability chart for uniform slopes (3D analysis) obtained by FELA..... 72

Figure 5.8: (a) Coulomb-type mechanism for lateral active earth pressure, and (b) hodograph .. 75

Figure 5.9: (a) Sandwich mechanism, and (b) multi-wedge mechanism for retaining wall passive load (from Chen and Rosenfarb 1973)..... 77

Figure 5.10: (a) Multi-block mechanism for active earth pressure, (b) hodograph, and (c) example volume element used for calculating the work rate of soil weight..... 78

Figure 5.11: (a) Coulomb-type mechanism for lateral active earth pressure, and (b) hodograph 80

Figure 5.12: (a) Multi-block mechanism for passive earth pressure, (b) hodograph, and (c) example volume element used for calculating the work rate of soil weight..... 82

Figure 5.13: Coefficient K_p as a function of ϑ/ϕ 86

Figure 5.14: (a) Coefficient K_p, and (b) Non-associativity impact factor computed by the multi-block mechanism and Coulomb, as a function of ϑ/ϕ 90

Figure 5.15: (a) Half of a symmetric translational mechanism, (b) hodograph, (c) example volume element used for calculating the work dissipation rate, and (d) example volume element used for calculating the work rate of soil weight 96

Figure 5.16: Elements for computing W_q and their corresponding horizontal lengths 97

Figure 5.17: (a) Non-symmetric translational mechanism, (b) hodograph, (c) example volume element used for calculating the dissipation rate, and (d) example volume element used for calculating the work rate of soil weight 98

Figure 5.18: (a) Dual-rotational mechanism, and (b) hodograph 99

Figure 5.19: (a) Mixed mechanism, (b) hodograph, and (c) example volume element in region ADFA used for calculating the work rate of soil weight 101

Figure 5.20: Proportional loading path OC in the multi-parameter load space 103

Figure 5.21: Yield locus for a strip footing with $\phi = 35°$, $\phi_w = 2/3 \cdot \phi$, and normalized surcharge load of $q/(\gamma B) = 1$: (a) associative soil; (b) non-associative soil with dilation angle $\vartheta = 0°$ 105

Figure 5.22: Bearing capacity factors for footings subjected to a vertical load for (a) $\phi = 40°$, and (b) $\phi = 20°$ 108

Figure 5.23: Impact of non-associativity on bearing capacity factors for footings subjected to a vertical load 109

Figure 5.24: Extreme impact of non-associativity on slope stability, retaining wall loads, and bearing capacity factors obtained by comparing associative (ϑ/ϕ) and non-associative flow rule (ϑ=0°) for ϕ=30° and 40° 110

Abstract

Limit analysis is widely used in geotechnical engineering to estimate stability measures or limit loads on earth structures. The classical formulation of limit analysis relies on the assumption of associative plastic flow rule. While correctly predicting the kinematics of deformation for metals, the observed behavior of soils contradicts the computational outcomes based on the normality flow rule. Laboratory tests demonstrate that geomaterials typically exhibit limited volumetric deformation, far smaller than that predicted by the flow rule associated with pressure-dependent yield criteria. Ignoring the non-associativity of plastic flow in assessment of stability of geotechnical structures is a source of inaccurate predictions of stability measures or limit loads.

The impact of non-associative plastic flow on stability measures is quantified and explained in this dissertation for geotechnical structures, such as slopes and shallow foundations. Focusing on the kinematic approach of limit analysis, the study demonstrates that non-associativity changes the geometry of collapse mechanisms and affects the calculated energy dissipation during collapse, as well as the work of gravity forces. The non-associativity has the greatest impact on problems where large amounts of soil mass are displaced against gravity. This is because the size of the failure mechanisms depends on the non-associativity, and the large mechanisms mobilize greater soil volumes, requiring larger work to trigger structural collapse. Consequently, factor of safety for slopes is affected to a lesser extent by non-associativity than the bearing capacity of foundation footings, as for slopes, gravity contributes predominantly to the failure-causing forces, rather than resistance.

To provide a practical quantitative metric, a *non-associativity impact factor* is introduced, defined as the relative difference in stability measures, or limit loads, owed to different degrees of non-associativity. Using this metric, of the geotechnical structures considered, the greatest sensitivity was found in the bearing capacity of foundation footings on sand, where the impact factor reached 70.45% for sand with internal friction angle of 40°. The least impact was found on the factor of safety of slopes, with the extreme impact on the factor of safety reaching only 23.40% for soil with the same internal friction angle. These results indicate the potential error introduced by assuming associativity in common geotechnical stability problems.

Chapter 1 Introduction

1.1 General Background

In the pursuit of safety, stability analysis of geotechnical structures has been one of the main research topics in the field of geotechnical engineering. An accurate prediction of failure mechanisms and collapse loads is essential to ensure safety and optimized design. In order to design geotechnical structures within their safety limits, the strength of materials and how they deform have been of interest to engineers and scientists for centuries. Early formal mathematics-based research on the mechanics of materials was mainly in the context of elasticity. The scientific investigation of metal plasticity can be said to have begun in 1864. That year, Tresca presented an initial report on his experiments on punching and extrusion and drew a conclusion that metals deform plastically when the maximum shear stress in the material is at its critical value. The critical shear stress concept suggested by Tresca can be interpreted as a concept of yielding condition in modern plasticity. Although Tresca did not use modern tensor notation, his conclusion is essentially the same as what we now call Tresca yield criterion. It reads

$$\max(\sigma_1 - \sigma_2, \sigma_2 - \sigma_3, \sigma_1 - \sigma_3) = 2K \tag{1.1}$$

where σ_1, σ_2, and σ_3 are the principal stresses and K is the shear strength. Tresca yield criterion is presented in Fig. 1.1. Fig. 1.1 (a) presents the corresponding stress state ($\sigma_1 \geq \sigma_2 \geq \sigma_3$) on the $\sigma_n - \tau$ space and Fig. 1.1 (b) illustrates the Tresca yield function in 3D σ_1, σ_2, and σ_3 space, which was later named as Haigh-Westergaard space (compression-positive convention).

(a) (b)

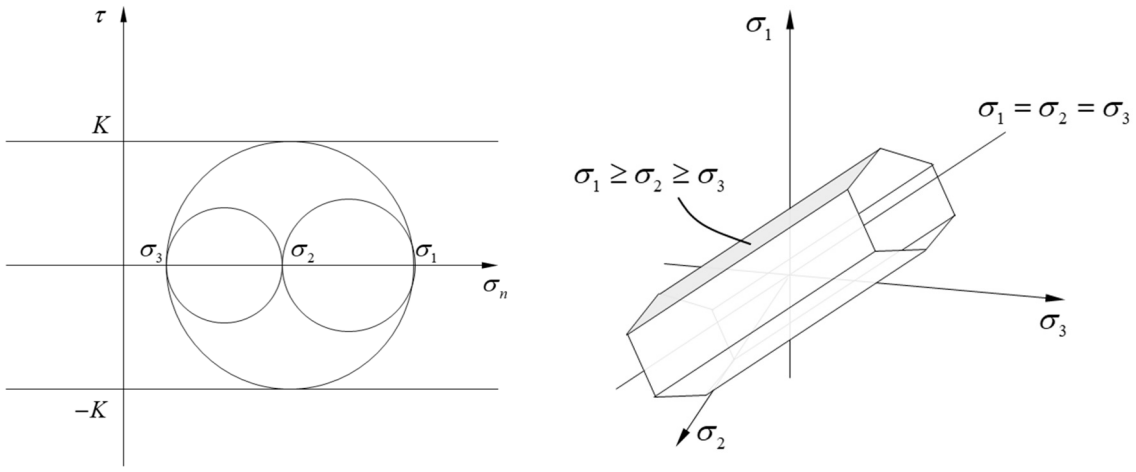


Figure 1.1: Tresca yield criterion in (a) $\sigma_n - \tau$ space, and (b) in the Haigh-Westergaard space

After Tresca's experimental investigations, Saint-Venant was the first one to formulate the fundamental equations of metal plasticity and to apply them to several problems, including bending and torsion of beams. Saint-Venant, in 1870, set up a system of five equations governing the stresses and strains in 2D space. The equations include stress equilibrium equations, incompressibility equation, Tresca yield criterion, and coaxiality equation. They read

$$\begin{cases} \dfrac{\partial \sigma_x}{\partial x} + \dfrac{\partial \tau_{yx}}{\partial y} = 0 \\ \dfrac{\partial \tau_{xy}}{\partial x} + \dfrac{\partial \sigma_y}{\partial y} = \gamma \\ \dfrac{\partial u_x}{\partial x} + \dfrac{\partial u_y}{\partial y} = 0 \\ {\tau_{xy}}^2 + \left(\dfrac{\sigma_x - \sigma_y}{2} \right)^2 = K^2 \\ \dfrac{\sigma_y - \sigma_x}{2\tau_{xy}} = \dfrac{\frac{\partial u_y}{\partial y} - \frac{\partial u_x}{\partial x}}{\frac{\partial u_y}{\partial x} + \frac{\partial u_x}{\partial y}} \end{cases} \tag{1.2}$$

where σ is the normal stress, τ is the shear stress, γ is the unit weight, u is the displacement vector, and K is the shear strength in the Tresca yield criterion. The system of five equations (Eq. 1.2) has advanced plasticity field, and these equations were used to solve plasticity problems.

At the turn of the 20th century, further advancements were made in understanding yield criteria for materials under complex stress states. Huber (1904) proposed a new yield criterion based on the concept of distortional energy. Von Mises (1913) independently proposed the same yield criterion by showing that yielding is governed by the second invariant of the deviatoric stress tensor rather than by the maximum shear stress alone, using the graphical representation of stress states introduced by Mohr (1900). The yield criterion suggested by Huber (1904) and Von Mises (1913), often referred to today as Huber-Mises yield criterion, Fig 1.2.

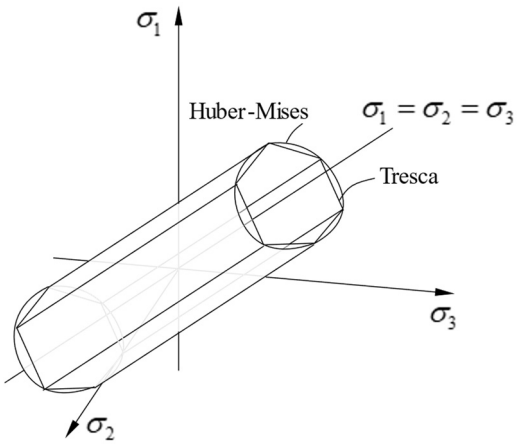


Figure 1.2: Huber-Mises yield criterion and Tresca yield criterion in the Haigh-Westergaard space (after Huber 1904 and Von Mises 1913)

The Huber-Mises yield criterion states that yielding occurs when the second invariant of the deviatoric stress tensor reaches a critical value. It reads

$$J_2 = \frac{1}{6}\left[(\sigma_1 - \sigma_2)^2 + (\sigma_2 - \sigma_3)^2 + (\sigma_3 - \sigma_1)^2\right] = k^2 \tag{1.3}$$

where J_2 is the second invariant of the deviatoric stress tensor, $\sqrt{3}\,k$ is the tensile strength. This criterion is particularly suitable for metals, and it accounts for the effect of all three principal

stresses, unlike the Tresca criterion, which is independent of the intermediate principal stress. The Huber-Mises criterion provided a more general and accurate description of yielding in isotropic, ductile materials under complex loading conditions and has been fundamental in the development of metal plasticity theory.

Prandtl applied plasticity theory to solve problems, such as punch indentation of metals (Prandtl 1920). Fig. 1.3 shows a schematic of a vertical load applied at the center of a perfectly plastic frictional material. Line ABCDE represents the boundary of the solution domain. The orthogonal networks of lines within the region ABCDEA are trajectories of major and minor principal stresses.

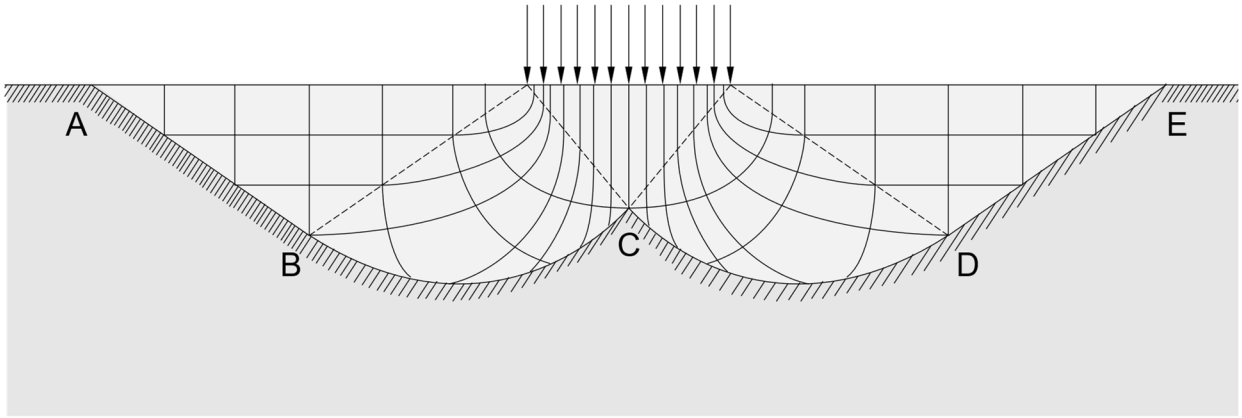


Figure 1.3: Schematic of punch indentation into a plastic material (after Prandtl 1920)

Subsequently, the theory of plasticity progressed rapidly, constituting an important branch in engineering mechanics. Sokolovskii played a pivotal role in applying plasticity in soil mechanics. Sokolovskii introduced the *method of characteristics* to soil mechanics, a powerful technique for analyzing plastic stress fields and flow in soils. In his 1943 book on the statics of granular media, he provided analytical solutions for many problems in soil mechanics, such as limit loads on foundation soils and stability of slopes.

Hill (1951) and Drucker et al. (1952) further enriched the field by presenting formal theorems of *limit analysis*, which provide the upper and lower estimates of collapse loads as well as other safety measures. Koiter (1960) indicated that limit analysis theorems are special cases of shakedown theorems, and found it peculiar that they were independently developed in the early

1950s, some twenty years after the first contributions to shakedown (Bleich 1932, Melan 1938). Gvozdev's work in 1936 with the framework of maximum and minimum structural loads, which he stated as limit conditions, may be one of the early contributions to limit analysis. Theorems of limit analysis, just like the developments in the theory of plasticity, focused on metals. The early contributions of limit analysis theorems to geotechnical engineering are attributed to Drucker and Prager (1952). Their framework made limit analysis successfully adopted in geotechnical engineering. Greenberg and Prager (1968) provided an important step forward by explicitly connecting limit analysis with mathematical programming techniques. Their work demonstrated that limit load problems could be formulated within the framework of linear programming, thereby opening a pathway for the use of optimization methods in plasticity and stability analyses. Chen (1975) presented a comprehensive collection of limit analysis solutions in soil mechanics, providing upper-bound and lower-bound estimates for stability measures of geotechnical structures. Limit analysis has been favored for its robustness, and it continues to be utilized in modern geotechnical engineering due to its effectiveness in stability analyses.

With the advancement of computational methods, Finite Element Limit Analysis (FELA) emerged as a powerful numerical tool that extended classical limit analysis to complex geotechnical problems. FELA formulates the lower and upper-bound principles of limit analysis by discretizing the soil domain into finite elements and formulating the boundary problems as large-scale optimization problems. An example of FELA result for a rigid footing subjected to an inclined eccentric load is shown in Fig. 1.4. The figure shows an optimized mesh that discretizes the soil domain and plastic shear strain field (red/blue – max/min).

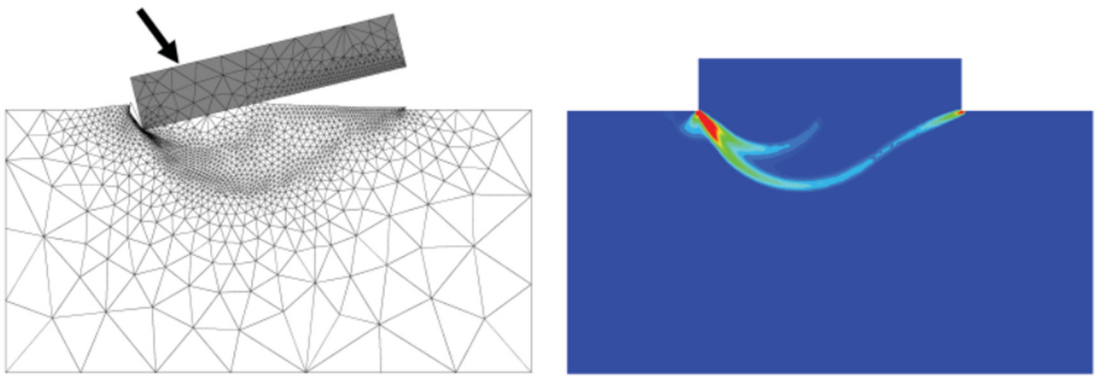


Figure 1.4: Rigid footing subjected to an inclined eccentric load (Sloan 2013)

FELA allows direct computation of collapse loads without the need for assuming a stress field or a collapse mechanism, as in classical limit analysis. The earliest finite element formulation of limit analysis is attributed to Lysmer (1970). Lysmer cast limit load problems into a finite element-linear programming framework from a general mechanics perspective. Building on this, Pastor and Turgeman (1976) and Bottero et al. (1980) applied FELA specifically to soil mechanics, demonstrating both static and kinematic formulations and showing its capability in problems such as slope stability and foundation pull-out. Other contributions to the modern form of FELA were subsequently made by Sloan (1988; 1989), later extended via nonlinear programming and second-order cone programming to improve robustness and efficiency (Lyamin and Sloan 2002a,b; Makrodimopoulos and Martin 2006). Krabbenhøft et al. (2005) further generalized this approach by utilizing the Second-Order Cone Programming (SOCP) framework in limit analysis problems. Building on this theoretical foundation, Krabbenhøft and co-workers later developed OptumG2 and OptumG3, commercial FELA software that implements SOCP-based formulations, making advanced FELA methods accessible for practical geotechnical engineering applications.

1.2 Non-associativity of plastic flow in soils

Limit analysis relies on two assumptions: the convexity of the yield condition and the associative plastic flow rule. The latter requires the plastic strain increments to be normal to the yield surface, in the conjugate spaces of stress and strain rate. The assumption of associativity has worked well for metals. However, soils exhibit non-associative behavior, characterized by plastic strain increment that is not normal to the yield surface, leading to discrepancies between theoretical predictions and observed responses. The concept of non-associativity, which deviates from the classical associative flow rule, was described by Mroz (1963). Insights into the behavior of non-associative materials have been explored by Radenkovic (1962), who provided theorems of limit analysis for non-associative materials. His first theorem states that active limit loads on non-associative material are bounded from above by the solution for associative material. The second theorem states that active limit loads on non-associative material are bounded from below by the solution for a fictitious associative material that has a yield surface defined by the plastic potential of the non-associative material. The plastic potential must be inscribed in the true yield condition.

A significant theoretical contribution was provided by Davis (1968), who examined the fundamental aspects of plasticity and soil failure mechanisms under the Mohr-Coulomb framework. Davis constructed both stress and velocity characteristics for non-associative flow, showing that the velocity characteristics do not coincide with the stress characteristics (Fig. 1.5), unless dilation angle (Ψ in Fig. 1.5) equals the internal friction angle ϕ.

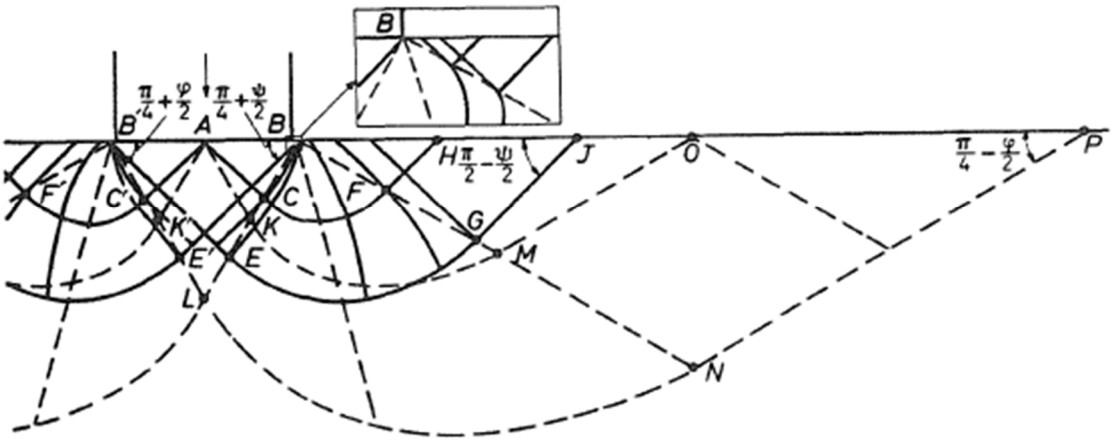


Figure 1.5: A schematic of bearing capacity problem with non-associative soil: stress characteristics (dashed lines) and velocity characteristics (solid lines) for incompressible soil (from Davis 1968)

He then provided a practical way to compute tractions on velocity characteristic using the Mohr-Coulomb parameters (c and ϕ) and dilatancy angle ϑ. Along a velocity characteristic, the traction satisfies a Mohr-Coulomb-like relation $\tau_k = c_k + \sigma_k \tan\phi_k$ with modified parameters

$$c_k = c\frac{\cos\vartheta\cos\phi}{1-\sin\vartheta\sin\phi}, \qquad \tan\phi_k = \frac{\cos\vartheta\sin\phi}{1-\sin\vartheta\sin\phi} \tag{1.4}$$

The literature offers relatively few developments for non-associative plasticity. Most contributions introduce modest modifications to the existing framework. With this context, two additional studies are discussed, one involving the classical Cam clay model with associative and non-associative flow rules, and a newer study with a modification of Davis's method. Banerjee and Stipho (1978) further extended plasticity theory to explore the role of associated and non-associated flow rules, especially for undrained behavior in soft clays. They compared the modified Cam clay yield function with associative flow rule, the original Cam clay yield function with

associative flow rule, and the original Cam clay yield function with non-associative flow rule. Modified Cam clay model yield function was used as the plastic potential, Fig. 1.6.

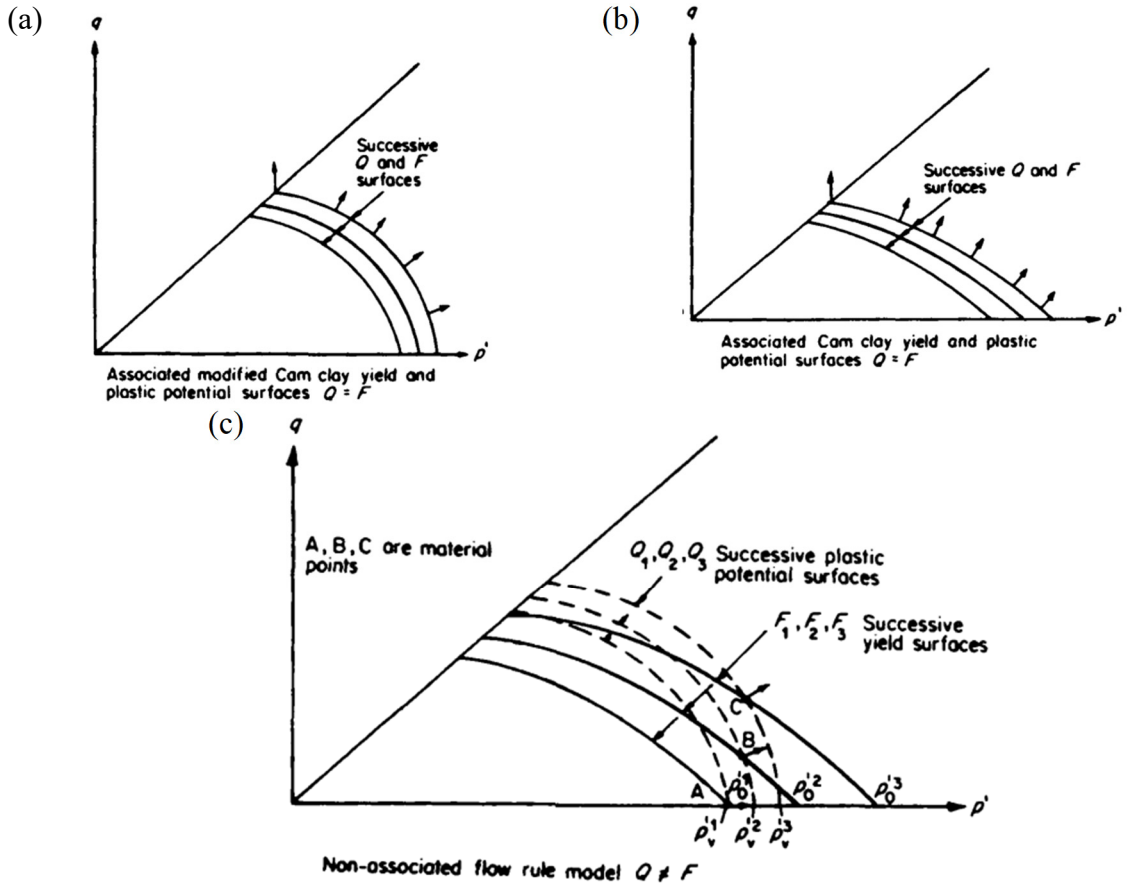


Figure 1.6: (a) Associated modified Cam clay model, (b) associated original Cam clay model, and (c) non-associated flow rule – Cam clay yield criterion and modified Cam clay model for plastic potential (Banerjee and Stipho 1978)

All models were numerically compared with laboratory results. Results demonstrated that incorporating non-associative plastic flow rule can significantly improve the prediction of soil behavior through soil constitutive models. Non-associative model showed the best agreement with experimental data, with porewater pressure build-up and undrained stress paths, Fig. 1.7.

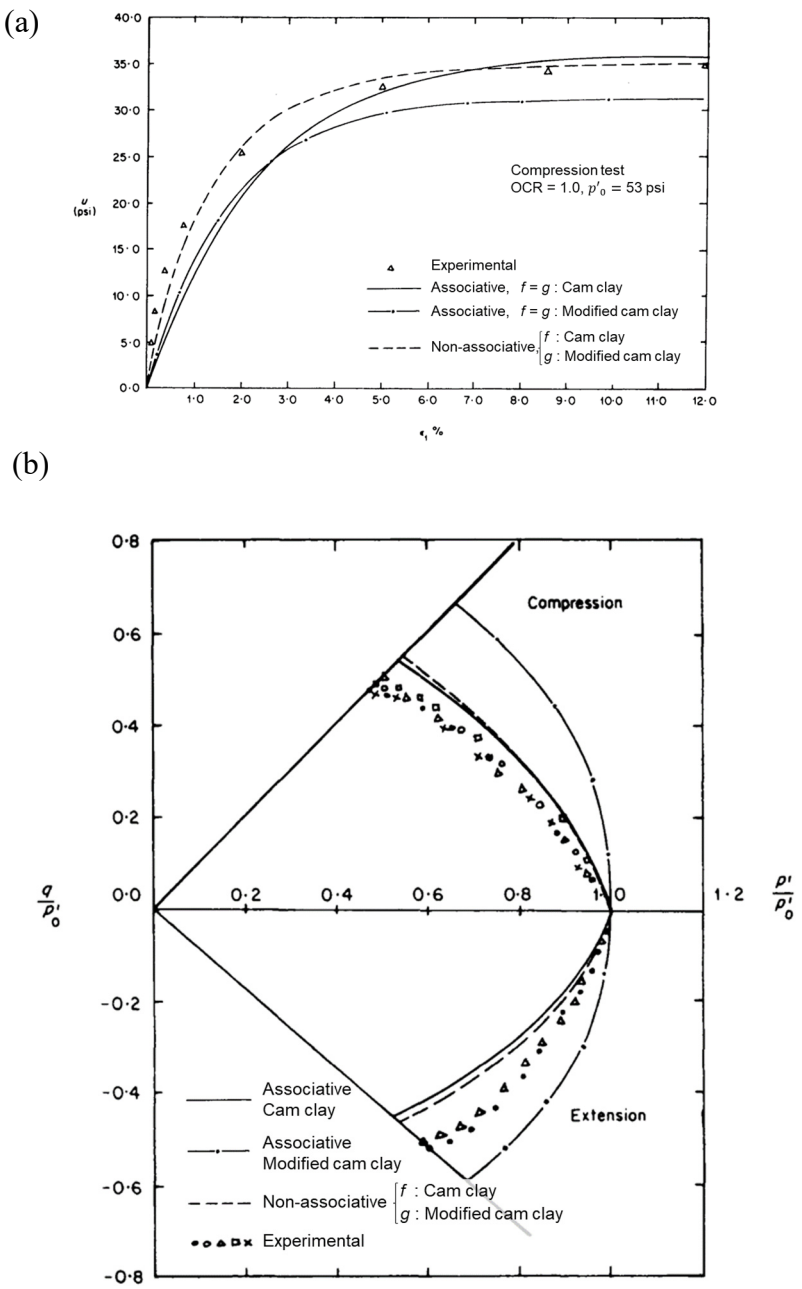


Figure 1.7: (a) Porewater pressure observation and predictions for a normally consolidated specimen and (b) Observed and predicted undrained stress paths in compression and extension tests for normally consolidated samples (Banerjee and Stipho 1978)

Chen et al. (2020) proposed a modified approach to Davis's original framework for geotechnical stability problems that involve non-associative plasticity. Prior numerical investigations by Tschuchnigg et al. (2015) and Wang et al. (2019) evaluated Davis's framework and reported that Davis's original framework may be overly conservative, especially for soils with

a large friction angle and small dilation. Hence, Chen et al. (2020) introduced a reduction parameter ω to overcome the conservatism as follows

$$\tan\phi^* = \frac{\cos[\vartheta + \omega(\phi - \vartheta)]\cos\phi}{1 - \sin[\vartheta + \omega(\phi - \vartheta)]\sin\phi}\tan\phi$$
$$c^* = \frac{\cos[\vartheta + \omega(\phi - \vartheta)]\cos\phi}{1 - \sin[\vartheta + \omega(\phi - \vartheta)]\sin\phi}c \tag{1.5}$$

where ω is a reduction parameter ($0 \leq \omega \leq 1$). They performed slope stability analysis using finite-element limit analysis (FELA) with the original Davis method and the modified Davis method (Eq. 1.5). Results from FELA were compared with results from the strength reduction finite-element method (SSRFEM). Results of slope stability analysis were presented in the form of Factor of Safety (FOS), Fig. 1.8. Results from FELA with the original Davis method are conservative compared to the SSRFEM method. Modified Davis method with a reduction parameter of $\omega = 0.3$ showed the least error compared to the SSRFEM method. Their modifications of the Davis method, especially for $\omega = 0.3$, could offer improved estimates of ultimate loads for slopes and foundations. However, this modification (Eq. 1.5) is a provisional adjustment, because it replaces a relation with clear mechanical meaning with a fitted form. While the fitted reduction parameter may improve agreement with SSRFEM in specific cases, its physical meaning and transferability are uncertain and should be treated with skepticism.

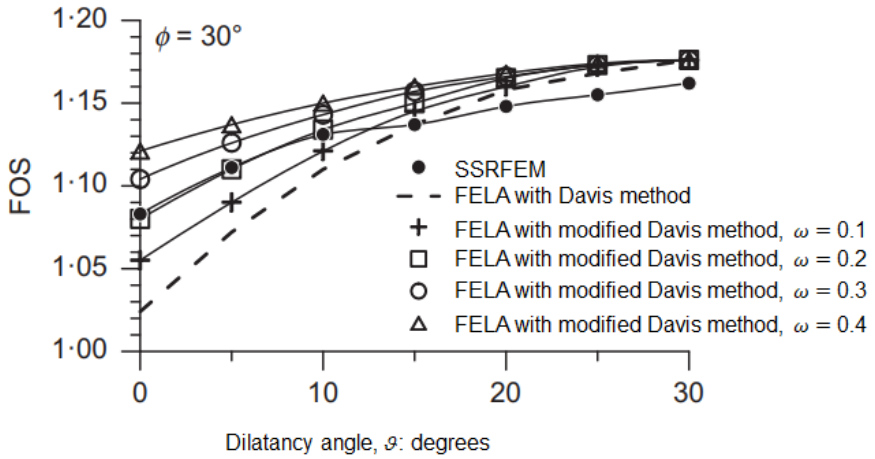


Figure 1.8: Factor of safety versus ϑ chart developed by SSRFEM and FELA (Chen et al. 2020)

A different perspective on addressing non-associativity was introduced by Chaaba et al. (2010). Their work is grounded in the concept of bipotential theory, originally developed by Saxcé and co-workers. In particular, Saxcé and Bousshine (1998) proposed the framework that generalizes the classical convex yield function analysis setting to non-associated flow rules in soils by introducing bipotential as a unified function of stress and strain rate. In other words, bipotential is a unified energy-based potential that combines the concepts of yield condition and the plastic flow rule. This approach eliminated the need to separate yield function and plastic potential functions, a distinction that had prevented classical limit analysis from being directly extended to non-associative materials. By minimizing the total plastic dissipation expressed through the bipotential, it enables kinematic limit analysis of non-associative materials. Because the bipotential coupling between the kinematic and static variables, the problem cannot be reduced to kinematic (velocity) fields alone. To address this, the authors proposed an iterative two-step approximation algorithm: (i) fixing the stress field to compute an admissible velocity field via the kinematic theorem, and (ii) updating the stress field from the constitutive relations while holding the velocity field unaltered. This process is repeated until convergence. Convergence is achieved when both the velocity and stress fields simultaneously satisfy the kinematic admissibility and the constitutive relations implied by the bipotential. In practice, this means iterating the two steps until the increment of plastic dissipation becomes negligible.

One of the notable applications of this bipotential theory is the punch indentation problem (Fig. 1.9). The soil material is modeled using a non-associative Drucker-Prager model defined by cohesion and friction angle, together with dilatancy angle.

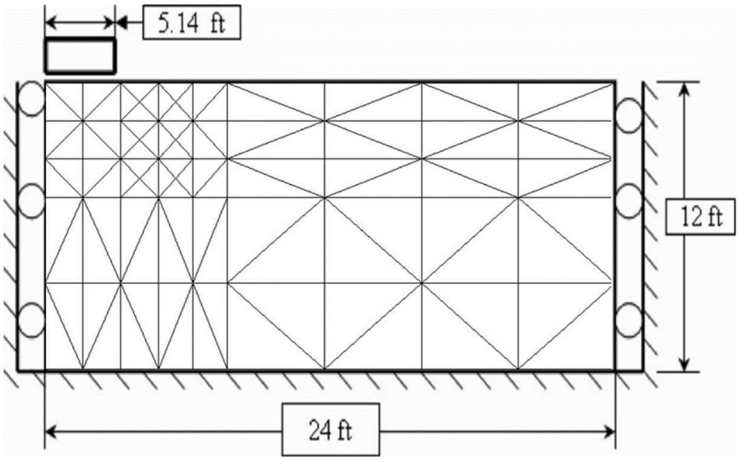


Figure 1.9: Geometry and boundary conditions with 99 triangular finite element mesh (after Chaaba et al. 2010)

The numerical results demonstrate that the bearing capacity factor N_c decreases as the dilatancy angle decreases, confirming that non-associativity systematically reduces load-carrying capacity relative to the associated case (Fig. 1.10). While these findings underscore the practical significance of accounting for non-associative flow rules in boundary value problems, it should also be noted that the bipotential framework remains challenging to implement. The reliance on iterative coupling and convergence issues at low dilatancy angles highlights that the method is still best suited for idealized benchmark problems.

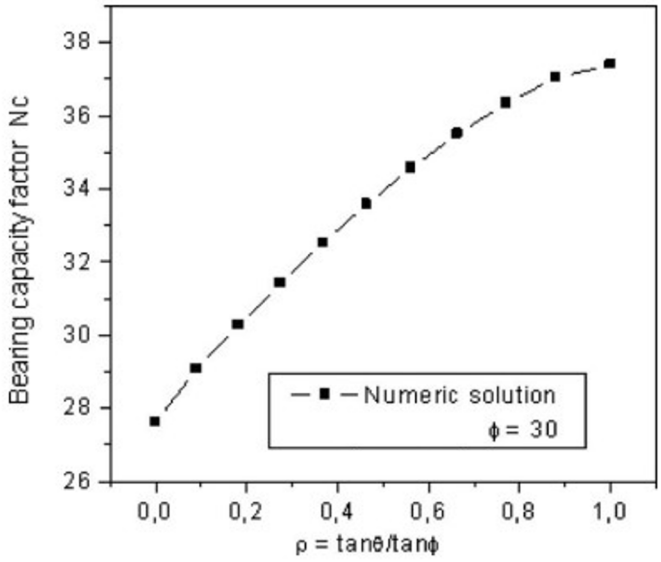


Figure 1.10: Variation of the bearing capacity factor N_c with dilatancy angle (Chaaba et al. 2010)

Chapter 2 Objectives

This research aims to address the impact of non-associative plastic flow rule of soils on the stability of earth structures, such as slopes, and the limit loads on retaining walls and foundation footings. By incorporating non-associativity, which reflects the actual soil behavior, one can achieve more accurate and realistic assessments of limit loads on geotechnical structures under various loading regimes, and ultimately enhance the design and safety of geotechnical structures. The following are the objectives of this thesis:

1. Construction and justification of substitution material approach to incorporate non-associativity of plastic flow in the kinematic (upper-bound) approach of limit analysis.

2. Quantitative assessment of the impact of non-associative plastic flow on the stability of geotechnical structures.

3. Improvement of mechanisms to obtain more accurate solutions for the stability of geotechnical structures.

Chapter 3 Plasticity of Geomaterials

Plasticity models provide a systematic framework to describe the behavior of soils and rocks subjected to loading, which is essential for assessing the stability of geotechnical structures. They capture fundamental features such as hardening during consolidation, softening under dilative deformation. By linking observed stress-strain behavior with yield criteria and flow rules, plasticity theory establishes the foundation of the description for the plastic state and behavior in soils and rocks.

3.1 Stress-strain behavior of soils and rocks

The stress-strain response of soils and rocks is dependent on factors such as relative density, confining pressure, and drainage conditions. At very small strains, soils may respond in a nearly elastic manner, but once yielding occurs, irreversible deformations develop. Dense sands under low confining pressures typically exhibit dilative behavior, showing a volume increase during shear, whereas loose sands or soils under high confining pressures tend to be contractive, undergoing volume reduction.

Fig. 3.1 presents the results of drained triaxial compression tests on Sacramento River sand (Lee and Seed 1967) prepared at a very dense state (Relative density of 100%). Deviatoric stress and the volumetric strain versus axial strain are shown for different confining pressures. Deviatoric stress q is defined here as a difference between the maximum and minimum principal stresses ($q = \sigma_1 - \sigma_3$). At low confining stresses, the sand exhibits pronounced dilative behavior. The specimen contracts slightly at the onset of shearing, followed by a rapid volume increase as shear progresses. In contrast, at high confining stresses, sand displays predominantly contractive behavior, volumetric strains remaining positive throughout the test (compression-positive convention).

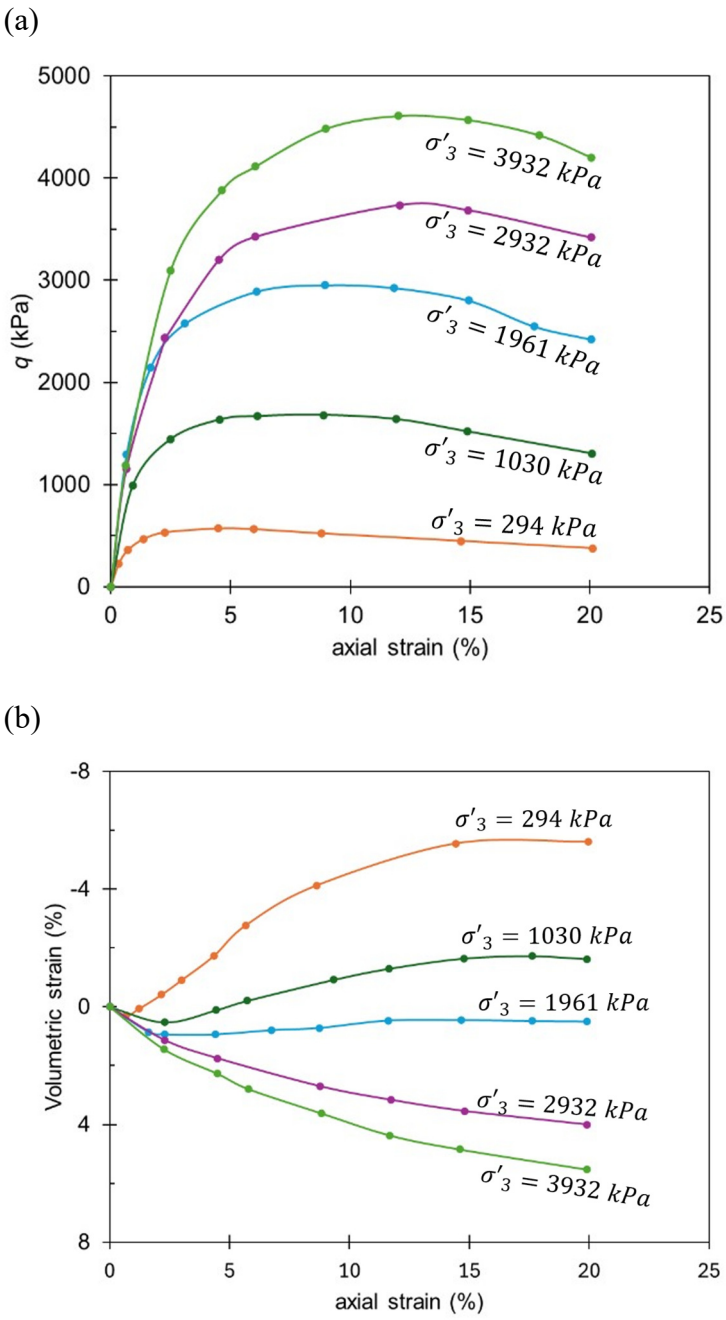


Figure 3.1: Stress-strain-volume change data for Sacramento River sand (after Lee and Seed 1967)

Experimental results provided by Lee and Seed (1967) were used to evaluate the internal friction angle and dilation angle. The peak internal friction angle was obtained by identifying the peak deviatoric stress on the q-axial strain curve. The corresponding dilation angle ϑ was obtained by using the strain-increment definition of dilatancy (Wood 1990)

$$\tan \vartheta = \frac{d\varepsilon_v}{d\varepsilon_q} \tag{3.1}$$

where $d\varepsilon_v$ is the volumetric strain increment and $d\varepsilon_q$ is the deviatoric strain increment. $d\varepsilon_v$ and $d\varepsilon_q$ are expressed in terms of the principal strain increments as

$$d\varepsilon_v = d\varepsilon_1 + 2d\varepsilon_3, \quad d\varepsilon_q = \frac{2}{3}\left(d\varepsilon_1 - d\varepsilon_3\right) \tag{3.2}$$

Combining Eqs. (3.1) and (3.2) yields

$$\tan \vartheta = \frac{3\frac{d\varepsilon_v}{d\varepsilon_a}}{3 - \frac{d\varepsilon_v}{d\varepsilon_a}} \tag{3.3}$$

where $d\varepsilon_a (= d\varepsilon_1)$ is the increment of axial strain. Comparison of the internal friction angle and dilation angle offers insight into the validity of the associative flow rule.

The results show that at low confining stress, the dilation angle is of similar magnitude to the peak friction angle, though slightly smaller. But at high confining stresses, the dilation angle is significantly smaller than the peak friction angle. These dilation angles are not taken directly from Lee and Seed (1967), but were computed here using their published triaxial test data. The results are shown in Table 3.1.

Table 3.1: Internal friction angle and dilation angle for Sacramento River sand specimens subjected to different confinements (all values were calculated from the raw test data of Lee and Seed 1967)

σ_3' (kPa)	ϕ (°)	ϑ (°)
294	36.5	27.0
1030	34.6	10.5
1961	33.8	4.9

This divergence between the friction angle and dilation angle demonstrates that the associative flow rule does not accurately capture the experimental behavior across the full range of confining stresses. Instead, soils display systematically lower dilatancy than would be predicted by associative flow rule, particularly under high confinement. This inconsistency provides clear evidence for the need to adopt non-associative flow rule in order to realistically represent soil behavior in plasticity models.

Another line of evidence supporting the need for non-associative flow rule is provided by the drained triaxial test data reported by Lade (2016). Fig. 3.2 shows the triaxial test data. The experimental results of dense samples of Antelope Valley sand showed a similar trend as Lee and Seed (1967). At low confinement, dilation dominates and peak strength is clearly mobilized, whereas at high confinement, contractive volumetric strains prevail and the stress-strain curve displays hardening without softening.

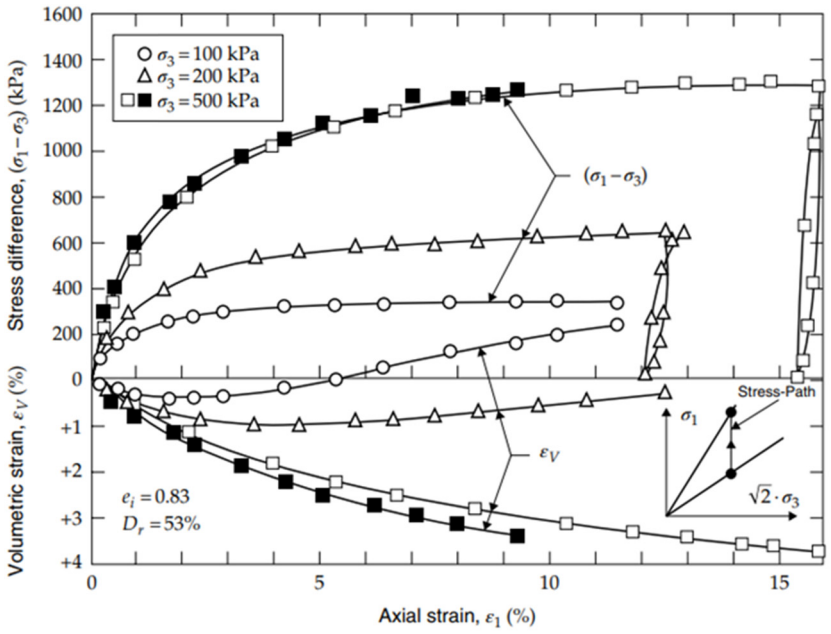


Figure 3.2: Results of drained triaxial compression tests on dense Antelope Valley sand (Lade 2016)

By using the data from Lade (2016), the peak internal friction angle can be back-calculated from the maximum deviatoric stress, while the dilation angle is obtained using Eq. (3.3). Computed results of the peak friction angle and dilation angle are presented in Table 3.2.

Table 3.2: Internal friction angle and dilation angle for Antelope Valley sand specimens subjected to different confinements (all values were calculated from the raw test data of Lade 2016)

σ_3' (kPa)	ϕ (°)	ϑ (°)
100	39.0	11.4
200	38.0	6.0

While the preceding discussion has focused on soils, similar patterns are also observed in rocks. Rocks exhibit a wide range of stress-strain behaviors, from brittle fracture at low confinement to ductile flow at high confinement. At low confining stresses, rocks typically fail suddenly after limited strain, producing sharp stress drops in testing. This is a characteristic of brittle behavior. With increasing confinement, the failure mode transitions to ductile deformation, allowing the material to sustain larger strains before failure. This poses a challenge for plasticity-based methods, which assume perfect plasticity and ductility of deformation in the entire stress range. However, Chen (1975) argued that if the deformation before the brittle stress drop is sufficiently large, the material may be treated as perfectly plastic for the purpose of applying limit analysis theorems. This reasoning supports the use of limit analysis in rock mechanics, but its applicability is constrained by the degree of structural integrity of the rock mass. In practice, this approach is considered valid mainly for rock masses with the Geological Strength Index (*GSI*) of 75 or less, where the presence of joints, faults, and cracks provides natural discontinuities in all directions. Along these joints, velocity discontinuities can be meaningfully defined, making the kinematic method of limit analysis a reasonable approximation.

These general considerations are further substantiated by experimental data. Arzúa and Alejano (2013) conducted a comprehensive series of tests on different granitic rock samples, among which the Amarelo País offers the most complete information. Amarelo País is a slightly weathered granite, for which the *GSI* of approximately 65-75 can be inferred, indicating a moderately jointed rock mass where discontinuities play a governing role in failure processes.

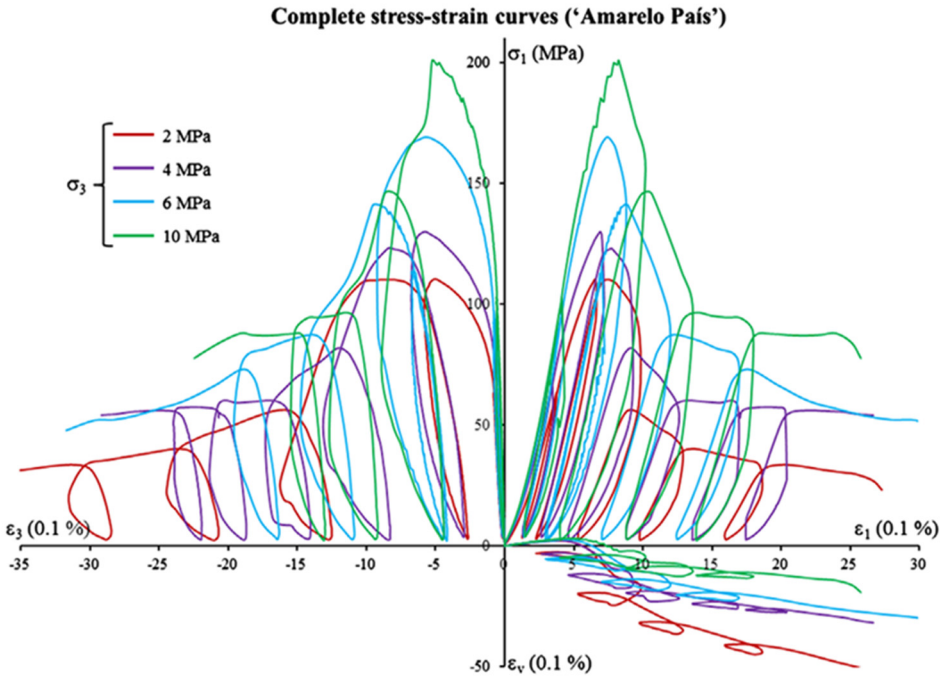


Figure 3.3: Complete stress-strain curves for Amarelo País granite (from Arzúa and Alejano 2013)

Fig. 3.3 shows the complete stress-strain curves obtained at confining pressures between 2 and 10 MPa. Based on this data, the parameters of the Hoek-Brown yield criterion were calculated to represent the failure envelope of this rock mass. Fig. 3.4 shows the Hoek-Brown yield criterion calculated from the triaxial test data and plastic stress states (Mohr circles). Assuming an associative flow rule, the rupture angle δ is equal to the mobilized friction angle. The observed (actual) rupture angles were measured from the data, using Eq. (3.3). Direct comparison between the predicted rupture angles and the experimentally observed rupture angle is summarized in Table. 3.3.

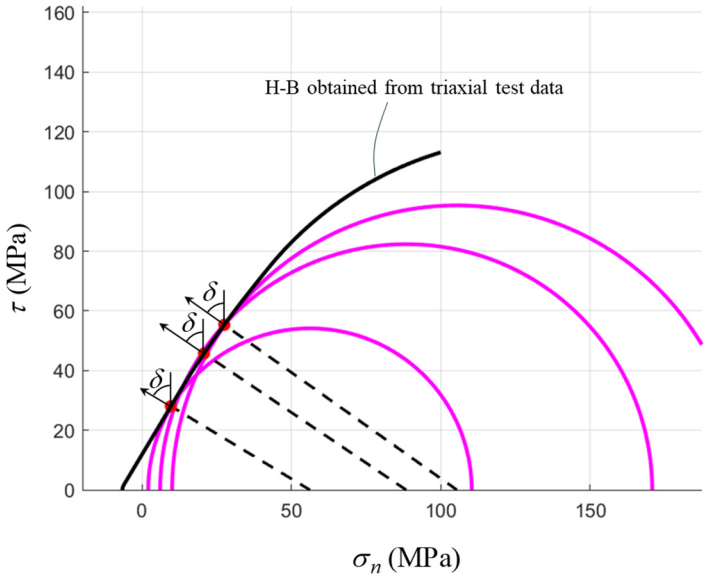


Figure 3.4: Hoek-Brown yield criterion from Arzúa and Alejano (2013) (black solid curve), superimposed with stress states extracted from the raw test data of Arzúa and Alejano (2013)

Table 3.3: Predicted and observed rupture angle for Amarelo País granite specimens at different stress states (all values were calculated from the raw test data of Arzúa and Alejano 2013)

σ_3' (MPa)	σ_1' (MPa)	Predicted δ (°) (Associative flow rule)	Observed δ (°) (Triaxial test)
2	110	58.9	49.1
6	171	56.0	43.9
10	201	54.6	43.3

The associative flow rule implies that dilatancy angles are identical to a strength parameter. However, both soil and rock test data consistently show that the observed dilation or rupture angles are smaller than those predicted. This indicates that associativity systematically overestimates dilatancy, leading to unrealistic kinematics of deformation. Consequently, non-associative flow rules are required to more accurately reproduce experimental behavior and ensure reliable predictions of stability in geomaterials.

3.2 Yield criteria and flow rules

Yielding in materials is defined by the yield criterion represented by the function $f(\sigma_{ij}) = 0$ in the stress space. Fig. 3.5 shows a stress space and a conjugate strain rate space.

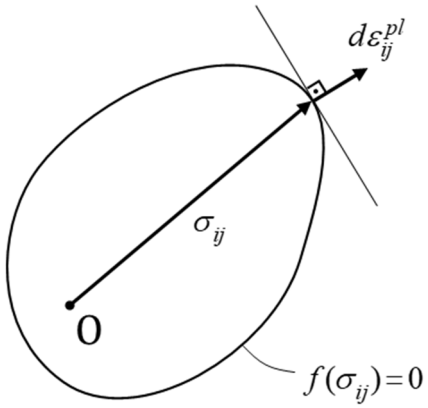


Figure 3.5: Yield function and plastic strain rate

$d\varepsilon_{ij}^{pl}$ is the plastic strain rate increment. When the stress state σ_{ij} satisfies $f(\sigma_{ij}) = 0$, irreversible deformation (plastic strain increment $d\varepsilon_{ij}^{pl}$) becomes possible. Once the plastic strain is initiated, its evolution is governed by a flow rule. The flow rule specifies how plastic strains develop at yielding, but it does not quantify the strain rate increments. In many classical plasticity models, it is assumed that the plastic flow is associative, and the direction of plastic strain increment is normal to the yield surface in stress space. Under this associativity assumption, the plastic strain increment is given by

$$d\varepsilon_{ij}^{pl} = d\lambda \frac{\partial f}{\partial \sigma_{ij}} \qquad \begin{cases} d\lambda = 0 \text{ if } f < 0 \\ d\lambda \geq 0 \text{ if } f = 0 \end{cases} \tag{3.4}$$

where $d\lambda$ is the plastic multiplier (not a material property in perfect plasticity). Once the yield function and plastic flow rule are defined, the plastic response of a material can be fully described in terms of its stress and strain rate evolution within the plastic process.

A complete description of the plastic state requires considering two complementary perspectives: the statics, which enforces equilibrium and yield consistency of the stress field, and the kinematics, which characterizes compatible strain-rate or velocity fields driven by the plastic flow rule. Together, these perspectives form the basis for understanding how geomaterials behave in the plastic state.

3.2.1 Statics of the limit state

Once the stress state in a soil reaches its yield condition, plastic deformation becomes possible. The plastic stress field in any boundary value problem must satisfy both the equilibrium equations and the yield criterion. It also must conform to the boundary conditions. The yield criterion that is used in engineering the most to describe the plastic state of soils is the Mohr-Coulomb function. The Mohr-Coulomb criterion is used here together with the differential equations of equilibrium to show the development of a method for finding plastic stress fields when the set of stress boundary conditions is sufficient. The procedure is based on the mathematical method of characteristics for solving hyperbolic-type differential equations. The Mohr-Coulomb yield criterion is shown in Fig. 3.6 and it is expressed here as

$$f(\sigma)=\sqrt{(\sigma_x-\sigma_y)^2+4\tau_{xy}{}^2}-(\sigma_x+\sigma_y)\sin\phi-2c\cos\phi=0 \tag{3.5}$$

where ϕ is the internal friction angle of soil and c is the cohesion.

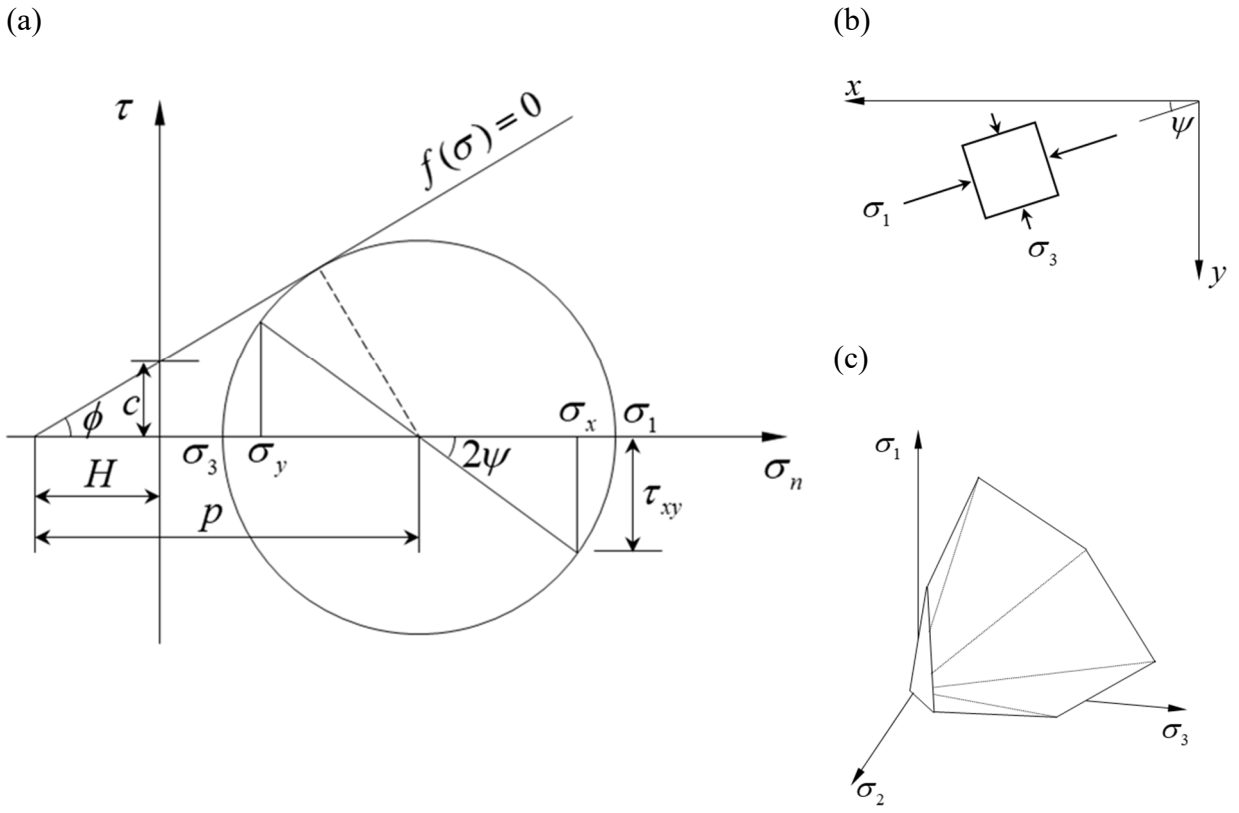


Figure 3.6: (a) Mohr-Coulomb failure criterion, (b) orientation of major principal stress in the physical space, and (c) Mohr-Coulomb failure criterion in the Haigh-Westergaard space

The stress state must satisfy stress equilibrium, and, assuming that the gravity direction coincides with axis *y*, we have the following set of stress equilibrium equations for plane strain conditions

$$\begin{aligned} \frac{\partial \sigma_x}{\partial x} + \frac{\partial \tau_{yx}}{\partial y} &= 0 \\ \frac{\partial \tau_{xy}}{\partial x} + \frac{\partial \sigma_y}{\partial y} &= \gamma \end{aligned} \tag{3.6}$$

In order to solve the set of equations (3.5) and (3.6), the former is presented in a parametric form with two parameters p and ψ

$$\begin{aligned}\sigma_x &= p(1+\sin\phi\cos 2\psi) - H \\ \sigma_y &= p(1-\sin\phi\cos 2\psi) - H \\ \tau_{xy} &= p\sin\phi\sin 2\psi\end{aligned} \tag{3.7}$$

where ψ is the angle of inclination of the major principal stress to axis x, $H=c\cot\phi$, and $p = H + (\sigma_x+\sigma_y) / 2$. Substituting Eq. (3.7) into Eq. (3.6) one obtains

$$\begin{aligned}&(1+\sin\phi\cos 2\psi)\frac{\partial p}{\partial x} + \sin\phi\sin 2\psi\frac{\partial p}{\partial y} - 2p\sin\phi\sin 2\psi\frac{\partial \psi}{\partial x} + 2p\sin\phi\cos 2\psi\frac{\partial \psi}{\partial y} = 0 \\ &\sin\phi\sin 2\psi\frac{\partial p}{\partial x} + (1-\sin\phi\cos 2\psi)\frac{\partial p}{\partial y} + 2p\sin\phi\cos 2\psi\frac{\partial \psi}{\partial x} + 2p\sin\phi\sin 2\psi\frac{\partial \psi}{\partial y} = \gamma\end{aligned} \tag{3.8}$$

The set in Eq. (3.8) has four unknown derivatives $\left(\frac{\partial p}{\partial x}, \frac{\partial p}{\partial y}, \frac{\partial \psi}{\partial x}, \text{ and } \frac{\partial \psi}{\partial y}\right)$. To make the set of equations determinate, expressions for the total differentials of p and ψ are added. The total differentials of p and ψ are

$$\begin{aligned}\frac{\partial p}{\partial x}dx + \frac{\partial p}{\partial y}dy &= dp \\ \frac{\partial \psi}{\partial x}dx + \frac{\partial \psi}{\partial y}dy &= d\psi\end{aligned} \tag{3.9}$$

The characteristic equation set Eqs. (3.8) and (3.9) has two real solutions to the lines along which the discontinuities in those derivatives are admissible. Hence, the system is of hyperbolic type. Its solution yields the following equations describing two families of stress characteristic s_1 and s_2, and the stress relations along the characteristics

$$\begin{aligned}\frac{dy}{dx} &= \tan\left[\psi + \left(\tfrac{\pi}{4} - \tfrac{\phi}{2}\right)\right]; && s_1 \\ \frac{dy}{dx} &= \tan\left[\psi - \left(\tfrac{\pi}{4} - \tfrac{\phi}{2}\right)\right]; && s_2\end{aligned} \tag{3.10}$$

$$
\begin{aligned}
dp + 2p\tan\phi d\psi &= \gamma(dy + \tan\phi dx); \quad \text{along } s_1 \\
dp - 2p\tan\phi d\psi &= \gamma(dy - \tan\phi dx); \quad \text{along } s_2
\end{aligned}
\tag{3.11}
$$

Plastic stress fields can be obtained by solving these equations for given boundary conditions. In rare cases (e.g., when $\gamma = 0$), these equations can be integrated directly, or a finite difference method can be used. This stress field solution is independent of kinematics, as the original equations, Eqs. (3.5) and (3.6), include only static quantities. As a consequence, the stress solution is decoupled from the kinematics and therefore independent of whether the flow rule is associative or not. The framework for solving stress fields in soils using the *method of characteristics* is due to Sokolovskii (1943).

3.2.2 Kinematics of the limit state

While elasticity is characterized by the proportional relationship between stresses and reversible strains, plasticity involves irreversible deformation, which is defined by the relationship between plastic strain rates and the stress state. This relation is referred to as the *flow rule*. When the stress state satisfies the yield criterion, plastic flow can occur. While the statics is governed by the yield function and stress equilibrium, kinematics is governed by a flow rule. Non-associative flow rule is in a similar form to the associative flow rule (Eq. 3.4), but function *f* replaced by *g* function, plastic potential. The rate form of plastic strain is $\dot{\varepsilon}_{ij}^{pl}$ and an incremental form of it is $d\varepsilon_{ij}^{pl}$, both notations are mathematically consistent. Non-associative flow rule can be written in the following form

$$
\dot{\varepsilon}_{ij}^{pl} = \dot{\lambda}\frac{\partial g}{\partial \sigma_{ij}} \qquad \begin{cases} \dot{\lambda} = 0 \text{ if } f < 0 \\ \dot{\lambda} \geq 0 \text{ if } f = 0 \end{cases}
\tag{3.12}
$$

where $\dot{\varepsilon}_{ij}^{pl}$ is the plastic strain rate tensor, $\dot{\lambda}$ is a plastic multiplier, and $g(\sigma_{ij})$ is a plastic potential function. The plastic potential function is a function used to determine the direction of plastic

deformation in a material. Fig. 3.7 shows the superimposed stress space σ_{ij} and the strain rate space $\dot{\varepsilon}_{ij}^{pl}$. They are conjugate spaces; i.e., the product of respective components gives the rate of work. When $f(\sigma_{ij})=0$, plastic strains can occur, and orientation of the plastic strain rate $\dot{\varepsilon}_{ij}^{pl}$ is normal to the plastic potential function, $g(\sigma_{ij})=0$. For associative material, the plastic potential function is identical to the yield function, $g(\sigma_{ij})=f(\sigma_{ij})$. If the material is non-associative, then $g(\sigma_{ij})\neq f(\sigma_{ij})$.

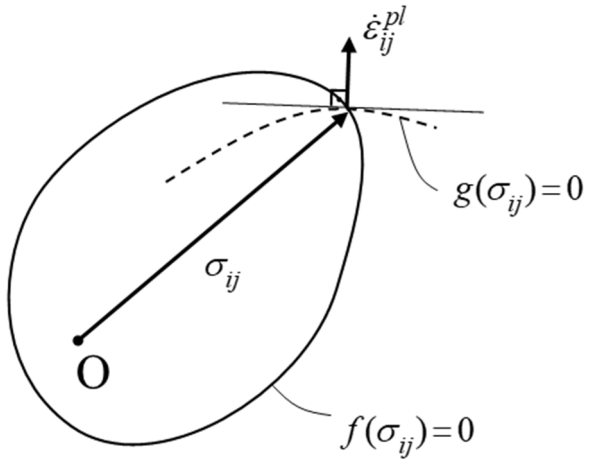


Figure 3.7: Yield function and plastic strain rate for non-associative flow rule

For soils, plastic potential is a function of the dilatancy angle ϑ, which is a measure of volumetric strain

$$g(\sigma)=\sqrt{(\sigma_x-\sigma_y)^2+4\tau_{xy}{}^2}-(\sigma_x+\sigma_y)\sin\vartheta-C=0 \tag{3.13}$$

where C is a constant that needs to be adjusted so that the plastic potential intersects the yield function at the current stress point. Substituting Eq. (3.13) into (3.12) one obtains the following expressions for the strain rate components

$$\dot{\varepsilon}_x = -\frac{\dot{\lambda}}{2}\left(\sin\vartheta - \frac{\sigma_x - \sigma_y}{\sqrt{\left(\sigma_x - \sigma_y\right)^2 + 4\tau_{xy}^2}} \right)$$
$$\dot{\varepsilon}_y = -\frac{\dot{\lambda}}{2}\left(\sin\vartheta + \frac{\sigma_x - \sigma_y}{\sqrt{\left(\sigma_x - \sigma_y\right)^2 + 4\tau_{xy}^2}} \right) \tag{3.14}$$
$$\dot{\varepsilon}_{xy} = \dot{\lambda}\frac{\tau_{xy}}{\sqrt{\left(\sigma_x - \sigma_y\right)^2 + 4\tau_{xy}^2}}$$

By standard analysis of stress state, the angle of inclination of the major principal stress to the *x*-axis can be expressed in terms of stress components

$$\tan 2\psi = \frac{2\tau_{xy}}{\sigma_x - \sigma_y} \tag{3.15}$$

Angle η of inclination of the major principal strain rate to the axis *x* can be obtained by the standard analysis of the strain rate state.

$$\tan 2\eta = \frac{2\dot{\varepsilon}_{xy}}{\dot{\varepsilon}_x - \dot{\varepsilon}_y} \tag{3.16}$$

By substituting Eq. (3.14) into Eq. (3.16), one reads

$$\tan 2\eta = \frac{2\dot{\varepsilon}_{xy}}{\dot{\varepsilon}_x - \dot{\varepsilon}_y} = \frac{2\tau_{xy}}{\sigma_x - \sigma_y} = \tan 2\psi \tag{3.17}$$

Stress state and strain rate state have the same principal directions, $\eta = \psi$. This means that the material is *coaxial*, and the trajectories of principal stresses and strain rates follow the same

directions. Since the material is *coaxial*, the strain rate components along axes x and y can be simplified by substituting Eq. (3.7) into Eq. (3.14)

$$\begin{aligned}\dot{\varepsilon}_x &= -\frac{\dot{\lambda}}{2}\left(\sin\vartheta - \cos 2\psi\right)\\ \dot{\varepsilon}_y &= -\frac{\dot{\lambda}}{2}\left(\sin\vartheta + \cos 2\psi\right)\\ \dot{\varepsilon}_{xy} &= \frac{\dot{\lambda}}{2}\sin 2\psi\end{aligned} \tag{3.18}$$

From the definition of strain rate, strain rates are defined as functions of velocities as

$$\frac{-\frac{\partial v_x}{\partial x}}{\dot{\varepsilon}_x} = \frac{-\frac{\partial v_y}{\partial y}}{\dot{\varepsilon}_y} = \frac{-\frac{1}{2}\left(\frac{\partial v_x}{\partial y} + \frac{\partial v_y}{\partial x}\right)}{\dot{\varepsilon}_{xy}} = 1 \tag{3.19}$$

By combining Eqs. (3.18) and (3.19), velocity relations are presented as linear differential equations

$$\begin{aligned}&\frac{\partial v_x}{\partial x}(\sin\vartheta + \cos 2\psi) - \frac{\partial v_y}{\partial y}(\sin\vartheta - \cos 2\psi) = 0\\ &2\sin 2\psi\,\frac{\partial v_x}{\partial x} + (\sin\vartheta - \cos 2\psi)\left(\frac{\partial v_x}{\partial y} + \frac{\partial v_y}{\partial x}\right) = 0\end{aligned} \tag{3.20}$$

Eq. (3.20) has four unknown derivatives $\left(\frac{\partial v_x}{\partial x}, \frac{\partial v_x}{\partial y}, \frac{\partial v_y}{\partial x}, \text{and}\, \frac{\partial v_y}{\partial y}\right)$ and two relations, so the system is underdetermined. To complete the system, two additional equations are introduced from the total differentials of v_x and v_y. The total differentials of v_x and v_y are

$$\frac{\partial v_x}{\partial x}dx + \frac{\partial v_x}{\partial y}dy = dv_x$$
$$\frac{\partial v_y}{\partial x}dx + \frac{\partial v_y}{\partial y}dy = dv_y \tag{3.21}$$

The set of Eqs. (3.20) and (3.21) is of hyperbolic type, and it can be solved using the method of characteristics. Equations of velocity characteristics and the velocity relations along the characteristics are

$$\frac{dy}{dx} = \tan\left[\psi + \left(\tfrac{\pi}{4} - \tfrac{\vartheta}{2}\right)\right]; \qquad k_1$$
$$\frac{dy}{dx} = \tan\left[\psi - \left(\tfrac{\pi}{4} - \tfrac{\vartheta}{2}\right)\right]; \qquad k_2 \tag{3.22}$$

$$dv_x + dv_y \tan\left[\psi + \left(\tfrac{\pi}{4} - \tfrac{\vartheta}{2}\right)\right] = 0; \quad \text{along } k_1$$
$$dv_x + dv_y \tan\left[\psi - \left(\tfrac{\pi}{4} - \tfrac{\vartheta}{2}\right)\right] = 0; \quad \text{along } k_2 \tag{3.23}$$

Eqs. (3.22) define two families of characteristics, referred to also as *slip-lines*, which are potential loci of slip. Eqs. (3.23) represent velocity relations along the two families of characteristics k_1 and k_2. Velocity characteristics (Eq. 3.22) have the same form as stress characteristics (Eq. 3.10) but with ϕ replaced by the dilatancy angle ϑ. It also indicates that velocity characteristics and stress characteristics coincide for associative materials ($\vartheta = \phi$).

3.3 Plasticity models

Plasticity models provide a framework to quantify the behavior of geomaterials under stress. They are essential for evaluating the stability of earth structures and failure mechanisms in geotechnical engineering. Among the various approaches, elastic-plastic models with hardening/softening have proven effective in describing the behavior of soils. For instance, during the consolidation process, clay compacts and strengthens, a process known as hardening. On the other hand, when a

geotechnical structure is subjected to dilative volumetric deformation, the soil may weaken and approach failure, exhibiting what is referred to as softening.

Consider the deformation of an elastic-perfectly plastic element. A stress-strain relationship of elastic-perfectly plastic behavior is shown in Fig. 3.8. Stress-strain behavior is purely elastic along segment OA, the material starts to yield at point A, where the yield stress σ_y is first reached. Strains increase at the state of yielding, segment AB, without increasing stress. After the unloading process along BC, the plastic strain ε^{pl} remains (irreversible deformation). Hence, throughout the loading path, the area OABC is the dissipated plastic work, and the area BCD is the recovered elastic work. The yield condition is not defined by a single stress value (i.e., yield stress σ_y in Fig. 3.8) but rather by a yield function.

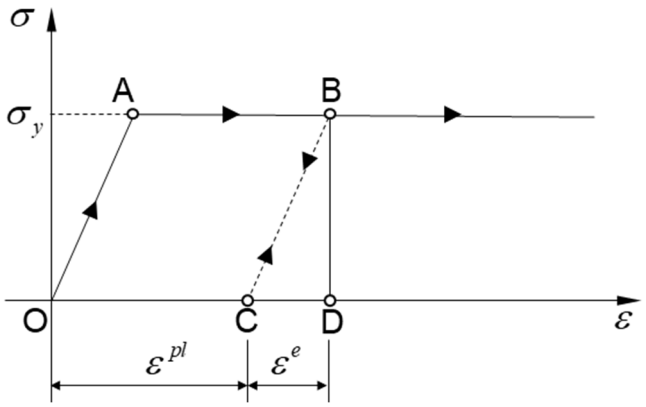


Figure 3.8: 1-D stress-strain relationship of elastic-perfectly plastic model

Following the description of the elastic-perfectly plastic model, the total increment of strain of a material is expressed as a sum of elastic and plastic strain increments

$$d\varepsilon_{ij} = d\varepsilon_{ij}^{e} + d\varepsilon_{ij}^{pl} \tag{3.24}$$

The elastic strain increment is linearly related to the stress increment via the elastic compliance constitutive tensor C_{ijkl}^{e}

$$d\varepsilon_{ij}^{e} = C_{ijkl}^{e} d\sigma_{kl} \tag{3.25}$$

Unlike in elasticity, there is no unique relationship of plastic strain increment to the stress increment in perfect plasticity. Instead, once yielding occurs (plastic state) the evolution of plastic strains is governed by a flow rule.

One can rewrite Eq. (3.24) by substituting Eq. (3.4) into Eq. (3.24) as

$$d\varepsilon_{ij} = C_{ijkl}^{e} d\sigma_{kl} + d\lambda \frac{\partial f}{\partial \sigma_{ij}} \tag{3.26}$$

The inverse relation can be derived starting from the increment of strain during elastic process

$$d\sigma_{ij} = D_{ijkl}^{e} d\varepsilon_{kl}^{e} = D_{ijkl}^{e} \left(d\varepsilon_{ij} - d\varepsilon_{kl}^{pl} \right) \tag{3.27}$$

where D_{ijkl}^{e} is the elastic-stiffness tensor. During elastic-perfectly plastic deformation, the stress state remains on the yield condition, with the latter being stationary in the stress space. Using the Prager consistency condition

$$df = \frac{\partial f}{\partial \sigma_{ij}} d\sigma_{ij} = 0 \tag{3.28}$$

and by substituting Eqs. (3.4) and (3.27) into Eq. (3.28), df can be rewritten as

$$df = \frac{\partial f}{\partial \sigma_{ij}} D_{ijkl}^{e} \, d\varepsilon_{kl} - \frac{\partial f}{\partial \sigma_{ij}} D_{ijkl}^{e} \, d\lambda \frac{\partial f}{\partial \sigma_{kl}} = 0 \tag{3.29}$$

The increment of the plastic multiplier λ can be found from Eq. (3.29)

$$d\lambda = \frac{\dfrac{\partial f}{\partial \sigma_{ij}} D^e_{ijkl} d\varepsilon_{kl}}{\dfrac{\partial f}{\partial \sigma_{pq}} D^e_{pqrs} \dfrac{\partial f}{\partial \sigma_{rs}}} \tag{3.30}$$

By substituting Eq. (3.30) into the plastic flow rule Eq. (3.4),

$$d\varepsilon^{pl}_{ij} = \frac{\dfrac{\partial f}{\partial \sigma_{ab}} D^e_{abkl} d\varepsilon_{kl}}{\dfrac{\partial f}{\partial \sigma_{pq}} D^e_{pqrs} \dfrac{\partial f}{\partial \sigma_{rs}}} \frac{\partial f}{\partial \sigma_{ij}} \tag{3.31}$$

Replacing $d\varepsilon^{pl}_{ij}$ in Eq. (3.31) into Eq. (3.27), one finds

$$d\sigma_{ij} = \left(D^e_{ijkl} - \frac{D^e_{ijpq} \dfrac{\partial f}{\partial \sigma_{pq}} \dfrac{\partial f}{\partial \sigma_{rs}} D^e_{rskl}}{\dfrac{\partial f}{\partial \sigma_{mn}} D^e_{mnwv} \dfrac{\partial f}{\partial \sigma_{wv}}} \right) d\varepsilon_{kl} \tag{3.32}$$

or

$$d\sigma_{ij} = D_{ijkl} d\varepsilon_{kl} \tag{3.33}$$

where D_{ijkl} is the elastic-perfectly plastic stiffness tensor. Eq. (3.33) defines the incremental constitutive relation for an elastic-perfectly plastic material.

A stress-strain relationship of elastic-plastic behavior with hardening is shown in Fig. 3.9. Stress-strain behavior is purely elastic along the segment OA, the material starts to yield at the yield stress σ_y. At the state of yielding, the material hardens, and this is represented by the positive inclination of segment AD. When the material is unloaded at point B, the stress path is along the segment BC, resulting in a point where the stress is nil, but an irreversible deformation ε^{pl}_{ij} remains.

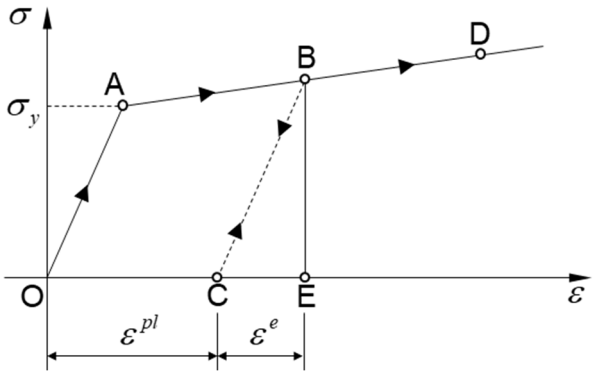


Figure 3.9: 1-D stress-strain relationship for elastic-plastic model with hardening

The Cam clay model will be used here as an example of a constitutive model with hardening/softening. This model was chosen here because it encapsulates many defining aspects of soil behavior, such as hardening and softening during plastic deformation, and *critical state* condition. *Critical state* is a state where soil deforms plastically at a constant volume without further loading increase. The early contributions to the development of the Cam clay model are found in Roscoe et al. (1958), Roscoe and Burland (1968), and Schofield and Wroth (1968).

The Cam clay model will be described using a set of triaxial stress components and increments of plastic strain components: mean effective stress p', deviatoric stress q, volumetric strain increment $d\varepsilon_p^{pl}$, and deviatoric strain increment $d\varepsilon_q^{pl}$ (superscript pl stands for plastic). Triaxial stress components can be defined by principal effective stresses

$$\begin{aligned} p' &= \frac{1}{3}(\sigma_1' + \sigma_2' + \sigma_3') \\ q &= \sigma_1' - \sigma_3' \end{aligned} \qquad (\sigma_1' \geq \sigma_2' \geq \sigma_3') \qquad (3.34)$$

Triaxial strain increment components can be defined by principal strain increments

$$\begin{aligned} d\varepsilon_p^{pl} &= d\varepsilon_1^{pl} + 2d\varepsilon_3^{pl} \\ d\varepsilon_q^{pl} &= \frac{2}{3}\left(d\varepsilon_1^{pl} - d\varepsilon_3^{pl}\right) \end{aligned} \qquad (3.35)$$

All normal stress components in this model are considered effective stresses.

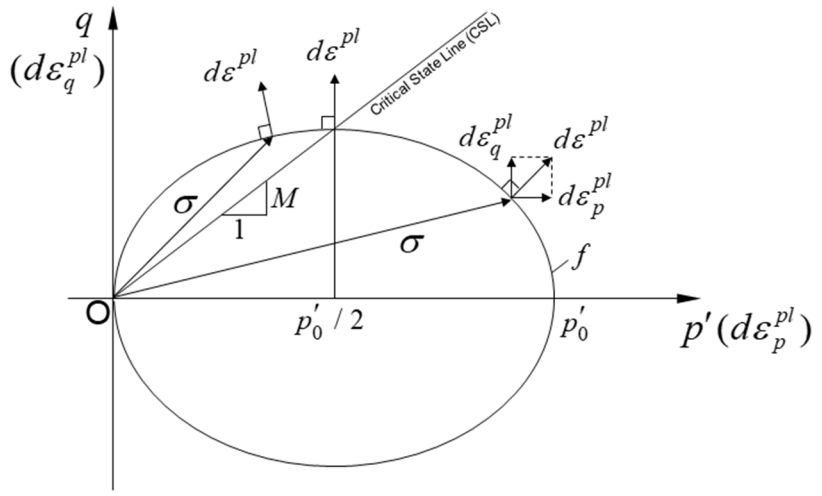


Figure 3.10: Yield surface in Cam clay model

The constitutive relationship within the elastic range is based on Hooke's law, which establishes a linear relationship between stress and elastic strain. When stress state σ is at the yield surface, soil can start yielding and deform plastically, Fig. 3.10. The yield surface is allowed to expand and contract as plastic deformation progresses, reflecting changes in the material's strength. Because the Cam clay model adopts the normality rule, the change in the yield surface size (and the hardening parameter) is governed by the plastic volumetric strain. When $d\varepsilon_p^{pl} > 0$, the yield surface contracts, and when $d\varepsilon_p^{pl} < 0$, it expands. As the yield surface expands or contracts with loading, the stress state will eventually reach the critical state line. The slope of the critical state line is denoted by *M*. When the stress state asymptotically reaches at the critical state line, the yield surface does not expand, but the soil deforms plastically at a constant volume without further loading. This asymptotic state is called the *critical state*, its comprehensive description is presented by Wood (1990).

The Cam clay model represents a specific formulation within the framework of critical state soil mechanics. The constitutive relation for a more general critical state model is needed to generalize this concept. Increments of triaxial stress invariants dp', dq and plastic strain increments $d\varepsilon_p^{pl}$, $d\varepsilon_q^{pl}$ are used for the derivation. Let the yield function $f = 0$ depend on a hardening parameter p_0'. p_0' is considered here as a general hardening parameter that governs the

size of the yield surface. First, consider a general case where hardening parameter p_0' depends on triaxial plastic strain components $\varepsilon_p^{pl}, \varepsilon_q^{pl}$

$$p_0' = p_0'(\varepsilon_p^{pl}, \varepsilon_q^{pl}) \tag{3.36}$$

hence, the total differential of p_0' is

$$dp_0' = \frac{\partial p_0'}{\partial \varepsilon_p^{pl}} d\varepsilon_p^{pl} + \frac{\partial p_0'}{\partial \varepsilon_q^{pl}} d\varepsilon_q^{pl} \tag{3.37}$$

With an assumption of the associative flow rule, plastic strain increment components read

$$\begin{aligned} d\varepsilon_p^{pl} &= d\lambda \frac{\partial f}{\partial p'} \\ d\varepsilon_q^{pl} &= d\lambda \frac{\partial f}{\partial q} \end{aligned} \tag{3.38}$$

where $d\lambda$ is a plastic multiplier. Hardening/softening parameter p_0', effective mean stress p', and deviatoric stress q. The general form of the yield conditions is

$$f(p', q, p_0') = 0 \tag{3.39}$$

Using the Prager consistency condition, $df = 0$, which ensures that the stress state remains on the yield surface during plastic flow, one can find

$$df = \frac{\partial f}{\partial p'} dp' + \frac{\partial f}{\partial q} dq + \frac{\partial f}{\partial p_0'} dp_0' = 0 \tag{3.40}$$

Substituting Eq. (3.38) into (3.37) leads to the total differential of p_0' with the plastic multiplier as one of the variables

$$dp_0' = \frac{\partial p_0'}{\partial \varepsilon_p^{pl}} d\lambda \frac{\partial f}{\partial p'} + \frac{\partial p_0'}{\partial \varepsilon_q^{pl}} d\lambda \frac{\partial f}{\partial q} = d\lambda \left(\frac{\partial p_0'}{\partial \varepsilon_p^{pl}} \frac{\partial f}{\partial p'} + \frac{\partial p_0'}{\partial \varepsilon_q^{pl}} \frac{\partial f}{\partial q} \right) \tag{3.41}$$

By substituting Eq. (3.41) into (3.40), increment of the plastic multiplier $d\lambda$ reads

$$d\lambda = \frac{\frac{\partial f}{\partial p'} dp' + \frac{\partial f}{\partial q} dq}{-\frac{\partial f}{\partial p_0'} \left(\frac{\partial p_0'}{\partial \varepsilon_p^{pl}} \frac{\partial f}{\partial p'} + \frac{\partial p_0'}{\partial \varepsilon_q^{pl}} \frac{\partial f}{\partial q} \right)} = \frac{1}{H} \left(\frac{\partial f}{\partial p'} dp' + \frac{\partial f}{\partial q} dq \right) \tag{3.42}$$

where the hardening modulus H is defined as

$$H = -\frac{\partial f}{\partial p_0'} \left(\frac{\partial p_0'}{\partial \varepsilon_p^{pl}} \frac{\partial f}{\partial p'} + \frac{\partial p_0'}{\partial \varepsilon_q^{pl}} \frac{\partial f}{\partial q} \right) \tag{3.43}$$

Substituting Eq. (3.42) into flow rule (3.38), plastic strain increments are found as a function of volumetric and deviatoric stress increments, dp' and dq

$$\begin{Bmatrix} d\varepsilon_p^{pl} \\ d\varepsilon_q^{pl} \end{Bmatrix} = \frac{1}{H} \begin{bmatrix} \frac{\partial f}{\partial p'} \frac{\partial f}{\partial p'} & \frac{\partial f}{\partial q} \frac{\partial f}{\partial p'} \\ \frac{\partial f}{\partial p'} \frac{\partial f}{\partial q} & \frac{\partial f}{\partial q} \frac{\partial f}{\partial q} \end{bmatrix} \begin{Bmatrix} dp' \\ dq \end{Bmatrix} \tag{3.44}$$

The constitutive relation of elastic strain increments to stress reads

$$\begin{Bmatrix} d\varepsilon_p^{el} \\ d\varepsilon_q^{el} \end{Bmatrix} = \begin{bmatrix} \frac{1}{K'} & 0 \\ 0 & \frac{1}{3G'} \end{bmatrix} \begin{Bmatrix} dp' \\ dq \end{Bmatrix} \tag{3.45}$$

where K' is the elastic bulk modulus and G' is the elastic shear modulus. For an isotropic soil can be written in terms of the Young's modulus E' and Poisson's ratio ν

$$K' = \frac{E'}{3(1-2\nu)}, \quad G' = \frac{E'}{2(1+\nu)} \tag{3.46}$$

By combining elastic and plastic components of each strain increment, this is a constitutive relation of strain increments to stress

$$\begin{Bmatrix} d\varepsilon_p \\ d\varepsilon_q \end{Bmatrix} = \begin{bmatrix} \frac{1}{K'} + \frac{1}{H}\frac{\partial f}{\partial p'}\frac{\partial f}{\partial p'} & \frac{1}{H}\frac{\partial f}{\partial q}\frac{\partial f}{\partial p'} \\ \frac{1}{H}\frac{\partial f}{\partial p'}\frac{\partial f}{\partial q} & \frac{1}{3G'} + \frac{1}{H}\frac{\partial f}{\partial q}\frac{\partial f}{\partial q} \end{bmatrix} \begin{Bmatrix} dp' \\ dq \end{Bmatrix} \tag{3.47}$$

The constitutive relation presented in Eq. (3.47) is for the case where hardening parameter p_0' is a function of both the volumetric and the deviatoric plastic strain. Unlike for metals, however, the deviatoric component of plastic strain has a negligible effect on the hardening of soils when compared to the effect of the volumetric plastic strain. Consequently, the hardening modulus *H* in the constitutive relation in Eq. (3.43), when specified for Cam clay, is defined as

$$H = -\frac{\partial f}{\partial p_0'}\frac{\partial p_0'}{\partial \varepsilon_p^{pl}}\frac{\partial f}{\partial p'} \tag{3.48}$$

Consider a case of triaxial compression test for lightly preconsolidated soil. Assuming the specimen was preconsolidated at pressure p_{01}', the current yield function $f_1 = 0$ of the material is

defined by the hardening parameter $p'_{01} = p'$, Fig. 3.11. After preconsolidation, the specimen was unloaded to the stress state at point A. It was subsequently reloaded in triaxial compression along the unloading-reloading line AB until point B was reached, and further loaded toward point C, where the critical state is asymptotically approached. During this process, the yield surface expands as plastic volumetric compression occurs, with the hardening parameter p'_0 increasing from p'_{01} toward p'_{03}.

At stress state A, the current yield function $(f_1 = 0)$ of the material is defined by the hardening parameter $p'_{01} = p'$, Fig. 3.11(a). Loading path AB in a conventional compression test has a slope of $dq / dp' = 3$. Along the loading path AB, the soil specimen behaves elastically. Elastic behavior of the specimen is captured on plane q and ε_q as a linear segment AB, Fig. 3.11(b). The change in specific volume *v* as a function of p' is presented along with isotropic normal consolidation and unloading-reloading lines in Fig. 3.11(c). The specific volume *v* is defined as the total volume per volume of solids. It can be expressed as $v = 1 + e$, where *e* is the void ratio. During the initial preconsolidation, the path follows the isotropic normal consolidation line. Upon unloading to A, the stress path follows unloading-reloading line for stress state inside $f_1 = 0$. Along the path AB, the soil specimen follows the same unloading-reloading line. As the specimen is loaded further along path BC, the yield surface expands to $f_3 = 0$. Hardening parameter p'_0 that determines the size of the yield surface increases, $p'_0 \rightarrow p'_{03}$, causing expansion of the yield surface. Point C is reached asymptotically while volumetric strain increments tend to zero. Point C represents the critical stress state where volumetric strains cease, with deviatoric strain increasing without further increase in stress, Fig. 3.11(b).

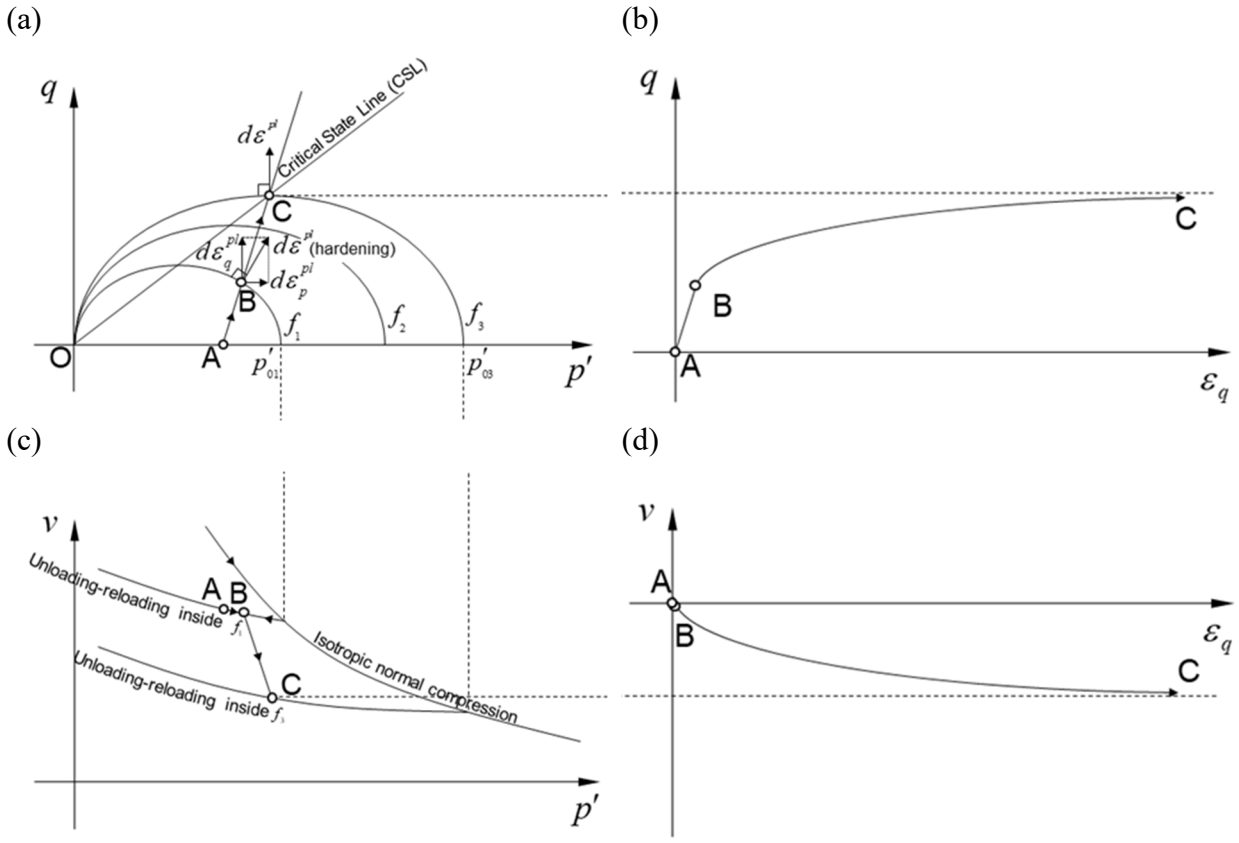


Figure 3.11: Conventional triaxial compression test for lightly preconsolidated clay using Cam clay model: (a) yield surfaces on plane $p'-q$, (b) deviatoric stress-strain response, (c) relationship between specific volume v and effective mean stress p', and (d) relationship between specific volume v and deviatoric strain ε_q

Consider now a case of a triaxial compression test for overconsolidated soil. Assuming the specimen was preconsolidated at pressure p'_{01} and then unloaded to stress state A, resulting in an overconsolidated condition, Fig. 3.12. It is loaded in triaxial compression, along the unloading-reloading line until the strength is reached at point B. Point B is the instability point where the soil specimen loses stability, leading to a reduction in deviatoric stress beyond this point. In this overconsolidated condition, the soil exhibits a dilative response during shear, and the yield surface gradually contracts in the $p'-q$ plane, Fig. 3.12(a). As the test continues, the stress state approaches point C, which is on the critical state line. Point C is approached asymptotically with no further change in volume, while shear strain continues to develop.

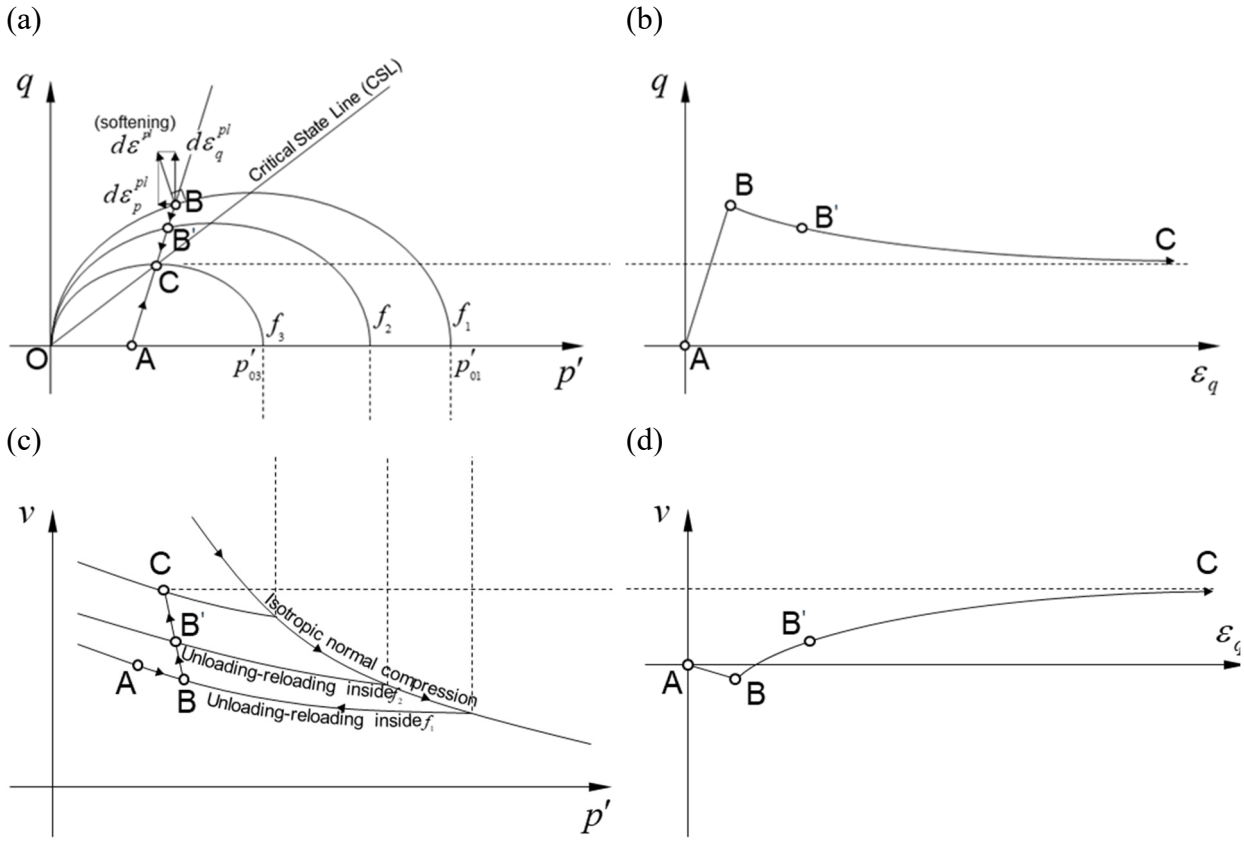


Figure 3.12: Conventional triaxial compression test for overconsolidated clay using Cam clay model: (a) yield surfaces on plane $p'-q$, (b) deviatoric stress-strain response, (c) relationship between specific volume v and effective mean stress p', and (d) relationship between specific volume v and deviatoric strain ε_q

In summary, plasticity theory provides a framework for interpreting the stress-strain response of geomaterials, encompassing yielding, hardening/softening, plastic flow, and the critical state. Experimental evidence shows that real geomaterials do not obey the associative flow rule, exhibiting non-associative flow. This evidence necessitates stability analysis methods that can incorporate non-associative flow rule.

Chapter 4 Limit Analysis

Limit analysis provides a powerful theoretical framework to estimate the limit load of geotechnical systems. Limit analysis assumes the convexity of the yield condition and the associative plastic flow rule. The method relies on two complementary formulations: the static (lower-bound) theorem and the kinematic (upper-bound) theorem. The static theorem involves constructing stress fields that satisfy stress equilibrium and stress boundary conditions without violating the yield condition. The kinematic theorem involves constructing velocity (strain rate) fields that satisfy the normality flow rule and the velocity boundary conditions.

4.1 Admissible stress fields and mechanisms

The static theorem of limit analysis requires a statically admissible stress field that satisfies boundary conditions and equilibrium without violating the yield criterion. The kinematic theorem of limit analysis requires a kinematically admissible velocity field (or mechanism) that fulfills boundary condition and flow rule requirements.

Consider a case of a shallow foundation on an incompressible, weightless soil. The footing is a surface footing, and traction p is the unknown limit load of the foundation. Fig. 4.1(a) illustrates an example of an admissible stress field in the foundation soil. The soil domain is divided into several regions, which are symmetric with respect to the centerline of the footing. Stress states in regions A, B, C, D, E, and F are shown in Fig. 4.1(b).

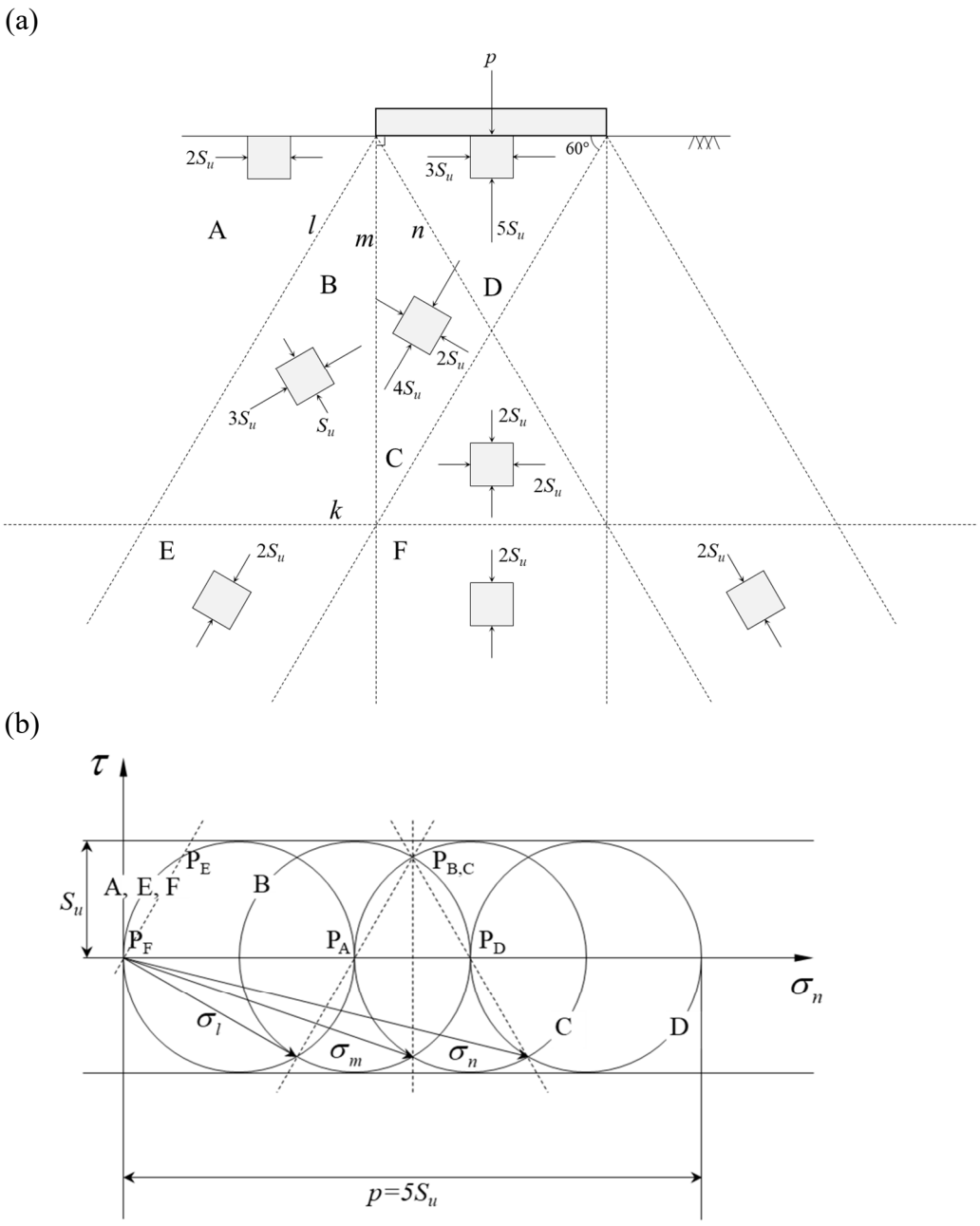


Figure 4.1: (a) Admissible plastic stress field for a shallow footing problem, and (b) plastic stress states in the respective regions

In this stress field, lines *l*, *m*, *n*, and *k* are discontinuity lines that divide the soil domain, which extends into the infinite half-space. In region A, the minor principal stress is 0, and the major principal stress, $2S_u$, can be found using the Mohr circle and the yield function. Stress σ_l acts on line *l* that divides regions A and B. Regions A and B share line *l,* so that the stress state of region B

can be obtained using stress σ_l and the yield function. In the same manner, the stress state in each region can be obtained. The major principal stress p is the static solution to the bearing capacity of the shallow footing.

An admissible mechanism (or kinematically admissible velocity field) represents a possible pattern of deformation that is compatible with the boundary conditions and the associative plastic flow rule. Consider now a shallow foundation on a weightless soil that satisfies the Mohr-Coulomb yield criterion and follows the associative flow rule. The soil is subjected to a vertical overburden of q at the free boundary. Fig. 4.2(a) illustrates an example of an admissible mechanism in shallow foundation soil. The boundary conditions are such that the soil block ABC moves together with the foundation at a uniform velocity of v_0, while the soil surface is treated as a free boundary. Lines AC, BC, BD, CD, and DE are velocity discontinuities, while lines AC, BC, and BD divide the half of the soil domain into three regions. Fig. 4.2(b) shows a closed diagram of velocities, and each velocity in the hodograph corresponds to the velocities in Fig. 4.2(a). These velocities are not constants but incipient velocities at the moment of yielding (plastic state).

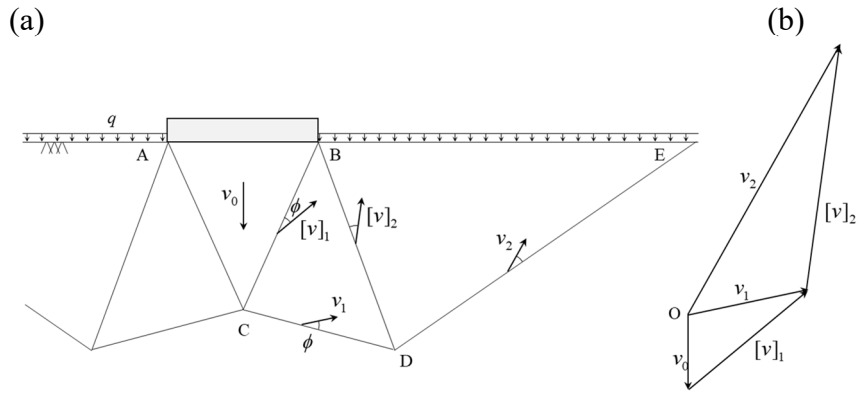


Figure 4.2: (a) Admissible mechanism of a shallow foundation problem, and (b) hodograph

In Fig. 4.2(a), soil block ABC moves downward. Block BCD slides relative to block ABC along the line BC, and block BDE slides relative to block BCD along the line BD. Lines BC and BD are velocity discontinuities between soil blocks, so that velocities $[v]_1$ and $[v]_2$ are velocity jumps at those lines. Those velocity jumps are inclined at an angle of friction ϕ. Lines CD and DE represent the boundaries between the yielding soil blocks and the surrounding stationary soil. Lines CD and DE are velocity discontinuities because the soil inside the mechanism is assumed to move as rigid

blocks while the soil outside remains at rest. Velocities at those discontinuities, v_1 and v_2, are inclined at an angle of friction ϕ. Such boundaries act as failure surfaces, where plastic shear strain localizes. Directions of velocities obtained from the mechanism are used to construct the hodograph by adjusting their magnitudes. All velocities can be expressed as a homogeneous function of order one with respect to the magnitude of v_0, so that relative magnitudes and directions of the velocity components need to be considered in the limit analysis.

4.2 Theorems of limit analysis

Fig. 4.3(a) shows a continuum body that is in equilibrium. The body has volume *V*, and is subjected to body force *X* and surface traction *T*. The surface traction acts on the surface *S*. σ represents a stress state at one point within the structure. The surface traction can be obtained by a dot product of σ and *n* where *n* is the unit outward normal vector. Fig. 4.3(b) shows the plastic deformation of the same body, characterized by a strain rate of $\dot{\varepsilon}$ and a velocity of *v*, each representing the state at a point within the structure. Fig. 4.3(a) and Fig. 4.3(b) provide two separate and unrelated sets: stress field and kinematic field.

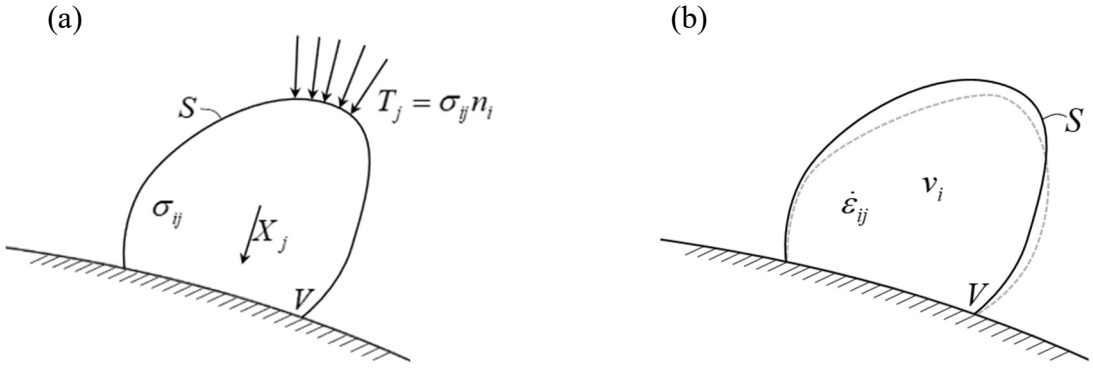


Figure 4.3: (a) Continuum body subjected to surface traction and body force, and (b) plastic deformation of the continuum body

Although the stress field and kinematic field are unrelated, they are brought together but independently, in the equation of virtual work. The principle of virtual work states that, for any virtual velocity field that is admissible, the rate of work done by the external loads must be equal

to the rate of internal work dissipated by the true stress within the body. Likewise, the same relation holds if the admissible stress field is taken as virtual and the velocity fields represents the true state of deformation. This principle is valid only when σ_{ij} is in equilibrium. The principle of virtual work can be mathematically expressed as

$$\int_V \sigma_{ij}\dot{\varepsilon}_{ij}dV = \int_S T_j v_j dS + \int_V X_j v_j dV \tag{4.1}$$

Fig. 4.4 shows yield function $f(\sigma_{ij}) = 0$, admissible stress tensor σ_{ij}^s, true plastic stress tensor σ_{ij}, and strain rate $\dot{\varepsilon}_{ij}$ that corresponds to σ_{ij}. σ_{ij}^s and σ_{ij} represent a stress state at each point within the structure. σ_{ij}^s is admissible so that it satisfies the stress equilibrium, boundary conditions, and does not violate the convex yield surface.

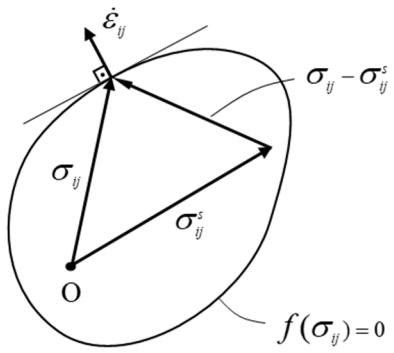


Figure 4.4: Yield function, stress, and strain rate for the lower-bound approach of limit analysis

The principle of virtual work written for admissible stress field σ_{ij}^s and true velocity field v_i is

$$\int_V \sigma_{ij}^s\dot{\varepsilon}_{ij}dV = \int_S T_i^s v_i dS + \int_V X_i v_i dV \tag{4.2}$$

where T_i^s is the traction on the surface of the structure, associated with σ_{ij}^s. By subtracting Eq. (4.2) from the principle of virtual work written for the true solution to a problem (Eq. 4.1) one obtains

$$\int_V \left(\sigma_{ij} - \sigma_{ij}^s\right)\dot{\varepsilon}_{ij} dV = \int_S \left(T_i - T_i^s\right) v_i dS \tag{4.3}$$

stress $\sigma_{ij} - \sigma_{ij}^s$ and strain rate $\dot{\varepsilon}_{ij}$ in Fig. 4.4 show that the following inequality is correct

$$(\sigma_{ij} - \sigma_{ij}^s)\dot{\varepsilon}_{ij} \geq 0 \tag{4.4}$$

This is a postulate of maximum plastic work; due to the convexity of the yield function and associativity, the true plastic work is the maximum among all plastic works corresponding to any admissible stress field. Since the left-hand side of Eq. (4.3) is greater than or equal to zero, the right-hand side of the equation is also greater than or equal to zero

$$\int_S T_i v_i dS \geq \int_S T_i^s v_i dS \tag{4.5}$$

The rate of work by true active traction T_i is not smaller than the rate of work by active traction T_i^s. The active limit load obtained from any statically admissible stress field bounds the true limit load from below, so that it is often called the lower-bound theorem. The lower-bound theorem of limit analysis states that the load corresponding to any statically admissible stress field cannot exceed the true collapse load. One can substitute inequality (4.5) into Eq. (4.2) to obtain an alternative form of the theorem

$$\int_V \sigma_{ij}^s \dot{\varepsilon}_{ij} dV \leq \int_S T_i v_i dS + \int_V X_i v_i dV \tag{4.6}$$

Fig. 4.5 shows yield function $f(\sigma_{ij})=0$, true plastic stress tensor σ_{ij}, kinematically admissible strain rate $\dot{\varepsilon}_{ij}^{k}$, and plastic stress tensor σ_{ij}^{k} that corresponds to $\dot{\varepsilon}_{ij}^{k}$. Strain rate $\dot{\varepsilon}_{ij}^{k}$ associated with σ_{ij}^{k}, satisfies kinematic boundary conditions and the associative flow rule. $\dot{\varepsilon}_{ij}^{k}$ represents a strain rate at one point within the structure.

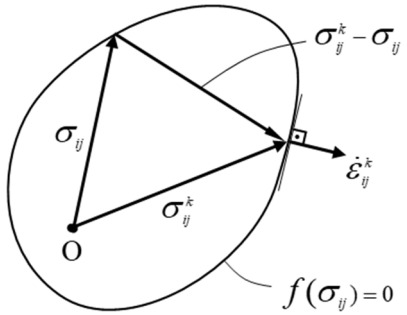


Figure 4.5: Yield function, stress, and strain rate for the upper-bound approach of limit analysis

The balance of work is valid for true stress field σ_{ij} and kinematically admissible kinematic field $\dot{\varepsilon}_{ij}^{k}$ (or v_i^k). The principle of virtual work written for a true stress field and a kinematically admissible velocity field is

$$\int_V \sigma_{ij}\dot{\varepsilon}_{ij}^{k}dV=\int_S T_i\, v_i^k dS+\int_V X_i v_i^k dV \tag{4.7}$$

The balance of work applied to the kinematically admissible mechanism v_i^k and stress field σ_{ij}^{k}

$$\int_V \sigma_{ij}^{k}\dot{\varepsilon}_{ij}^{k}dV=\int_S T_i^k v_i^k dS+\int_V X_i v_i^k dV \tag{4.8}$$

where T_i^k is a traction on the surface of the material, associated with the kinematically admissible mechanism and v_i^k is the kinematically admissible velocity field. By subtracting Eq. (4.7) from Eq. (4.8),

$$\int_V \left(\sigma_{ij}^k - \sigma_{ij}\right)\dot{\varepsilon}_{ij}^k dV = \int_S \left(T_i^k - T_i\right)v_i^k dS \tag{4.9}$$

Stress $\sigma_{ij}^k - \sigma_{ij}$ and strain rate $\dot{\varepsilon}_{ij}^k$ in Fig. 4.5 show that the following inequality is correct due to the convexity of the yield function and associativity

$$(\sigma_{ij}^k - \sigma_{ij})\dot{\varepsilon}_{ij}^k \geq 0 \tag{4.10}$$

Since the left-hand side of Eq. (4.9) is greater than or equal to zero, the right-hand side of the equation is also greater than or equal to zero.

$$\int_S T_i^k v_i^k dS \geq \int_S T_i v_i^k dS \tag{4.11}$$

The rate of work by active traction T_i^k is not smaller than the rate of work by true active traction T_i in any kinematically admissible mechanism. The limit load obtained from any kinematically admissible velocity field bounds the true limit load from above, so that it is often called the upper-bound theorem. The upper-bound theorem of limit analysis states that the load corresponding to any kinematically admissible velocity field cannot be smaller than the true collapse load. One can substitute inequality (4.11) into Eq. (4.8) to obtain an alternative form of the theorem

$$\int_V \sigma_{ij}^k \dot{\varepsilon}_{ij}^k dV \geq \int_S T_i v_i^k dS + \int_V X_i v_i^k dV \tag{4.12}$$

4.3 Limit analysis for non-associative soils and rock masses

Classical limit analysis theorems are rigorously valid for perfectly plastic materials with the associative flow rule. As discussed in Section 3.1, geomaterials generally conform to non-

associative plastic flow rule, and authors, including Radenkovic, Josselin de Jong, Palmer, and Saxcé, have attempted to extend the limit analysis theorems to such non-associative materials. Radenkovic (1962) proposed two theorems of limit analysis for non-associative materials. The first theorem states that the limit load of the structure made of a non-associative material is bounded from above by the limit load of the structure made of an associative material having the same yield surface. The proof comes from the fact that the true plastic stress field of the non-associative material is also admissible for the associative material, so the dissipation inequality implied by the postulate of maximum plastic work in the associative material leads to an upper-bound on the true limit load, see inequality (4.11). Radenkovic's second theorem states that if there exists convex function $g(\sigma_{ij}) = 0$ that lies entirely inside yield surface $f(\sigma_{ij}) = 0$, and if the plastic strain rate is normal to surface $g(\sigma_{ij}) = 0$, then the collapse load of the structure made of the non-associative material is bounded from below by the limit load of the structure made of the associative material defined by the yield function, $g(\sigma_{ij}) = 0$. Despite the theoretical significance of Radenkovic's contribution, the practicality of his theorems is limited. The first theorem does not make it possible to obtain the non-associative solutions. The second theorem was later expanded by Josselin de Jong (1964) and Palmer (1966).

Josselin de Jong (1964) demonstrated that when the material follows non-associative flow rule, the material can produce negative dissipation under certain loading paths. He argued that the set of stress states must be restricted to a smaller region inside the yield surface so that such negative dissipation is prevented, and only within this reduced domain can a lower-bound on the limit load be ensured. Palmer (1966) subsequently gave an alternative formulation of such lower-bound theorem of limit analysis for non-associative materials. Palmer demonstrated how to construct the surface, $g(\sigma_{ij}) = 0$, in the conjugate spaces of stress and plastic strain rate, Fig. 4.6. In this approach, the yield surface simply replaced by the potential function. Radenkovic's theorems and extensions have broadened the theoretical framework for non-associative soils. However, when they are applied to the Mohr-Coulomb yield criterion, their practical value is limited. Radenkovic's first theorem reduces to computing the classical associative solution. The second theorem, when combined with an incompressibility condition ($\vartheta = 0°$), yields a trivial solution of zero.

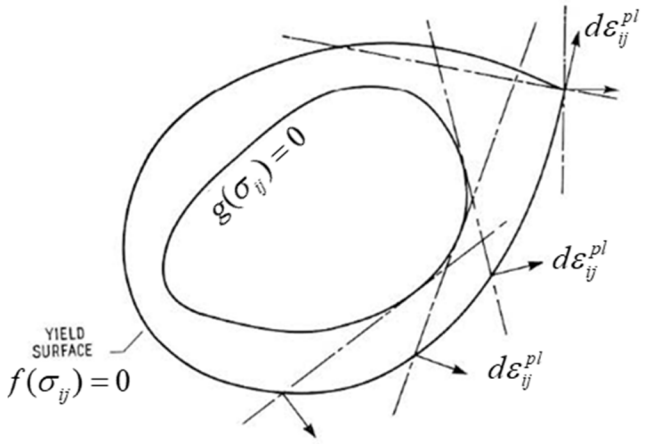


Figure 4.6: Construction of plastic potential (g-function) using yield surface and strain increments (from Palmer 1966)

Saxcé and co-workers (e.g., Saxcé and Bousshine 1998, Chaaba et al 2010) proposed a different approach by introducing the concept of bipotential, a dissipation function that unifies the yield condition and the flow rule. In this framework, plastic flow rule is not described by a yield surface and a separate plastic potential, but instead by a single bipotential function. The bipotential framework allows the non-associative Mohr-Coulomb model to be expressed in a form that resembles standard material, even though the strain rate is not normal to the yield function. This construction allows the non-associative flow rule to be treated in a variational form analogous to that of associative flow rule. In practice, however, the bipotential function must be explicitly constructed for the material under consideration, a mathematically demanding task that limits the method to relatively simple or idealized problems. Moreover, implementations of the bipotential framework typically rely on iterative coupling between stresses and kinematics, and convergence of the process may fail or become unstable. These challenges highlight that the framework is mostly limited to simple or idealized problems, remaining difficult to apply to a wide range of geotechnical boundary value problems.

From a practical geomechanics standpoint, the most influential contribution to upper-bound limit analysis of non-associative material is due to Davis (1968). Davis originated a technique to utilize the upper-bound approach of limit analysis to non-associative soil by defining tractions on velocity characteristics. Michalowski (1989) indicated the equivalency of the work balance equation and force equilibrium in translational rigid-body mechanisms. Based on the

contributions by Davis and Michalowski, Drescher and Detournay (1993) presented a technique to apply the kinematic (upper-bound) theorem of limit analysis to non-associative soils, as long as the collapse mechanism has a rigid-body translational pattern. The equivalency of the work balance and force equilibrium is demonstrated here using a quadrangle block in Fig. 4.7(a) translating with velocity v, surrounded by other blocks separated by velocity discontinuities with velocity jumps $[v]_i$ and tractions T_i.

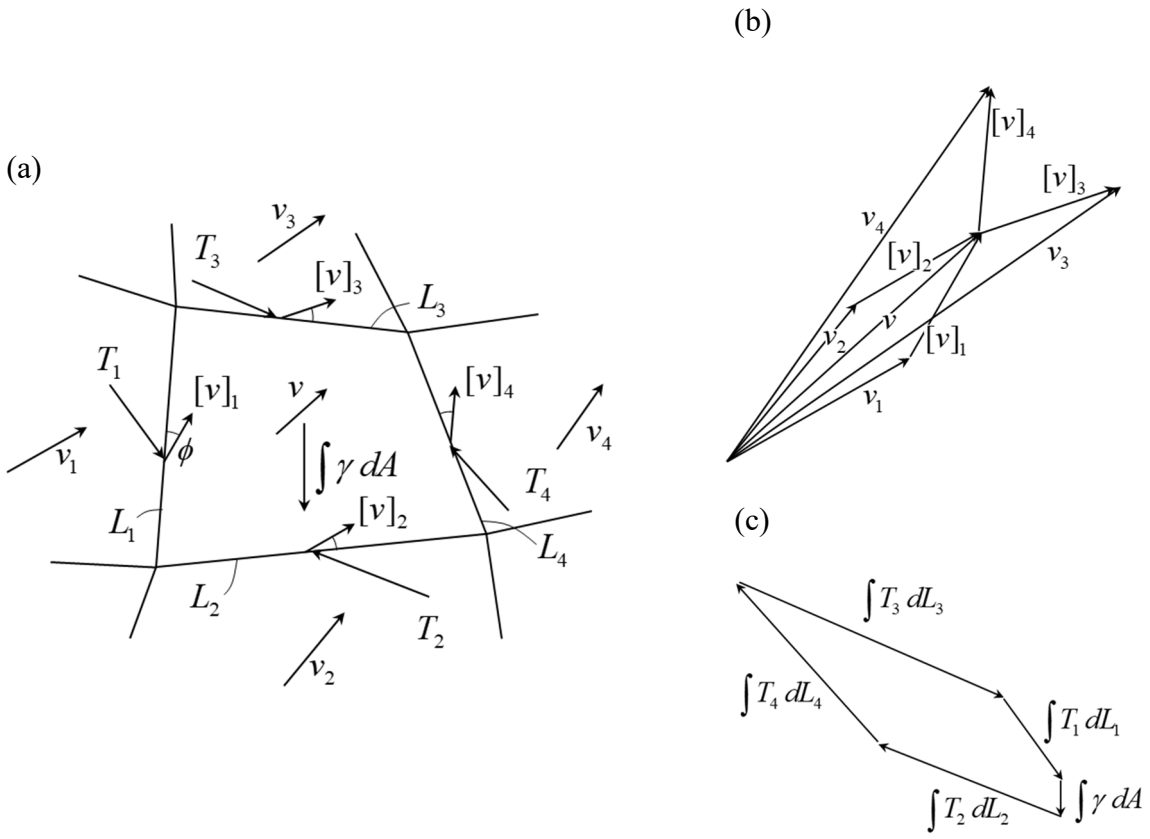


Figure 4.7: (a) Rigid quadrangle block with tractions, velocities, and velocity jumps, (b) hodograph, and (c) polygon of forces

Fig. 4.7 (b) shows the hodograph of the translating quadrangle and the velocities of neighboring blocks. Relationships of block velocities and velocity jumps are

$$\begin{aligned} v_1 + [v]_1 &= v \\ v_2 + [v]_2 &= v \\ v_3 - [v]_3 &= v \\ v_4 - [v]_4 &= v \end{aligned} \tag{4.13}$$

The balance of internal work rate and external work rate is written for the block as

$$\begin{aligned} &-[v]_1 \int_{L_1} T_1 dL - [v]_2 \int_{L_2} T_2 dL + [v]_3 \int_{L_3} T_3 dL + [v]_4 \int_{L_4} T_4 dL \\ &= v_1 \int_{L_1} T_1 dL + v_2 \int_{L_2} T_2 dL + v_3 \int_{L_3} T_3 dL + v_4 \int_{L_4} T_4 dL + v \int_{A} \gamma dA \end{aligned} \tag{4.14}$$

By substituting Eq. (4.13) into Eq. (4.14), it yields

$$v \left[\int_{L_1} T_1 dL + \int_{L_2} T_2 dL + \int_{L_3} T_3 dL + \int_{L_4} T_4 dL + \int_{A} \gamma dA \right] = 0 \tag{4.15}$$

Because the rate of work in Eq. (4.15) must be zero for any v, it follows that

$$\int_{L_1} T_1 dL + \int_{L_2} T_2 dL + \int_{L_3} T_3 dL + \int_{L_4} T_4 dL + \int_{A} \gamma dA = 0 \tag{4.16}$$

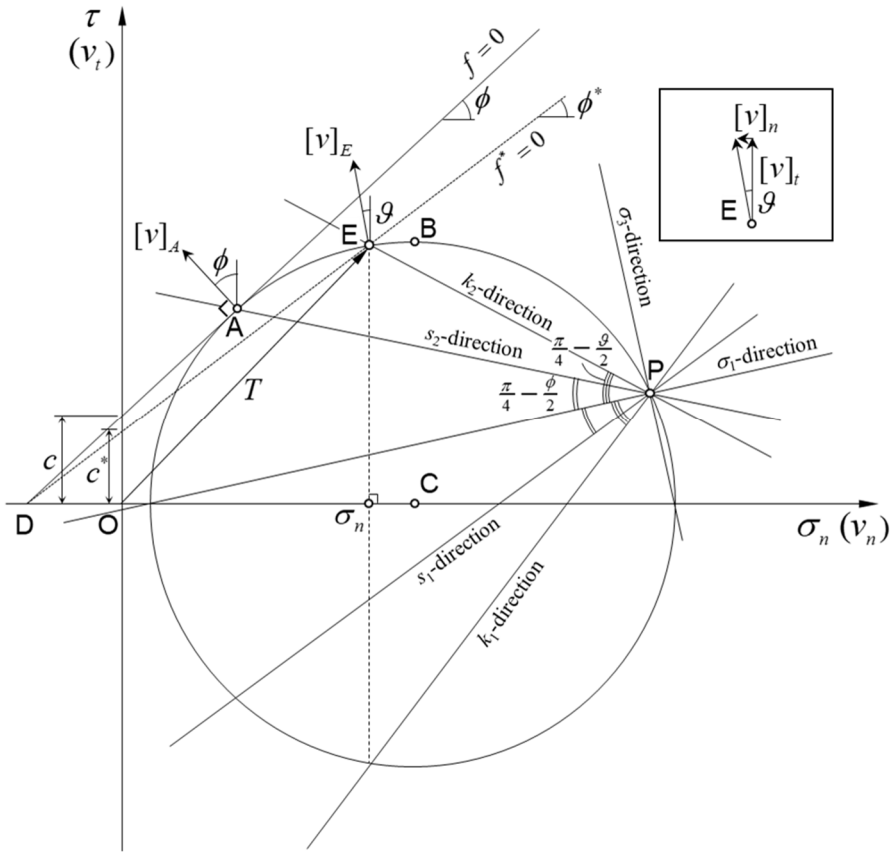


Figure 4.8: Tractions and velocity jumps for Mohr-Coulomb yield criterion with associative and non-associative flow rule

Fig. 4.8 presents the Mohr-Coulomb yield criterion, $f(\sigma,\tau)=0$ and a stress state that reached the yield criterion (plastic stress state). The pole is at point P and the model is coaxial. Associative flow is represented by the velocity jump $[v]_A$ located at point A ($\vartheta=\phi$) and non-associative flow is represented by $[v]_E$ located at point E on sector AB ($\vartheta\le\phi$). Point A is identified by the stress characteristic line, s_2, and point E is identified by the velocity characteristic line, k_2. Velocity discontinuities are admissible only on velocity characteristic lines, and the orientation of traction on these discontinuities depends on the degree of non-associativity measured by the dilatancy angle ϑ relative to internal friction angle ϕ. Traction for associative material is located at point A in Fig. 4.8, while that for non-associative material is located at point E. Hence, the rate of energy dissipation along the discontinuities is different for associative and non-associative materials. The

rate of energy dissipation in non-associative materials is obtained by taking the dot product of T and $[v]_E$, Fig. 4.8. It yields

$$T_i[v]_i = [v]\cos\vartheta[c^* + \sigma_n(\tan\phi^* - \tan\vartheta)] \tag{4.17}$$

in which σ_n is a normal component of stress at point E, and c^* and ϕ^* are parameters that define $f^* = \tau - c^* - \sigma_n \tan\phi^* = 0$, Fig. 4.7. However, σ_n is unknown in general, so that the calculation of the rate of energy dissipation using Eq. (4.17) is not feasible.

When dealing with rigid translational mechanisms, the limit load is dependent on the force equilibrium (Eq. 4.16). Hence, limit analysis for non-associative materials with a rigid translation mechanism can be thought of as using a fictitious Mohr-Coulomb yield criterion (Davis 1968) and the associative flow rule. To obtain c^* and ϕ^* as functions of ϑ and ϕ, two triangles DAC and DEC sharing a segment CD, Fig. 4.8, are compared. Using the law of sines on the triangles leads to

$$\frac{1}{\sin\phi} = \frac{\cos(\phi^* - \vartheta)}{\sin\phi^*} \tag{4.18}$$

Expressing the Eq. (4.18) in terms of the relationship between ϕ, ϕ^*, and ϑ leads to formulas for tan ϕ^* and c^*, satisfying

$$\begin{aligned} \tan\phi^* &= \frac{\cos\vartheta\cos\phi}{1-\sin\vartheta\sin\phi}\tan\phi \\ c^* &= \frac{\cos\vartheta\cos\phi}{1-\sin\vartheta\sin\phi}c \end{aligned} \tag{4.19}$$

The terms c^* and ϕ^* are used to describe the yield criterion of *substitution material*. This hypothetical material is introduced to address how non-associative soils can be analyzed within a framework that was developed for associative flow rules. For coaxial non-associative materials, the Mohr-Coulomb yield criterion and velocity relation for substitution material at the discontinuities satisfy

$$\tau = \sigma \tan \phi^* + c^*$$
$$[v]_n = [v]_t \tan \vartheta \tag{4.20}$$

The concept of substitution material enables using the kinematic limit analysis for non-associative material by replacing material parameters in the Mohr-Coulomb yield condition, cohesion c and internal friction angle ϕ, with fictitious values c^* and ϕ^* accounting for dilation angle ϑ. The rate of energy dissipation on velocity discontinuities can now be expressed as

$$T_i [v]_i = c^* [v] \cos \phi^* \tag{4.21}$$

The method for implementing non-associativity in limit analysis from rigid block translation mechanisms can be extended to continual deformation mechanisms. As an example, the Prandtl-type failure mechanism (Prandtl 1920) and the multi-block mechanism to compute bearing capacity factors N_c and N_q for strip footings are shown. These factors N_c and N_q are dimensionless bearing capacity parameters that represent the contributions of soil cohesion and surcharge load, respectively, calculated under the condition of weightless soil. The symmetric half of the mechanisms and hodographs for weightless soil with $\phi = 35°$ are illustrated in Fig. 4.9. As the number of blocks in rigid block translation increases, the geometry of the mechanism converges to the continual deformation pattern.

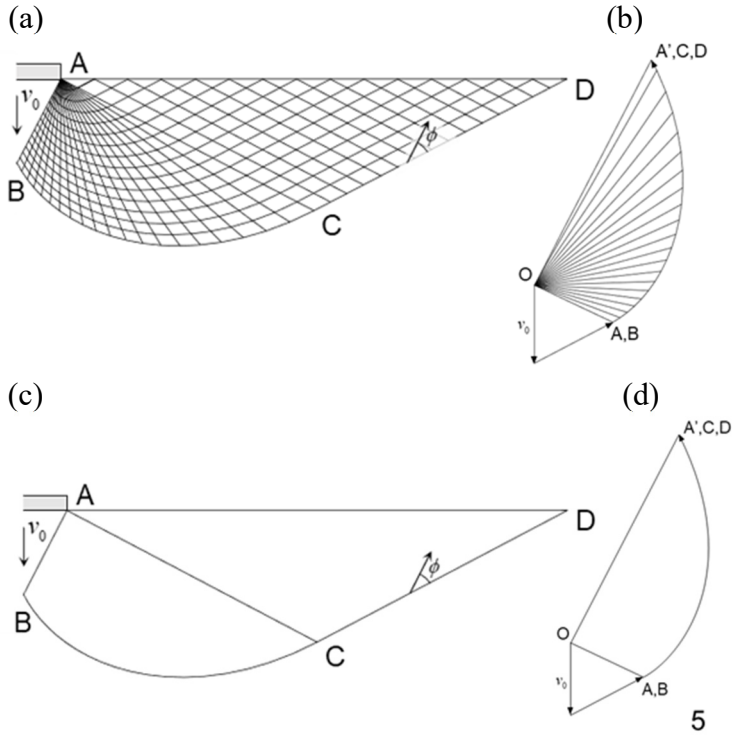


Figure 4.9: Prandtl-type mechanism for calculation of N_c and N_q; (a) rigid block translation, (b) hodograph, (c) continual deformation, and (d) its hodograph

As the number of blocks in rigid block translation increases, the obtained N_c and N_q converges to their true solutions. Relationships between the number of blocks and the obtained N_c and N_q after optimization are presented in Fig. 4.10. N_c and N_q for soils with $\phi = 35°$ converged to their true solutions (N_c = 46.124 and N_q = 33.294) calculated from the continual deformation mechanism, up to three decimal places for the number of blocks greater than 10^3. It means that continual deformation, Fig. 4.9(c), can be interpreted as a multi-block mechanism, Fig. 4.9(a), with an infinite number of blocks. This observation suggests that the rigid block translation mechanism can approximate the continual Prandtl-type deformation pattern, with the computed factors N_c and N_q showing a numerical tendency toward the values from the continual mechanism.

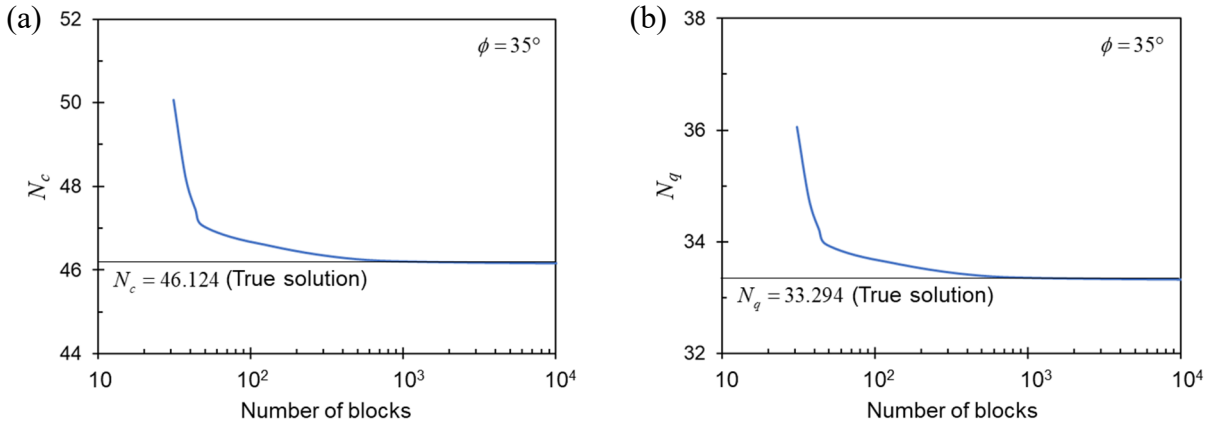


Figure 4.10: Bearing capacity factors computed using different number of blocks for rigid block in a translation mechanism; (a) N_c, and (b) N_q

The technique to utilize limit analysis for non-associative soils can be extended to non-linear yield criteria. The shear strength of soils can be effectively represented by the Mohr-Coulomb yield criterion, which establishes a linear relationship between shear strength and pressure. In contrast, the dependence of rock shear strength on pressure is distinctly nonlinear. Originated in 1980, the Hoek-Brown criterion (Hoek and Brown 1980, Hoek et al. 2002, Hoek and Brown 2019) is a widely accepted strength criterion for rocks, recognized for its ability to reflect the non-linear dependency of rock strength on pressure. This criterion is a function of the major and minor principal stresses, with parameters related to the type and the quality of the rock

$$\sigma_1' = \sigma_3' + \sigma_{ci}\left(m_b \frac{\sigma_3'}{\sigma_{ci}} + s\right)^a \tag{4.22}$$

where σ_{ci} is the uniaxial compressive strength of intact rock. Other material parameters are defined as

$$\begin{aligned} m_b &= m_i e^{\left(\frac{GSI-100}{28-14D}\right)} \\ a &= \frac{1}{2} + \frac{1}{6}\left(e^{-\frac{GSI}{15}} - e^{-\frac{20}{3}}\right) \\ s &= e^{\left(\frac{GSI-100}{9-3D}\right)} \end{aligned} \tag{4.23}$$

where m_i is a rock type-dependent parameter with a typical range of 5–35. *GSI* is the Geological Strength Index, indicating the quality of rock mass, ranging from 5 to 100, with *GSI* = 100 indicating an intact rock. *D* is a disturbance factor with a range of 0 to 1, *D*=0 defining undisturbed rock and *D*=1 defining very substantially disturbed rock. The Hoek-Brown yield criterion in Eq. (4.22) can be presented as a surface in the Haigh-Westergaard space, as shown in Fig. 4.11(a). Surface ABCA represents plastic stress states where $\sigma_1' \geq \sigma_2' \geq \sigma_3'$.

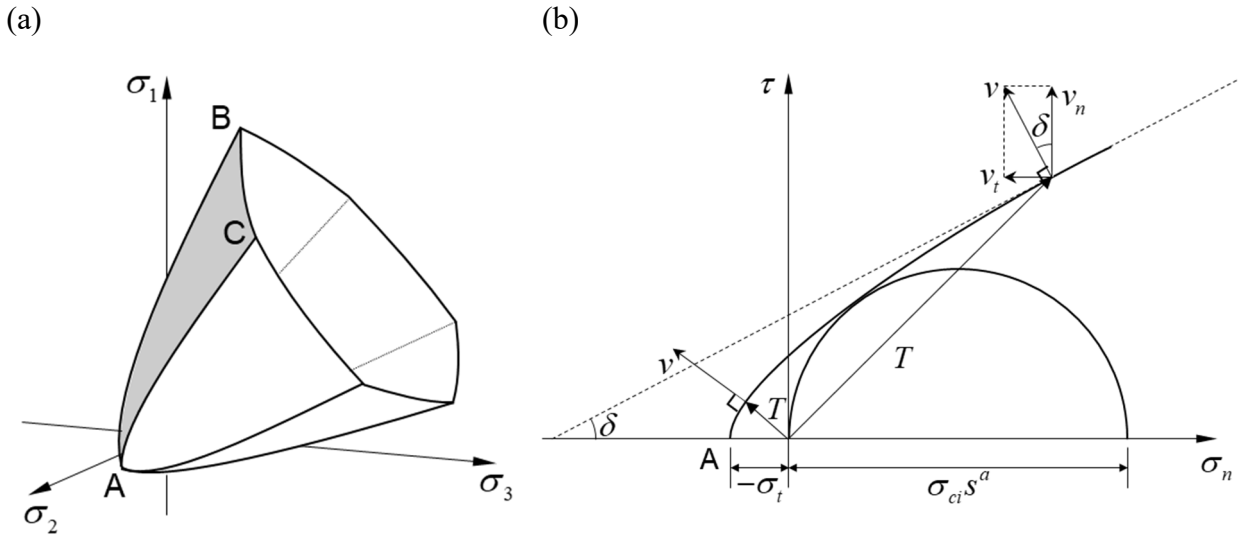


Figure 4.11: Hoek-Brown yield criterion (a) in Haigh-Westergaard space; (b) on $\sigma_n - \tau$ plane with tractions *T* and velocity discontinuity vectors *v* on kinematic discontinuities, conforming to the associative flow rule

While the yield criterion (Eq. 4.22) is presented as a function of effective principal stresses, Kumar (1998) presented this yield criterion as an envelope of limit states on $\sigma_n - \tau$ plane. In doing so, Kumar used some of the early developments by Balmer (1952). Kumar's representation was given in a parametric form as a function of rupture angle δ shown in Fig. 4.11(b). Rupture angle δ can be interpreted as an instantaneous friction angle of the rock. The Hoek-Brown yield criterion in a parametric form reads

$$\sigma_n = \sigma_{ci}\left\{\left(\frac{1}{m_b}+\frac{\sin\delta}{m_b a}\right)\left[\frac{m_b a(1-\sin\delta)}{2\sin\delta}\right]^{\frac{1}{1-a}}-\frac{s}{m_b}\right\}$$
$$\tau = \sigma_{ci}\left\{\frac{\cos\delta}{2}\left[\frac{m_b a(1-\sin\delta)}{2\sin\delta}\right]^{\frac{a}{1-a}}\right\} \tag{4.24}$$

Hoek-Brown yield criterion on a $\sigma_n - \tau$ plane shows a non-linear convex shape, Fig. 4.11(b). The apex of the yield criterion at point A indicates isotropic tensile strength σ_t, which can be defined by substituting $\sigma_1' = \sigma_3' = -\sigma_t$ into Eq. (4.22)

$$\sigma_t = \sigma_{ci}\frac{s}{m_b} \tag{4.25}$$

Hoek and Brown suggested the yield criterion for rock, but they did not specify the flow rule or the plastic potential in the model. If the rock is associative, tanδ is the ratio of the volumetric strain rate to the shear strain rate. However, the dilation of the soil predicted by the pressure-dependent yield criterion and associative flow rule is larger than that obtained from physical testing (see Section 3.1). Hence, the need for the use of non-associative flow rule arises. For non-associative materials, the inclination of the velocity jump along the discontinuity is governed by dilatancy angle ϑ, not rupture angle δ. Hence, a parametric form of *substitution* Hoek-Brown yield criterion with ϑ as one of the parameters is needed to enable computation of the limit load on non-associative rock. Derivation of the parametric form of *substitution* Hoek-Brown yield criterion starts from obtaining traction vectors *T* within the material. Fig. 4.12 shows the Hoek-Brown yield criterion with the stress circle representing the limit (plastic) stress state. This is for coaxial non-associativity, so stress characteristics and velocity characteristics originate from the stress pole of the Mohr circle, point P. Major and minor principal stress directions (σ_1 and σ_3 directions) are presented, and they are identical to the major and minor principal directions of the strain rates.

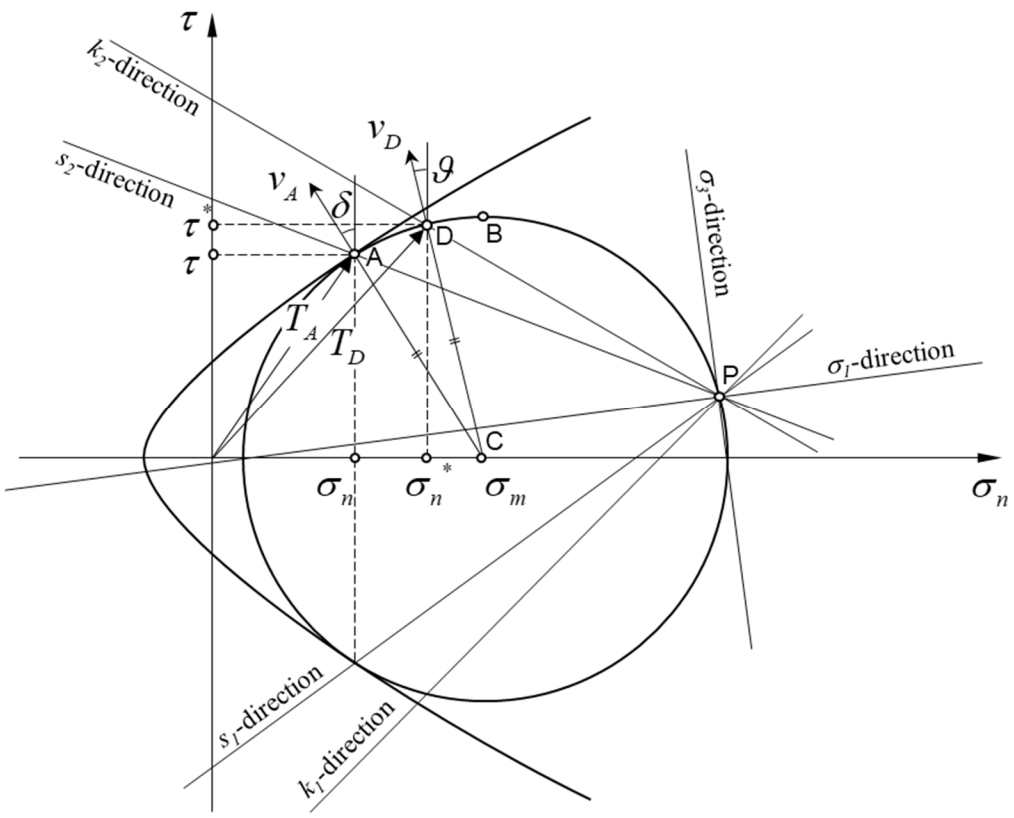


Figure 4.12: Tractions and velocity jumps for Hoek-Brown yield criterion with non-associative flow rule

The associative flow is represented by the velocity vector v_A located at point A ($\vartheta = \delta$). Non-associative flow is represented as v_D located at a point on arc AB ($\vartheta \leq \delta$). For associative flow rule, velocity characteristics coincide with the stress characteristics s_1 and s_2. For non-associative material, the velocity characteristics of k_1 and k_2 families do not coincide with stress characteristics s_1 and s_2.

Traction vector T_A for associative rock is defined by point A (σ_n, τ) in Fig. 4.12 and is captured in Eqs. (4.24), but traction vector T_D for non-associative rock, defined by point D, needs to be derived from the geometric relations in Fig. 4.12. The length of segments CD and CA is equal to the radius of the Mohr circle, which can be defined as $\tau / \cos\delta$. Using geometric relationships in Fig. 4.12, traction vector T defined by point D (σ_n^*, τ^*) can be found as

$$\sigma_n^* = \sigma_m - \tau \frac{\sin \vartheta}{\cos \delta}$$
$$\tau^* = \tau \frac{\cos \vartheta}{\cos \delta} \tag{4.26}$$

where

$$\sigma_m = \sigma_n + \tau \tan \delta \tag{4.27}$$

Substituting Eqs. (4.24) into (4.26), one arrives at the yield criterion of a fictitious substitution material with angles δ and ϑ being its parameters

$$\sigma_n^* = \sigma_{ci} \left\{ \left(\frac{1}{m_b} + \frac{\sin \delta}{m_b a} \right) \left[\frac{m_b a (1 - \sin \delta)}{2 \sin \delta} \right]^{\frac{1}{1-a}} - \frac{s}{m_b} + \frac{\sin \delta - \sin \vartheta}{2} \left[\frac{m_b a (1 - \sin \delta)}{2 \sin \delta} \right]^{\frac{a}{1-a}} \right\}$$
$$\tau^* = \sigma_{ci} \left\{ \frac{\cos \vartheta}{2} \left[\frac{m_b a (1 - \sin \delta)}{2 \sin \delta} \right]^{\frac{a}{1-a}} \right\} \tag{4.28}$$

As a result, the yield criterion for the original material and fictitious substitution material differs. As an example, the yield criterion for rock mass with $m_i = 5,\ D = 0,\ GSI = 65,\ \vartheta = \delta$ is shown in Fig. 4.13 with the yield criterion of a substitution rock mass of $m_i = 5$, $D = 0$, $GSI = 65$, $\vartheta = 0°$ on a $\sigma_n - \tau$ plane, normalized by σ_{ci}. Mohr circles are presented to show how the substitution yield criterion can be graphically formulated. Dilatancy angle of $\vartheta = 0°$ is selected to demonstrate the extreme case of non-associativity. The solution to a boundary value problem for a substitution material must be independent of the choice of the flow rule for rigid-block translation mechanism, as demonstrated in Eq. (4.16). It is convenient to use a normality flow rule, so that the theorem of limit analysis is always true, with velocities indicated in Fig. 4.13 as v_B^* and v_D^*.

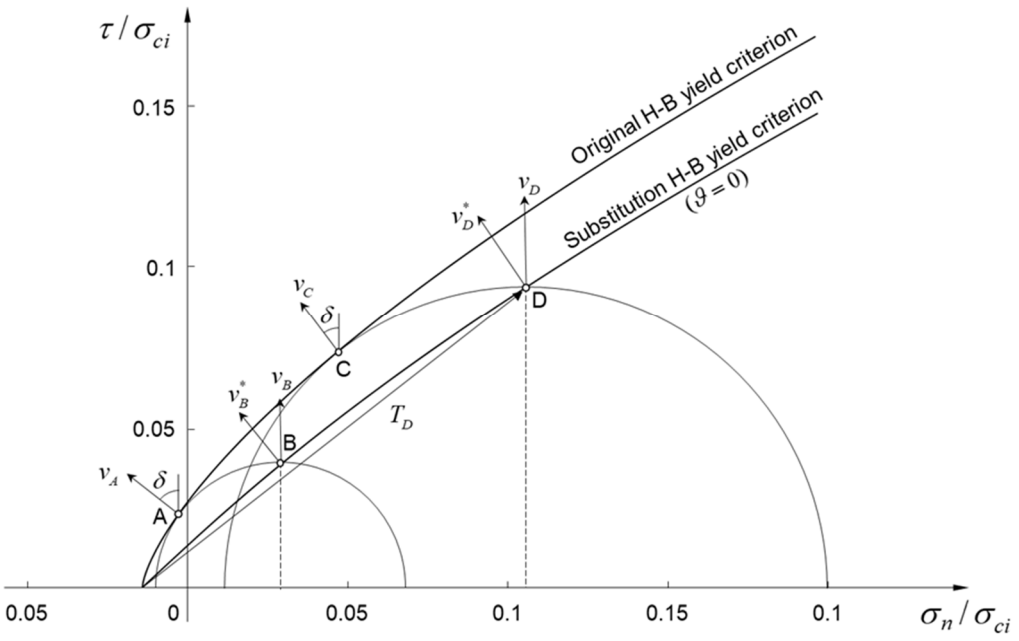


Figure 4.13: Hoek-Brown yield criterion and substitution Hoek-Brown yield criterion for non-associative rock (m_i=5, D=0, GSI=65, ϑ=0°)

This extension demonstrates that the framework originally developed for linear yield criteria can be generalized to non-linear yield criteria such as the Hoek-Brown yield criterion. By introducing a substitution material with equivalent parameters that incorporate the effect of the flow rule, the non-associative behavior of rocks can be taken into account within the same kinematic limit analysis formulation used for associative materials. The concept of substitution material establishes a basis for evaluating the impact of non-associativity on the stability of geotechnical structures.

Chapter 5 Impact of Non-associativity on Stability of Geotechnical Structures

The preceding chapters have established the theoretical background for plastic behavior of geomaterials, the formulation of limit analysis theorems, and the methodological extension that enables the application of limit analysis to non-associative materials. In practical geotechnical design, associative flow rule is often adopted, yet laboratory observations show that soils rarely satisfy this condition. Hence, the stability of geotechnical structures such as slopes and foundation and loads on retaining walls can be significantly affected by the degree of non-associativity in the soil's plastic flow rule.

5.1 Slopes

The slope stability problem is one of the classical and most important topics in geotechnical engineering. Methods for evaluating slope stability can be broadly classified into three categories: (i) limit equilibrium methods (Bishop 1995, Janbu 1957, and Morgenstern and Price 1965), (ii) limit analysis methods (Drucker and Prager 1952, Chen 1975, Michalowski 1989, 1995), and (iii) numerical methods (Griffiths and Marquez 2007). The limit equilibrium method simplifies the slope mass into slices and enforces equilibrium between the driving and resisting forces or moments. While computationally efficient, this approach requires assumptions regarding interslice forces and the shape of the failure surface. The limit analysis method provides rigorous bounds on the collapse load or the factor of safety. The numerical methods, such as finite element or finite difference methods, can capture complex geometries, and they also allow direct computation of displacement.

To combine the advantages of the numerical formulation and the rigor of limit analysis, the Finite Element Limit Analysis (FELA) method was developed. FELA directly implements the theorems of limit analysis within the finite element framework without prescribing a kinematically admissible failure mechanism. In this study, slope stability analyses are conducted

using FELA. For associative soils, the analyses are performed using the conventional strength parameters, c and ϕ. As discussed in Section 4.3, for non-associative soils, the effect of dilation ϑ is incorporated by adopting substitution material strength parameters c^* and ϕ^*. They are derived based on the following relation

$$\tan\phi^* = \frac{\cos\vartheta\cos\phi}{1-\sin\vartheta\sin\phi}\tan\phi$$
$$c^* = \frac{\cos\vartheta\cos\phi}{1-\sin\vartheta\sin\phi}c \tag{5.1}$$

Both two-dimensional (plane strain) and three-dimensional slope configurations are analyzed to examine how the influence of non-associativity varies.

5.1.1 Plane strain analysis

In practical geotechnical engineering, slope stability is often evaluated using 2D plane strain analyses. This approach is based on a representative cross-section of the slope, typically selected according to the geometry and the relative importance of each section. Engineers commonly analyze multiple cross-sections in practice, prioritizing those with critical geometry, stratigraphy, or loading conditions. The assumption of plane strain is reasonable when the slope extends sufficiently in the out-of-plane direction, such that strain variation along the longitudinal axis is negligible. In this study, slope stability analyses were performed using Finite Element Limit Analysis (FELA) implemented in OptumG2, a commercial software developed based on second-order cone programming (SOCP). The FELA framework combines the rigor of limit analysis with the numerical robustness of finite element discretization, enabling lower-bound and upper-bound formulations to be solved as large-scale optimization problems.

The computational model domain is discretized using triangular finite elements with adaptive meshing to ensure refinement in regions of high shear strain rates near the expected failure surface. Fig. 5.1(a) shows that the bottom boundary is fixed in both horizontal and vertical directions, while the lateral boundaries are fixed horizontally but allowed vertical displacement. The slope surface is modeled as a stress-free boundary. The soil is modeled using

the Mohr-Coulomb yield criterion, characterized by cohesion c, internal friction angle ϕ, and unit weight γ. The non-associative flow rule is implemented by adopting the substitution material strength parameters, c^* and ϕ^* by using Eq. (5.1).

The results of FELA for the slope model are presented in terms of factor of safety F. The factor of safety is the ratio of the available shear strength of the soil to the minimum shear stress required to maintain limit equilibrium

$$F = \frac{c}{c_d} = \frac{\tan\phi}{\tan\phi_d} \tag{5.2}$$

where c_d and ϕ_d are soil strength parameters corresponding to the minimum values required for the structure to remain in limit equilibrium. Parameters c_d and ϕ_d do not reflect the true strength of the soil but rather the minimum values necessary to maintain overall equilibrium under given loading conditions. The factor of safety defined in Eq. (5.2), therefore, represents a global measure of stability. Parameters c_d and ϕ_d are fictitious and not true material properties; the resulting failure pattern should not be interpreted as a physically exact representation of the collapse mechanism.

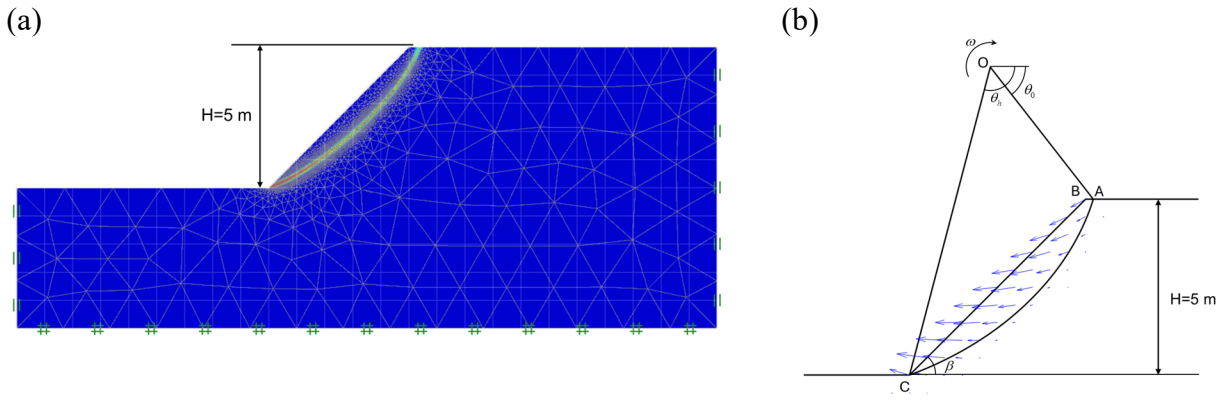


Figure 5.1: Comparison of mechanisms for slope stability: (a) strain rate field from FELA (red/blue – max/min), and (b) contours of optimized collapse mechanism from classical limit analysis with superimposed velocities from FELA

The slope model analyzed in Optum G2 has a height of 5 m and an inclination of 45°, with soil characterized by a friction angle of 35° and a cohesion of 50 kPa. The distribution of plastic

shear strain rates obtained from the Optum G2 simulation is presented in Fig. 5.1(a), where red denotes the maximum shear strain rates and dark blue corresponds to zero shear strain rate. The color contours highlight a distinct collapse mechanism in the velocity field. Note that the absolute values of shear strain rates are meaningful only in relation to the rate of loads, and they are not indicated here. The corresponding mechanism obtained from the analytical solution is presented in Fig. 5.1(b) with relative velocities from the Optum G2 simulation superimposed. The obtained collapse mechanism by analytical solution, Fig. 5.1(b), corresponds to a rotational mechanism. The soil mass above the velocity discontinuity undergoes rigid-body rotation about point O. Unlike the analytical approach, where a specific mechanism must be prescribed a priori, the FELA does not assume any predefined failure pattern; instead, the mechanism naturally emerges from the finite element solution that satisfies the limit conditions. Hence, the velocity discontinuity separating the moving soil mass from the stationary soil forms a sharp boundary in the analytical solution, Fig. 5.1(b), whereas the discontinuity appears to be a diffused shear band in FELA, Fig. 5.1(a). The analytical model yields the factor of safety F = 4.45, whereas the Optum G2 solution was found to be F = 4.42 with 100k elements, showing a difference of less than 1%.

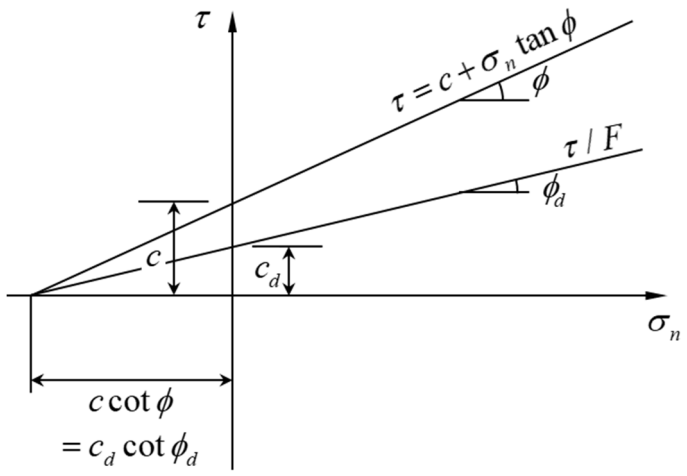


Figure 5.2: Independence of parameter $c \cot\phi$ of the safety factor

The factor of safety is often expressed in the form of charts. Many classical charts, such as those by Taylor (1937), require an iterative procedure. In Taylor-type stability charts, the required cohesion to maintain equilibrium is expressed in normalized form $c_d / (\gamma H) = c / (\gamma HF)$, and factor

of safety F is obtained according to Eq. (5.2). To avoid the iteration requirement, the factor of safety is plotted as a function of $c\cot\phi$. In this form, product $c\cot\phi$ remains constant, as shown in Fig. 5.2, regardless of the safety factor and it eliminates the need for repeated iterations. Consequently, it is useful to plot $c/(\gamma H\tan\phi)$ versus $F/\tan\phi$, and produce charts for various slope inclination angles. The advantage of this representation is that F can be estimated directly from charts without iterative computation.

Figure 5.3 presents the stability of uniform slopes in terms of $F/\tan\phi$ and $c/(\gamma H\tan\phi)$ for different slope angles β. The comparison between the FELA results and the classical rotational mechanism shows excellent agreement with less than 1%, demonstrating the consistency between numerical and analytical approaches. Fig. 5.3(a) and (b) present identical datasets of normalized slope stability results, but over different ranges of $c/(\gamma H\tan\phi)$ to emphasize variations in normalized slope geometry and soil strength conditions.

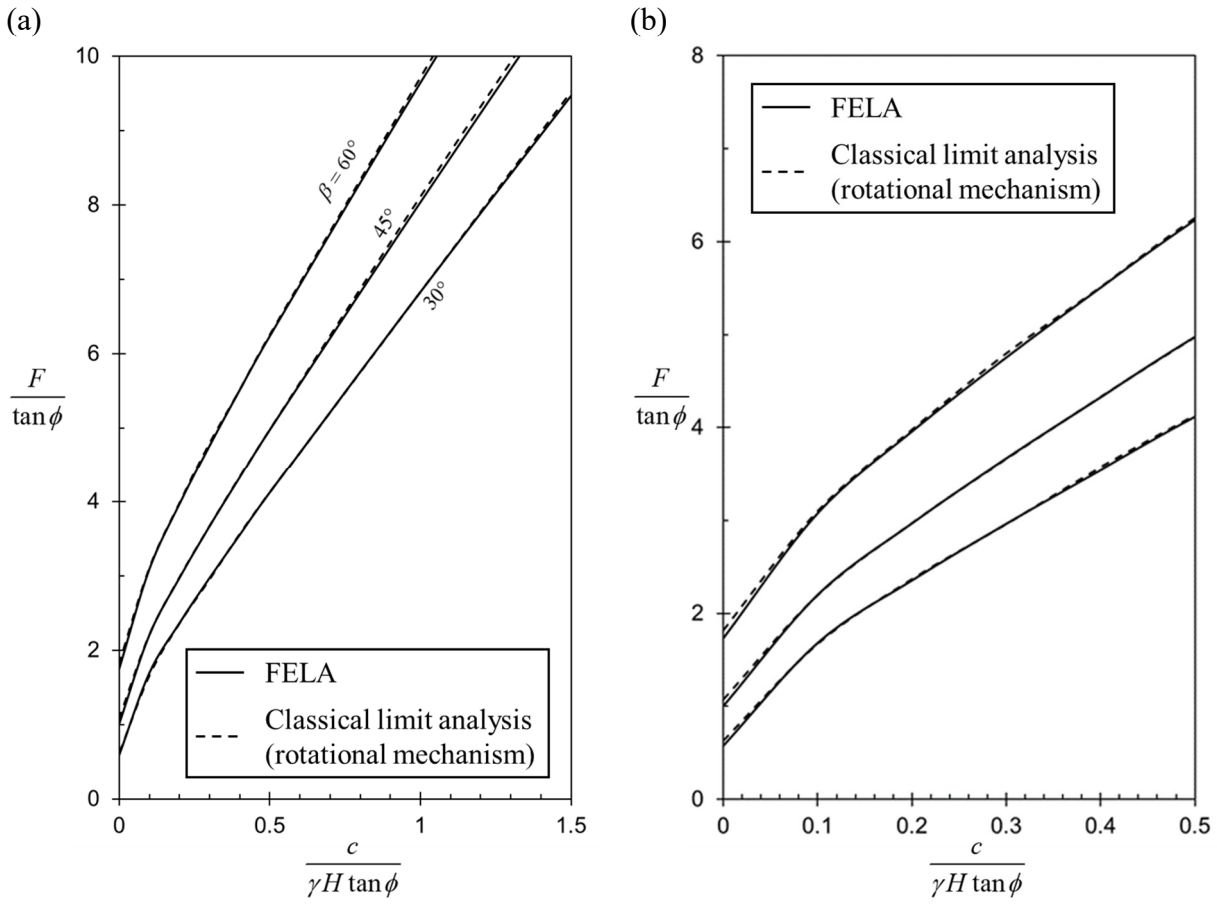


Figure 5.3: Stability chart for uniform slopes (2D plane strain analysis) obtained from FELA and classical limit analysis method

5.1.2 Spatial collapse in slopes

The failure of natural and engineered slopes is typically a three-dimensional (3D) phenomenon, governed by the combined effects of soil strength, geometry, and boundary constraints. Plane-strain analyses are commonly adopted in stability evaluations for practical purposes. However, they idealize the problem and do not capture the spatial nature of the collapse mechanism, especially when slope width B is limited by natural topography or structural boundaries (Michalowski and Drescher 2009; Michalowski and Park 2021). Fig. 5.4 shows a schematic of the 3D failure mechanism of a uniform slope that has a width-height ratio of B/H and an inclination of β. 3D slope failures are commonly characterized by a rotational mechanism that develops along a curvilinear conical surface, often referred to as a horn-type failure surface. The soil mass above

this surface undergoes rotation about an axis parallel to the slope crest (line RR′), producing a spoon-shaped sliding volume bounded by the intersection of the curved failure surface and the original ground surface.

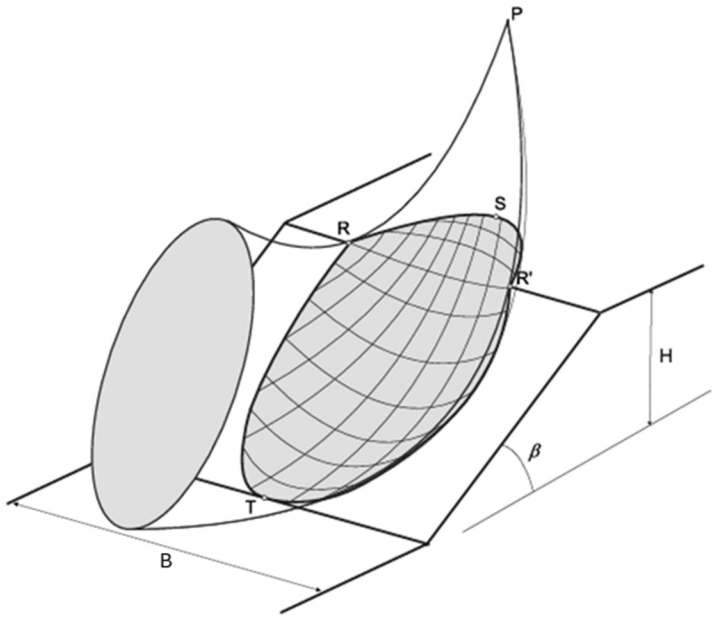


Figure 5.4: Three-dimensional mechanism generated by the rotation of a circle with a variable diameter (after Michalowski 2010)

Although the rotational mechanism provides a useful conceptual reference for understanding 3D collapse mechanism of slope, it requires an idealized kinematic mechanism prescribed a priori. In contrast, FELA framework does not impose any predefined failure mechanism. The collapse state emerges naturally from the optimization process that minimizes the load multiplier while enforcing yield and equilibrium constraints. The resulting plastic strain rate field (or velocity field) reveals the most critical admissible state, allowing direct visualization of the spatial extent.

To avoid constraining the natural formation of the failure mechanism, only essential boundary conditions were applied in FELA, as shown in Fig. 5.5. The bottom surface of the model was fixed in all directions. The vertical planes on the two sides of the slope were restrained in all directions. The front and back boundaries were restrained in the normal direction with respect to

their planes, while free in the tangential directions. The ground surface including the slope face was left entirely free of tractions.

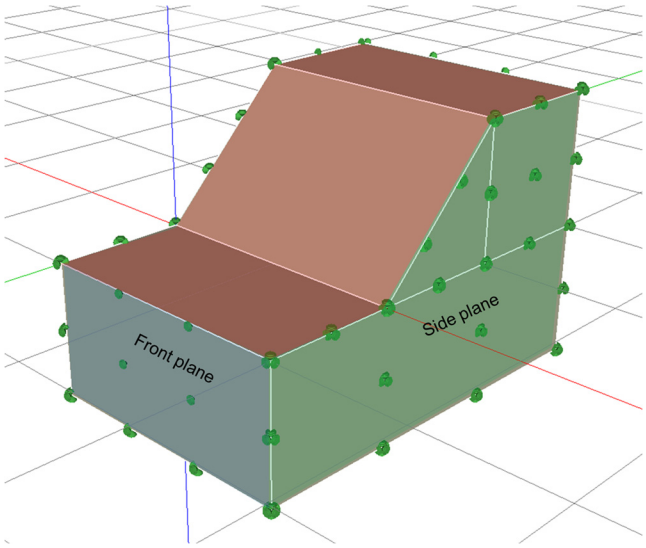


Figure 5.5. Boundary conditions of a slope in 3D FELA

As illustrations of the FELA results obtained from Optum G3, Fig. 5.6 presents the computed failure mechanism for the case of $\phi = 30°$ and $40°$, $\beta = 45°$, $\frac{B}{H} = 2$, and $\frac{c}{\gamma H} = 0.5$ using 10k elements. Symmetry allows the model to be represented by only half of the slope geometry. The contours represent the magnitudes of velocities at failure, highlighting the location and shape of the critical slip surface. Warmer colors (red) indicate zones of larger velocity magnitude, while cooler colors (blue) represent regions of lower velocity. In the context of limit analysis, the velocity field is expressed in relative terms. Thus, only the distribution and relative magnitude of velocities are physically meaningful, rather than their absolute values. The observed pattern of the velocity field is consistent with a rotational mechanism for this configuration, although a similar velocity distribution can be obtained from translational or mixed mechanisms.

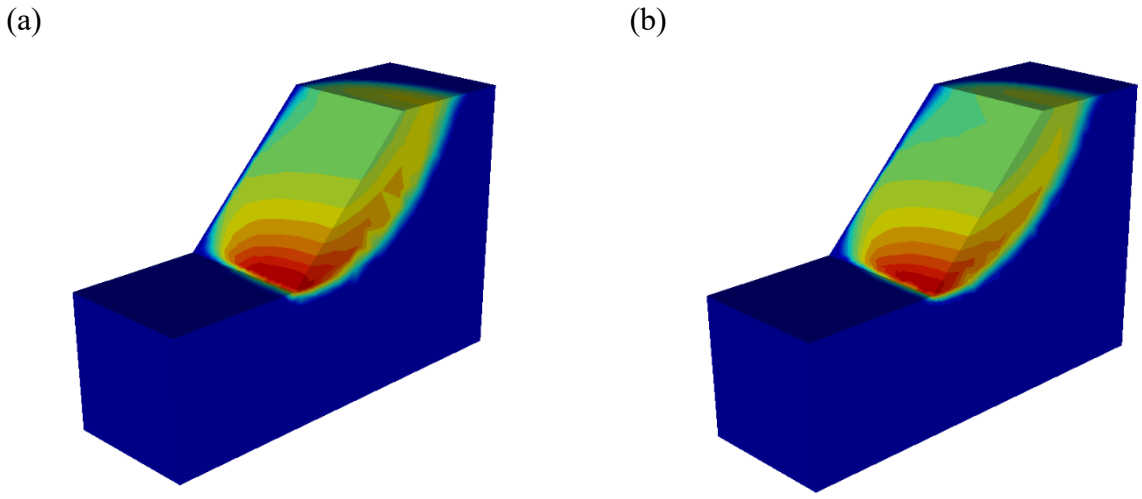


Figure 5.6: Contours of velocity magnitudes from 3D FELA, uniform slopes of β=45°, B/H=2, and $c/(\gamma H)$=0.5: (a) ϕ=30° and (b) ϕ=40°

Three-dimensional stability of slopes was evaluated using FELA implemented in Optum G3. The computed results are presented in Fig. 5.7 in the same normalized form as Fig. 5.3, using $F / \tan\phi$ versus $c / (\gamma H \tan\phi)$. Factor of safety F was obtained for each slope geometry, characterized by the width ratio B/H and slope inclination β. This representation eliminates the need for iterative procedures when the factor of safety is sought, allowing the results for different slope configurations to be presented compactly in the form of stability charts. Fig. 5.7(a-f) summarize the results as stability charts. Three slope inclinations are considered, $\beta = 30°$, 45°, and 60°; for each β, the charts include curves for width ratios, $B / H = 1$, 2, 5, and $B / H \to \infty$. The case $B / H \to \infty$ coincides with plane-strain and is therefore taken directly from the 2D results in Fig. 5.3. Within each β, two panels are shown in the same normalized coordinates: the left panel displays the full range $0 \le c / (\gamma H \tan\phi) \le 1.5$, while the right panel provides a zoomed view for $0 \le c / (\gamma H \tan\phi) \le 0.5$ to resolve trends at low normalized cohesion.

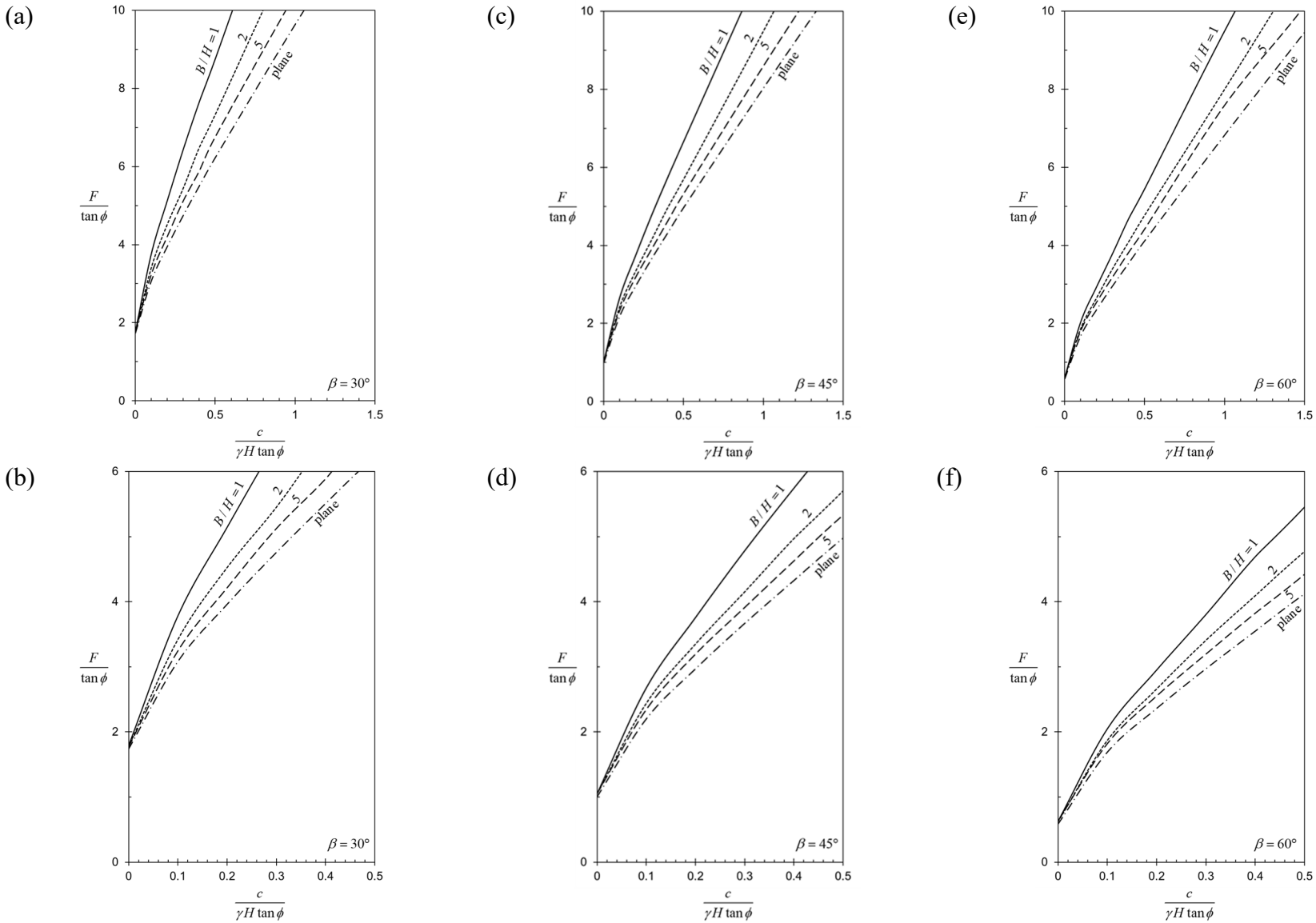


Figure 5.7: Stability chart for uniform slopes (3D analysis) obtained by FELA

5.1.3 Impact of non-associativity on stability of slopes

The influence of non-associative flow on slope stability is examined using the normalized representation, $F / \tan\phi$ and $c / (\gamma H \tan\phi)$. Before proceeding, it is recalled that c^* and ϕ^* are the shear strength parameters of the substitution material, which serve as equivalent strength parameters used to represent the behavior of non-associative soils. Both c^* and ϕ^* are functions of c, ϕ, and dilation angle ϑ, as shown in Eq. 5.1. Since the same functional relationship transforms c and $\tan\phi$ into c^* and $\tan\phi^*$, $c / (\gamma H \tan\phi)$ can also be expressed as $c^* / (\gamma H \tan\phi^*)$. For a uniform slope of a certain geometry (defined by B/H and β), the horizontal axis in Fig. 5.7 is identical for both associative and non-associative materials. The ordinate read from the normalized chart, Fig. 5.7, is also the same; however, the actual factor of safety differs because it is obtained by multiplying the ordinate value by $\tan\phi$ for the associative soil and by $\tan\phi^*$ for the non-associative soil. The reduction in the factor of safety due to non-associativity can therefore be quantified as

$$\lambda_F = \frac{\left|F - F^*\right|}{F} \cdot 100 = \frac{\left|\tan\phi - \tan\phi^*\right|}{\tan\phi} \cdot 100(\%) \tag{5.3}$$

where λ_F is the non-associativity impact factor for factor of safety of slopes, F is the factor of safety for associative soil, and F^* is the factor of safety for non-associative soil. This relation provides a direct measure of the effect of non-associative flow on slope stability without recalculating the failure mechanism. Despite the variations in slope inclination, width-height ratio, or dimensionality (2D or 3D), the influence of non-associativity on stability of slopes by a single parameter λ_F, that depends solely on friction and dilation angles. This invariance arises because both the associative and non-associative results share identical normalized coordinates. The computed values of λ_F for several combinations of friction and dilation angles are summarized in Table. 5.1. The table presents the relative reduction in the factor of safety for representative soil conditions corresponding to typical internal friction angles of 20°, 30°, and 40°. The dilation angle

was assumed to vary in proportion to the friction angle, considering the case of $\vartheta = \frac{2}{3}\phi$ and $\vartheta = \frac{1}{3}\phi$, as well as the extreme incompressible case of $\vartheta = 20°$.

Table 5.1: Non-associativity impact factor λ_F for factor of safety of slopes calculated for different internal friction and dilation angles

λ_F								
$\phi = 20°$			$\phi = 30°$			$\phi = 40°$		
$\vartheta=\frac{2}{3}\phi$	$\vartheta=\frac{1}{3}\phi$	$\vartheta=0°$	$\vartheta=\frac{2}{3}\phi$	$\vartheta=\frac{1}{3}\phi$	$\vartheta=0°$	$\vartheta=\frac{2}{3}\phi$	$\vartheta=\frac{1}{3}\phi$	$\vartheta=0°$
0.73%	2.81%	6.03%	1.83%	6.60%	13.40%	3.79%	12.49%	23.40%

The results, Table. 5.1, show that the influence of non-associativity becomes increasingly pronounced as the dilation angle decreases. As discussed in Section 2.1, soils do not generally follow the associative flow rule, and the dilation angle is often smaller than the friction angle. For non-associative soils with relatively low friction angles, the assumption of the associative flow rule introduces only a minor error; however, for materials with high friction angles, the impact of non-associativity becomes increasingly pronounced. In particular, for the extreme case of $\phi = 40°$ and $\vartheta = 0°$, the factor of safety is 23.40% lower than that of the associative soil, demonstrating that the neglect of non-associativity can yield non-conservative predictions of slope stability.

5.2 Loads on retaining structures

Retaining walls are essential structures in geotechnical engineering, designed to resist lateral pressures from soil masses or other materials. They are widely used in various applications, from supporting excavations to stabilizing slopes and embankments. The stability and overall design of retaining walls depend on an accurate characterization of the lateral earth pressures acting on the wall, which govern required wall dimensions and reinforcement (e.g., geogrids or geotextiles) to prevent failure modes such as overturning, sliding, or bearing capacity failure. Classical plasticity theory often assumes that soil follows the associative plastic flow rule, and the associative flow rule is commonly used to estimate these loads. Coulomb's wedge theory (Coulomb 1776),

although not explicitly developed from the perspective of the flow rule, is equivalent to an associative solution when interpreted from the limit analysis standpoint.

As discussed in Section 4.1, laboratory evidence indicates that soils generally exhibit non-associative plastic behavior. Hence, earth pressures can differ significantly from those predicted by classical associative solutions. Therefore, the effect of non-associativity may introduce a substantial deviation in the predicted active and passive loads. To evaluate the impact of non-associativity on retaining wall loads, substitution material that accounts for non-associativity is introduced. Strength parameters of the substitution material, c^* and ϕ^*, are calculated according to Eq. (5.4), and they were derived in Section 4.3.

5.2.1 Active load

Coulomb's wedge theory (Coulomb 1776) introduced the idea of a failure wedge to obtain the earth force on the wall, defining the shape and mechanics of the soil mass likely to move when a retaining wall fails. Coulomb used the limit equilibrium method to obtain the earth force on the wall, but the same results can be obtained by implementing the idea of a wedge into upper-bound limit analysis.

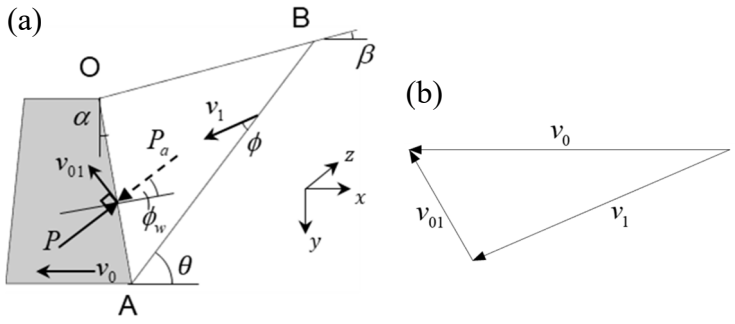


Figure 5.8: (a) Coulomb-type mechanism for lateral active earth pressure, and (b) hodograph

Figure 5.8 shows the Coulomb-type collapse mechanism and its hodograph for an active case. Backfill soil is inclined by counter-clockwise angle β to the x-axis, and the wall is inclined by clockwise angle α to the y-axis. The soil internal friction angle is ϕ and the soil-wall interface friction angle is ϕ_w. Active earth thrust P_a is inclined at counter-clockwise angle of ϕ_w to the line

normal to the wall, because the soil wedge behind the wall is subjected to sliding. P_a is an active force acting on the wall, while P is its reaction. Subscript a is used to indicate that earth thrust P_a is an active force. Wall velocity v_0 is horizontal to the left, and velocity jump at the soil-wall interface v_{01} is inclined by counter-clockwise angle ϕ_w to the wall. The velocity of the soil region OAB, v_1, is inclined at counter-clockwise angle ϕ to the kinematic discontinuity AB. Mechanism for the active case in Fig. 5.8(a) can be fully defined by an independent variable θ, inclination angle of the failure wedge. The independent variable is optimized to obtain the maximum of the lower bound to the true limit load.

In the computation of kinematic limit analysis using the Coulomb-type mechanism, work dissipation in the soil is nil, because the backfill soil doesn't have cohesion. Dissipation along the soil-wall interface is also taken as zero under the admissible assumption that velocity vector v_{01} is normal to load vector P_a. This does not imply that separation between the wall and the backfill necessarily occurs in reality; rather, this kinematically admissible assumption eliminates the interface dissipation term. Hence, the left side of inequality (4.12) becomes zero, resulting in

$$\int_S T_i v_i^k \, dS + \gamma \int_V n_i v_i^k \, dV \leq 0 \tag{5.4}$$

where T_i is the unknown traction vector on the left side of the wall (line OA), n_i is the unit vector in the direction of gravity. Because the velocity field corresponds to a rigid body translation, v_i^k is constant along the wall, and the surface integral of traction, $\int_S T_i \, dS$, represents the reaction of the wall, equal in magnitude to the load acting on the retaining wall. The obtained load from inequality (5.4) produces the lower-bound limit load on the wall for the active case. More refined mechanisms, Fig. 5.9 have been suggested to obtain more accurate estimates of loads on retaining walls (Chen and Rosenfarb 1973). In this same spirit, a more general multi-block mechanism can be constructed, allowing piece-wise linear discontinuities and greater geometric flexibility than other mechanisms. This will be pursued in the next section.

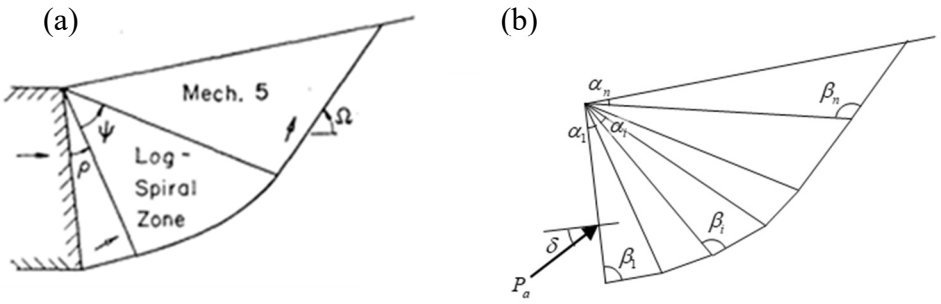


Figure 5.9: (a) Sandwich mechanism, and (b) multi-wedge mechanism for retaining wall passive load (from Chen and Rosenfarb 1973)

Multi-block mechanism

The multi-block mechanism is shown in Fig. 5.10. This mechanism assumes purely translational kinematics. The mechanism consists of multiple quadrangle and triangular blocks. The hodograph in Fig. 5.10(b) shows the velocities of each block and the velocity discontinuity vectors at their interfaces. Since the failure surface for the active retaining wall case is nearly straight in this configuration, the flexibility offered by the multi-block mechanism cannot be effectively utilized. In the configuration shown in Fig. 5.10(a), the soil regions labeled a, b, c, d, and e effectively behave as rigid blocks as shown in Fig. 5.10(b). Backfill soil is inclined by counter-clockwise angle β to the x-axis, and the wall is inclined by clockwise angle α to the y-axis. Active earth thrust P_a is inclined at counter-clockwise angle of ϕ_w to the line normal to the wall, because the soil block behind the wall is subjected to sliding. Velocity jumps at interfaces of blocks are inclined at angle of ϕ to the interfaces of each block (kinematic discontinuities). Geometry of the mechanism is defined by inclination of each straight-line segment of a velocity discontinuity. Angles of inclinations are the independent variables of the mechanism and they are constrained by kinematic admissibility of the mechanism. The number of blocks is m and the number of blocks bordering block a, Fig. 5.10(a), is a, then the total number of independent variables can be found from formula $2(m-1)+a$. All independent variables are optimized to obtain the maximum estimate of limit load P.

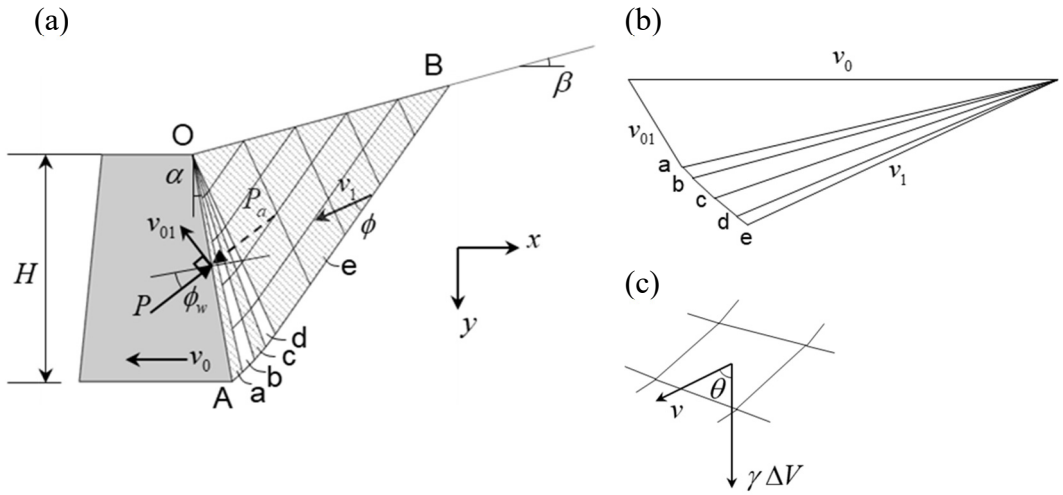


Figure 5.10: (a) Multi-block mechanism for active earth pressure, (b) hodograph, and (c) example volume element used for calculating the work rate of soil weight

By conforming to the labeling convention of blocks in Fig. 5.10, inequality (5.4) can be rewritten as

$$P \geq \frac{\gamma V_a v_a \cos\theta_a + \gamma V_b v_b \cos\theta_b + \cdots + \gamma V_e v_e \cos\theta_e}{v_0 \cos(\alpha + \phi_w)} \tag{5.5}$$

where P is the true limit load, θ is angle of velocity vector of the corresponding element measured clockwise from the y-axis. Maximum of the lower bound to lateral earth force P can be obtained by inequality (5.5) after optimizing independent variables. The limit load is presented in a form of a commonly used dimensionless measure of load intensity, the active earth pressure coefficient. Active earth pressure coefficient K_a expresses the dimensionless coefficient dependent on soil strength. K_a is obtained by dividing calculated lateral force P by $\gamma H^2/2$. Table 5.2 shows calculated results of coefficient K_a. They have been carried out for internal friction angle ϕ in the range of 30° – 40°. The Coulomb-type and multi-block mechanisms yield the same values over this range.

Table 5.2: Active earth pressure coefficient K_a for different internal friction angle ϕ and soil-wall interface friction angle ϕ_w

ϕ (°)	α (°)	β (°)	$\phi_w = 0°$		$\phi_w = 1/3\phi$		$\phi_w = 2/3\phi$	
			Coulomb	Multi-block*	Coulomb	Multi-block*	Coulomb	Multi-block*
30	0	0	0.333	0.333	0.308	0.308	0.297	0.297
35	0	0	0.271	0.271	0.251	0.251	0.244	0.244
40	0	0	0.217	0.217	0.202	0.202	0.200	0.200

*Number of blocks: 471, Number of independent variables: 960

5.2.2 Passive load

In contrast to the active condition, the passive case involves wall moving toward the backfill, forcing the soil mass to mobilize substantially larger volume of the soil. As a result, a more extensive collapse mechanism develops, and the geometry of the mobilized region becomes more sensitive to different mechanism's geometry when compared to the active case. In the following, the classical associative passive earth pressure mechanism is first reviewed, and then the multi-block mechanism and the effect of non-associativity are examined.

Figure 5.11 shows the Coulomb-type collapse mechanism and its hodograph for a passive case. The wall is inclined by clockwise angle α to the y-axis, and the backfill soil is inclined by counter-clockwise angle β to the x-axis. The soil internal friction angle is ϕ while the soil-wall interface friction angle is ϕ_w. Passive earth thrust P_p is inclined by clockwise angle ϕ_w to the line normal to the wall, because the soil block behind the wall is subjected to sliding. P is an active force acting on the wall, while P_p is its reaction (soil resistance). Since the wall is pushing the backfill in passive case, wall velocity v_0 is horizontal to the right. Velocity jump at the soil-wall interface v_{01} is inclined by counter-clockwise angle of ϕ_w to the wall under the admissible assumption, which is in opposite direction in the active case. The velocity of the soil region OAB, v_1, is inclined at angle ϕ to kinematic discontinuity AB. Mechanism for the passive case in Fig. 5.11(a) is fully defined by independent variable θ, inclination angle of the failure wedge. The independent variable is optimized to obtain the best estimate of the upper-bound to the true limit load.

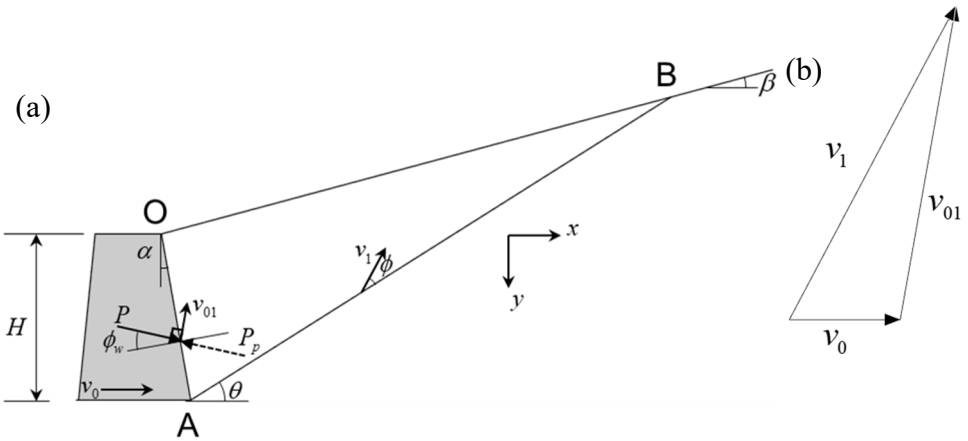


Figure 5.11: (a) Coulomb-type mechanism for lateral active earth pressure, and (b) hodograph

In the computation of the limit load using the kinematic limit analysis with Coulomb-type mechanism, work dissipation in the soil is nil, because the backfill soil is typically considered cohesionless. Work dissipation on the soil-wall interface is also nil because the load vector P_p is normal to the velocity vector v_{01}. Hence, the left side of inequality (4.12) becomes zero, resulting in same as (5.5)

$$\int_S T_i v_i^k \, dS + \gamma \int_V n_i v_i^k \, dV \leq 0 \tag{5.6}$$

where T_i is the unknown traction vector on the left side of the wall (line OA), n_i is the unit vector in the direction of gravity.

Multi-block mechanism

The multi-block mechanism is shown in Fig. 5.12. Backfill soil is inclined by counter-clockwise angle β to the x-axis, and the wall is inclined by clockwise angle α to the y-axis. The soil internal friction angle is ϕ and the soil-wall interface friction angle is ϕ_w. The mechanism consists of multiple quadrangle and triangular blocks originating from point O. The hodograph in Fig. 5.12(b) shows the velocities of each block and the velocity discontinuity vectors at their interfaces. Velocity jumps at interfaces of blocks are inclined at the angle of internal friction to the interfaces in each block (kinematic discontinuities). Geometry of the mechanism is defined by inclination of each straight-line segment of a velocity discontinuity. Angles of inclination are the independent variables of the mechanism and they are constrained by kinematic admissibility of the mechanism. The number of independent blocks is m and the number of blocks bordering block OACO along piece-wise linear kinematic discontinuity OC is a, then the total number of independent variables can be found from formula $2(m - 1) + a$. All independent variables are optimized to obtain the best estimate of the upper-bound to the true limit load.

By conforming to the labeling convention of blocks in Fig. 5.12, inequality (5.6) can be rewritten as

$$P \le \frac{\gamma V_a v_a \sin\theta_a + \gamma V_{b_1} v_{b_1} \sin\theta_{b_1} + \gamma V_{b_2} v_{b_2} \sin\theta_{b_2} + \cdots + \gamma V_{i_5} v_{i_5} \sin\theta_{i_5}}{v_0 \cos(\alpha - \phi_w)} \tag{5.7}$$

where P is the true limit load, θ is the counter-clockwise angle of velocity vector of the corresponding element, with respect to x-axis. The least estimate of lateral earth force P can be obtained by inequality (5.7) after optimizing independent variables.

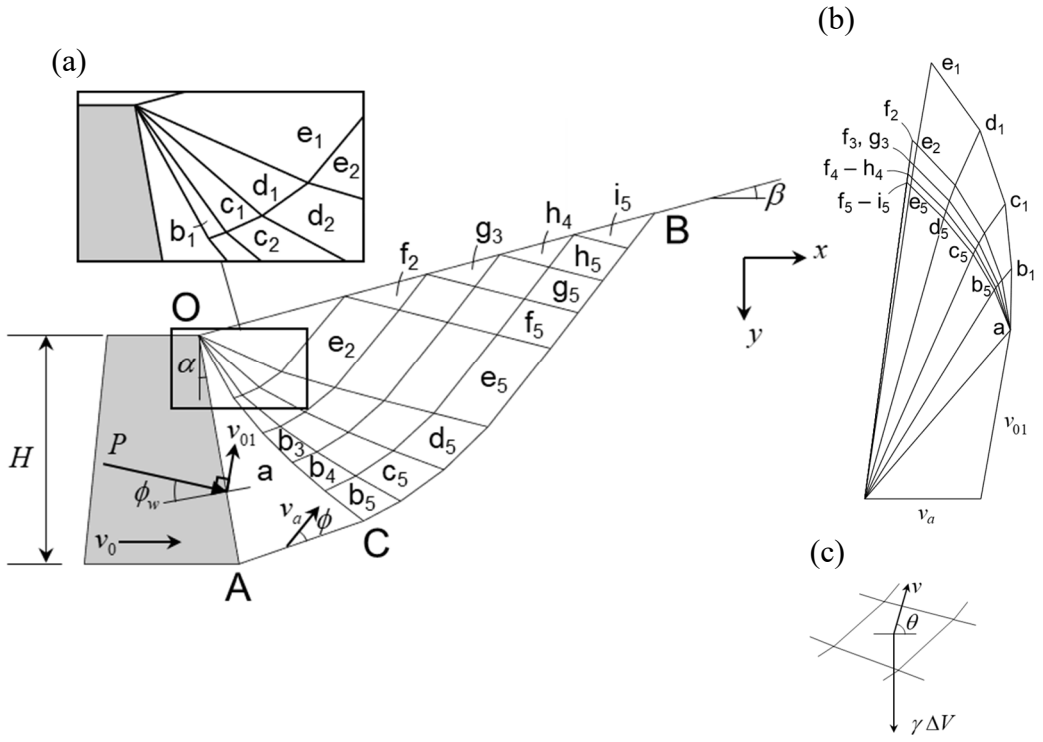


Figure 5.12: (a) Multi-block mechanism for passive earth pressure, (b) hodograph, and (c) example volume element used for calculating the work rate of soil weight

Similar to the active earth pressure coefficient, the passive earth pressure coefficient represents a dimensionless measure of load intensity of passive earth force. Passive earth pressure coefficient K_p is obtained by dividing the lateral earth force by $\gamma H^2/2$. Table 5.3 shows calculation results of coefficient K_p. They have been carried out for internal friction angle ϕ in the range of 30° – 40°, wall inclination angle α up to 20°, backfill inclination angle β up to 20°, and soil-wall interface friction ratio of $\phi_w/\phi = 0$, 1/3, and 2/3. While the multi-block mechanism generally provides more accurate coefficient K_p than the classical Coulomb's analysis, the two methods give

identical results for a limited set of geometric and interface conditions. Identical results are obtained when (i) the wall is vertical ($\alpha = 0°$), the backfill is horizontal ($\beta = 0°$), and the wall-soil interface friction is either zero or $\phi_w = 1/3\phi$; and (ii) when $\alpha = 10°$ & $\beta = 0°$, $\alpha = 20°$ & $\beta = 10°$, and $\phi_w = 0°$.

The difference of results between Coulomb's analysis and multi-block mechanism increases when internal friction angle ϕ is larger, wall inclination angle α is smaller (the wall is closer to vertical), backfill inclination angle β is larger (steeper backfill slope), and soil-wall interface friction angle ϕ_w is larger. The difference in the calculated coefficient K_p between the Coulomb method and the multi-block mechanism becomes more significant under certain conditions. For example, for $\phi = 40°$, $\alpha = 0°$, $\beta = 20°$, and $\phi_w = 2/3\phi$, Coulomb's analysis predicts an extremely large coefficient, $K_p = 908.687$, whereas the multi-block mechanism yields a much smaller value, $K_p = 29.978$. Coulomb's prediction exceeded the multi-block mechanism result by 2929%. A similar pattern appears for $\phi = 40°$, $\alpha = 10°$, $\beta = 20°$, and $\phi_w = 2/3\phi$, result by Coulomb's analysis is $K_p = 66.270$, while that by the multi-block mechanism is $K_p = 21.333$, resulting in a deviation of 211%. Such magnitudes clearly indicate conditions where Coulomb's solution becomes pathologically large, while the multi-block mechanism continues to provide a bounded and physically meaningful estimate.

Table 5.3: Passive earth pressure coefficient K_p for different internal friction angle ϕ, wall angle α, backfill inclination angle β, and soil-wall interface friction angle ϕ_w

ϕ (°)	α (°)	β (°)	$\phi_w = 0°$		$\phi_w = 1/3\phi$		$\phi_w = 2/3\phi$	
			Coulomb	Multi-block*	Coulomb	Multi-block*	Coulomb	Multi-block*
30	0	0	3.000	3.000	4.143	4.046	6.105	5.339
		10	4.080	3.997	6.314	5.609	10.903	7.569
		20	5.737	5.164	10.404	7.473	23.373	10.254
	10	0	2.535	2.535	3.292	3.285	4.450	4.243
		10	3.343	3.337	4.742	4.556	7.162	6.045
		20	4.450	4.295	7.053	6.060	12.451	8.179
	20	0	2.274	2.274	2.817	2.817	3.579	3.545
		10	2.952	2.952	3.939	3.911	5.454	5.089
		20	3.809	3.783	5.539	5.214	8.549	6.937
35	0	0	3.690	3.690	5.680	5.469	9.962	7.936
		10	5.228	5.109	9.417	7.957	21.540	11.854
		20	7.822	6.921	17.952	11.192	71.496	16.989
	10	0	3.002	3.002	4.235	4.219	6.466	5.954
		10	4.079	4.074	6.454	6.113	11.618	8.909
		20	5.666	5.464	10.465	8.565	24.509	12.779
	20	0	2.612	2.612	3.455	3.455	4.808	4.988
		10	3.471	3.471	5.035	4.988	7.882	7.088
		20	4.622	4.599	7.505	6.970	13.823	10.196
40	0	0	4.599	4.599	8.147	7.667	18.717	12.549
		10	6.841	6.669	15.193	11.812	58.459	19.924
		20	11.062	9.520	36.591	17.586	908.687	29.978
	10	0	3.587	3.587	5.609	5.570	10.176	8.800
		10	5.043	5.038	9.193	8.502	21.710	13.963
		20	7.363	7.082	16.791	12.640	66.270	21.333
	20	0	3.018	3.018	4.324	4.324	6.797	6.540
		10	4.116	4.116	6.626	6.535	12.338	10.395
		20	5.679	5.659	10.636	9.644	25.741	15.892

*Number of blocks: 471, Number of independent variables: 960

5.2.3 Impact of non-associativity on retaining wall loads

The substitution material characterized by strength parameters c^* and ϕ^*, introduced in Section 4.3, is incorporated into kinematic limit analysis. The solution using the substitution material accounts for non-associativity. The strength parameters of the substitution material are determined as functions of dilation angle ϑ. The effect of non-associativity on retaining wall loads is examined by evaluating the active and passive coefficients for soils whose dilation varies from associative ($\vartheta = \phi$) to incompressible behavior ($\vartheta = 0°$). Four representative dilation angles are considered: $\vartheta = \phi$, $\frac{2}{3}\phi$, $\frac{1}{3}\phi$, and incompressible limit $\vartheta = 0°$. For each dilation angle, the coefficients are computed for wall inclinations $\alpha = 0°$, 10°, and 20°, backfill inclinations $\beta = 0°$, 10°, and 20°, and soil-wall interface friction angles equal to $\frac{2}{3}\phi$, $\frac{1}{3}\phi$, and 0°.

For the active load, the assumed failure surface remains nearly straight, causing the multi-block mechanism to degenerate to a single wedge mechanism. Because of this geometric restriction, the kinematic solution of the active load from multi-block mechanism coincides with Coulomb's classical prediction for all dilation angles. The computed coefficients K_a are shown in Table 5.5. Unlike the factor of safety for slopes, K_a increases as ϕ decreases, meaning that K_a is negatively correlated with ϕ. Therefore, non-associativity leads to an increase in the active earth pressure coefficient. To quantify the impact of non-associativity, the non-associativity impact factor, λ_a, is introduced

$$\lambda_a = \frac{\left|K_a - K_a^*\right|}{K_a} \cdot 100(\%) \tag{5.8}$$

where K_a^* is the active earth pressure coefficient for non-associative soil. Table 5.4 shows the computed results of λ_a. These values of λ_a are computed using the active earth pressure coefficients corresponding to the vertical wall, horizontal backfill, and $\phi_w = \frac{2}{3}\phi$. The results show that the discrepancy between the incompressible soil and the associative soil become larger as the friction angle increases. For example, when $\phi = 40°$, the active earth pressure coefficient at $\vartheta = 0°$ is 33.50% greater than that obtained from the associative flow rule. Fig. 5.13 illustrates this trend by showing how λ_a varies with the degree of non-associativity ($\vartheta = \phi$) for the different internal friction angles.

Table 5.4: Non-associativity impact factor λ_a for retaining wall active loads calculated for different internal friction and dilation angles

λ_a								
$\phi = 30°$			$\phi = 35°$			$\phi = 40°$		
$\vartheta = \frac{2}{3}\phi$	$\vartheta = \frac{1}{3}\phi$	$\vartheta = 0°$	$\vartheta = \frac{2}{3}\phi$	$\vartheta = \frac{1}{3}\phi$	$\vartheta = 0°$	$\vartheta = \frac{2}{3}\phi$	$\vartheta = \frac{1}{3}\phi$	$\vartheta = 0°$
1.68%	6.40%	13.80%	2.87%	10.66%	22.13%	4.50%	16.50%	33.50%

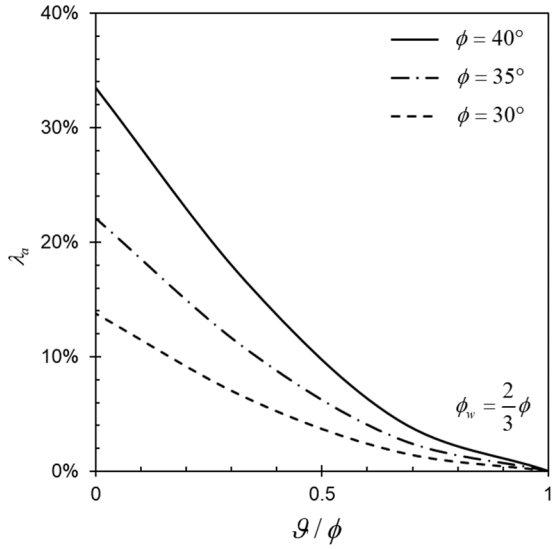


Figure 5.13: Coefficient K_p as a function of ϑ/ϕ

Table 5.5: Active earth pressure coefficient K_a for different dilation angle ϑ, friction angle ϕ, wall angle α, backfill inclination angle β, and soil-wall interface friction angle ϕ_w

			Coulomb											
α (°)	β (°)	ϕ_w / ϕ	$\phi = 30°$				$\phi = 35°$				$\phi = 40°$			
			$\vartheta = \phi$	$\vartheta = \frac{2}{3}\phi$	$\vartheta = \frac{1}{3}\phi$	$\vartheta = 0$	$\vartheta = \phi$	$\vartheta = \frac{2}{3}\phi$	$\vartheta = \frac{1}{3}\phi$	$\vartheta = 0$	$\vartheta = \phi$	$\vartheta = \frac{2}{3}\phi$	$\vartheta = \frac{1}{3}\phi$	$\vartheta = 0$
0	0	0	0.333	0.340	0.356	0.382	0.271	0.279	0.302	0.336	0.217	0.228	0.256	0.298
		1/3	0.308	0.314	0.329	0.352	0.251	0.258	0.278	0.308	0.202	0.212	0.236	0.273
		2/3	0.297	0.302	0.316	0.338	0.244	0.251	0.270	0.298	0.200	0.209	0.233	0.267
	10	0	0.374	0.381	0.401	0.433	0.300	0.310	0.336	0.376	0.238	0.250	0.283	0.332
		1/3	0.350	0.356	0.375	0.404	0.280	0.289	0.313	0.349	0.222	0.234	0.263	0.307
		2/3	0.340	0.347	0.365	0.392	0.275	0.284	0.307	0.342	0.221	0.232	0.261	0.304
	20	0	0.441	0.451	0.480	0.526	0.344	0.356	0.391	0.445	0.267	0.282	0.322	0.385
		1/3	0.420	0.429	0.457	0.503	0.325	0.337	0.369	0.421	0.252	0.266	0.303	0.362
		2/3	0.414	0.424	0.452	0.499	0.323	0.334	0.367	0.419	0.253	0.267	0.304	0.364
10	0	0	0.407	0.413	0.430	0.455	0.343	0.352	0.375	0.409	0.287	0.299	0.328	0.371
		1/3	0.384	0.389	0.404	0.427	0.325	0.333	0.353	0.383	0.273	0.284	0.310	0.348
		2/3	0.377	0.382	0.397	0.418	0.323	0.331	0.351	0.380	0.277	0.287	0.313	0.350

	10	0	0.461	0.468	0.489	0.520	0.384	0.395	0.422	0.463	0.318	0.332	0.366	0.417
		1/3	0.440	0.447	0.467	0.496	0.367	0.377	0.403	0.441	0.305	0.318	0.350	0.397
		2/3	0.438	0.445	0.464	0.493	0.370	0.379	0.405	0.443	0.312	0.325	0.357	0.405
	20	0	0.548	0.558	0.588	0.636	0.444	0.458	0.494	0.552	0.360	0.377	0.421	0.488
		1/3	0.534	0.545	0.575	0.624	0.431	0.445	0.480	0.537	0.350	0.366	0.409	0.474
		2/3	0.540	0.552	0.583	0.635	0.440	0.454	0.491	0.551	0.363	0.379	0.423	0.493
20	0	0	0.498	0.504	0.521	0.546	0.434	0.443	0.466	0.500	0.375	0.387	0.418	0.462
		1/3	0.478	0.484	0.499	0.522	0.419	0.427	0.448	0.479	0.365	0.376	0.404	0.444
		2/3	0.479	0.485	0.500	0.522	0.427	0.435	0.456	0.486	0.381	0.392	0.419	0.459
	10	0	0.572	0.579	0.601	0.633	0.492	0.503	0.532	0.574	0.421	0.436	0.473	0.527
		1/3	0.558	0.565	0.586	0.617	0.482	0.492	0.519	0.561	0.415	0.429	0.464	0.516
		2/3	0.568	0.575	0.596	0.628	0.498	0.508	0.536	0.579	0.438	0.452	0.489	0.542
	20	0	0.687	0.699	0.731	0.782	0.576	0.591	0.630	0.691	0.483	0.502	0.550	0.623
		1/3	0.687	0.699	0.732	0.787	0.574	0.589	0.630	0.694	0.484	0.502	0.551	0.626
		2/3	0.714	0.727	0.764	0.826	0.604	0.621	0.665	0.735	0.518	0.539	0.591	0.674

For the passive load, the failure surface does not remain straight but develops a curved profile, allowing the multi-block mechanism to take advantage of its geometric flexibility. This contrasts with the active case, where the mechanism collapses to a single wedge. Because of this enhanced flexibility, the passive problem provides an opportunity to examine how the impact of non-associativity differs when a more complex kinematic mechanism is utilized. The passive earth pressure coefficients obtained by Coulomb's method are summarized in Table 5.8 and those by the multi-block mechanism are summarized in Table 5.9.

To quantify the influence of non-associativity on retaining wall passive loads, non-associativity impact factor for the passive case λ_p. is introduced. Similar to the active load, this factor provides a normalized measure of the deviation between the passive earth pressure coefficient obtained from the associative flow rule and that computed from the non-associative flow rule. By expressing the variation in this dimensionless form, the effect of dilatancy can be evaluated across both the Coulomb wedge and the multi-block mechanism. The non-associativity impact factor λ_p is defined as

$$\lambda_p = \frac{\left|K_p - K_p^*\right|}{K_p} \cdot 100(\%) \tag{5.9}$$

where K_p^* is the passive earth pressure coefficient for non-associative soil. Table 5.6 shows the computed results of λ_p obtained by Coulomb's analysis, and Table 5.7 shows the λ_p obtained by multi-block mechanism. These results correspond to the condition of a horizontal backfill and a vertical wall, with the soil-wall interface friction angle taken as $\phi_w = \frac{2}{3}\phi$.

Table 5.6: Non-associativity impact factor λ_p for retaining wall passive loads calculated using the Coulomb's method for different internal friction and dilation angles

λ_p								
$\phi = 30°$			$\phi = 35°$			$\phi = 40°$		
$\vartheta = \frac{2}{3}\phi$	$\vartheta = \frac{1}{3}\phi$	$\vartheta = 0°$	$\vartheta = \frac{2}{3}\phi$	$\vartheta = \frac{1}{3}\phi$	$\vartheta = 0°$	$\vartheta = \frac{2}{3}\phi$	$\vartheta = \frac{1}{3}\phi$	$\vartheta = 0°$
2.65%	9.24%	17.90%	5.03%	16.33%	29.43%	9.48%	27.80%	45.39%

Table 5.7: Non-associativity impact factor λ_p for retaining wall passive loads calculated using the multi-block mechanism for different internal friction and dilation angles

λ_p								
$\phi = 30°$			$\phi = 35°$			$\phi = 40°$		
$\vartheta = \frac{2}{3}\phi$	$\vartheta = \frac{1}{3}\phi$	$\vartheta = 0°$	$\vartheta = \frac{2}{3}\phi$	$\vartheta = \frac{1}{3}\phi$	$\vartheta = 0°$	$\vartheta = \frac{2}{3}\phi$	$\vartheta = \frac{1}{3}\phi$	$\vartheta = 0°$
5.00%	9.87%	17.55%	4.73%	12.60%	27.67%	5.99%	24.54%	40.37%

Figure 5.14(a) plots the passive earth pressure coefficients computed from both the multi-block mechanism and Coulomb's method for internal friction angles of $\phi = 30°$, 35°, and 40° as a function of ϑ / ϕ. The results show that the classical Coulomb's result is consistently greater than that from the multi-block mechanism. Fig. 5.14(b) illustrates the corresponding non-associativity impact factors. Except for the case of $\phi = 30°$, the impact factor obtained from the Coulomb's method is larger than that from the multi-block mechanism for $\phi = 35°$ and 40°. These trends indicate that for larger friction angles, the increased geometric flexibility of the multi-block mechanism reduces the influence of non-associativity on the retaining wall passive load.

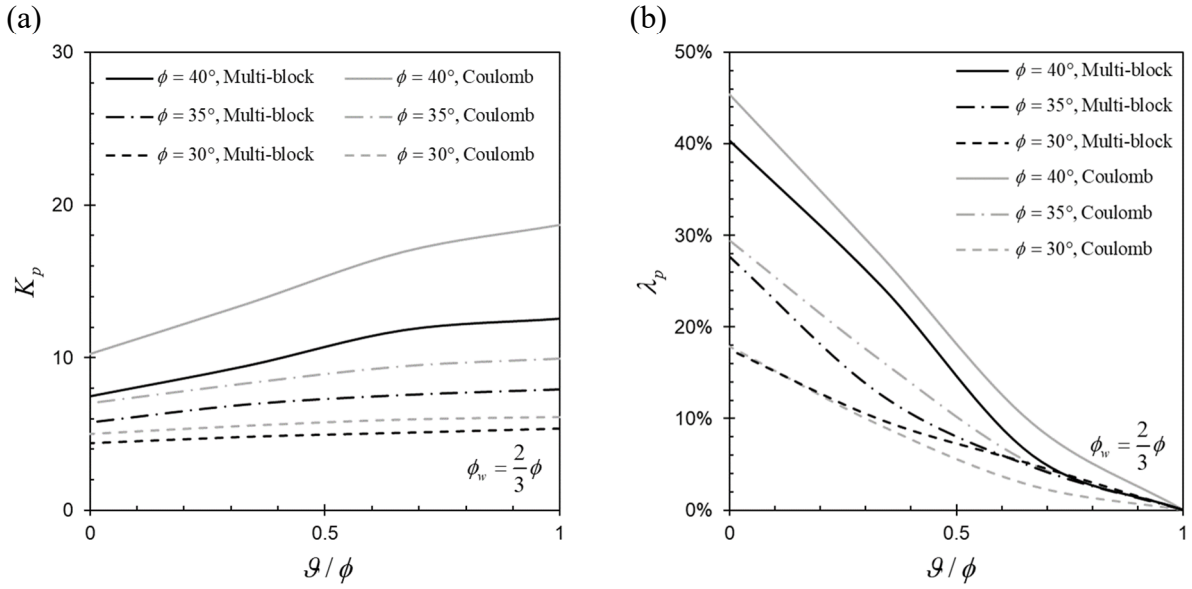


Figure 5.14: (a) Coefficient K_p, and (b) Non-associativity impact factor computed by the multi-block mechanism and Coulomb, as a function of ϑ/ϕ

Table 5.8: Passive earth pressure coefficient K_p obtained by Coulomb's analysis for different dilation angle ϑ, internal friction angle ϕ, wall angle α, backfill inclination angle β, and soil-wall interface friction angle ϕ_w

α (°)	β (°)	ϕ_w / ϕ	Coulomb											
			$\phi = 30°$				$\phi = 35°$				$\phi = 40°$			
			$\vartheta = \phi$	$\vartheta = \frac{2}{3}\phi$	$\vartheta = \frac{1}{3}\phi$	$\vartheta = 0$	$\vartheta = \phi$	$\vartheta = \frac{2}{3}\phi$	$\vartheta = \frac{1}{3}\phi$	$\vartheta = 0$	$\vartheta = \phi$	$\vartheta = \frac{2}{3}\phi$	$\vartheta = \frac{1}{3}\phi$	$\vartheta = 0$
0	0	0	3.000	2.945	2.807	2.618	3.690	3.578	3.313	2.980	4.599	4.379	3.900	3.355
		1/3	4.143	4.054	3.829	3.528	5.680	5.466	4.967	4.360	8.147	7.630	6.550	5.387
		2/3	6.105	5.943	5.541	5.012	9.962	9.461	8.335	7.030	18.717	16.942	13.514	10.222
	10	0	4.080	3.992	3.771	3.474	5.228	5.037	4.593	4.049	6.841	6.439	5.591	4.662
		1/3	6.314	6.150	5.741	5.205	9.417	8.971	7.962	6.783	15.173	13.923	11.407	8.989
		2/3	10.903	10.536	9.643	8.510	21.540	20.045	16.850	13.435	58.459	49.564	34.729	23.053
	20	0	5.737	5.585	5.207	4.710	7.822	7.463	6.646	5.682	11.062	10.221	8.519	6.770
		1/3	10.404	10.054	9.201	8.120	17.952	16.787	14.267	11.527	36.591	31.993	23.800	16.759
		2/3	23.373	22.248	19.615	16.487	71.496	62.972	46.974	32.820	908.687	512.522	197.400	84.451
10	0	0	2.535	2.497	2.400	2.267	3.002	2.928	2.750	2.522	3.587	3.448	3.140	2.778
		1/3	3.292	3.234	3.088	2.888	4.235	4.107	3.806	3.427	5.609	5.332	4.733	4.056
		2/3	4.450	4.357	4.121	3.805	6.466	6.219	5.645	4.948	10.176	9.486	8.061	6.555

	10	0	3.343	3.284	3.136	2.933	4.079	3.960	3.677	3.322	5.043	4.809	4.302	3.721
		1/3	4.742	4.645	4.399	4.070	6.454	6.221	5.677	5.013	9.193	8.629	7.449	6.177
		2/3	7.162	6.981	6.531	5.939	11.618	11.056	9.788	8.318	21.710	19.704	15.824	12.088
	20	0	4.450	4.357	4.121	3.805	5.666	5.464	4.994	4.417	7.363	6.941	6.049	5.067
		1/3	7.053	6.875	6.432	5.849	10.465	9.982	8.888	7.608	16.791	15.417	12.689	9.963
		2/3	12.451	12.044	11.051	9.791	24.509	22.843	19.278	15.459	66.270	56.312	39.676	26.543
20	0	0	2.274	2.246	2.174	2.074	2.612	2.559	2.431	2.264	3.018	2.923	2.709	2.451
		1/3	2.817	2.777	2.674	2.531	3.455	3.371	3.169	2.910	4.324	4.153	3.777	3.335
		2/3	3.579	3.518	3.363	3.152	4.808	4.662	4.318	3.886	6.797	6.445	5.689	4.842
	10	0	2.952	2.910	2.802	2.652	3.471	3.389	3.191	2.937	4.116	3.963	3.624	3.222
		1/3	3.939	3.874	3.709	3.483	5.035	4.891	4.549	4.120	6.626	6.312	5.633	4.864
		2/3	5.454	5.346	5.074	4.707	7.882	7.594	6.926	6.114	12.338	11.530	9.862	8.095
	20	0	3.809	3.744	3.579	3.354	4.622	4.491	4.179	3.786	5.679	5.424	4.868	4.228
		1/3	5.539	5.429	5.152	4.780	7.505	7.242	6.629	5.879	10.636	10.002	8.672	7.234
		2/3	8.549	8.340	7.821	7.138	13.823	13.173	11.706	10.000	25.741	23.412	18.900	14.543

Table 5.9: Passive earth pressure coefficient K_p obtained by the multi-block mechanism for different dilation angle ϑ, internal friction angle ϕ, wall angle α, backfill inclination angle β, and soil-wall interface friction angle ϕ_w

α (°)	β (°)	ϕ_w / ϕ	Multi-block mechanism*											
			$\phi = 30°$				$\phi = 35°$				$\phi = 40°$			
			$\vartheta = \phi$	$\vartheta = \frac{2}{3}\phi$	$\vartheta = \frac{1}{3}\phi$	$\vartheta = 0$	$\vartheta = \phi$	$\vartheta = \frac{2}{3}\phi$	$\vartheta = \frac{1}{3}\phi$	$\vartheta = 0$	$\vartheta = \phi$	$\vartheta = \frac{2}{3}\phi$	$\vartheta = \frac{1}{3}\phi$	$\vartheta = 0$
0	0	0	3.000	2.945	2.807	2.618	3.690	3.630	3.321	2.980	4.599	4.410	3.902	3.355
		1/3	4.046	3.960	3.742	3.447	5.469	5.260	4.921	4.213	7.667	7.302	6.200	5.125
		2/3	5.339	5.072	4.812	4.402	7.936	7.561	6.936	5.740	12.549	11.797	9.470	7.483
	10	0	3.997	3.878	3.668	3.407	5.109	5.014	4.584	3.967	6.669	6.412	5.464	4.561
		1/3	5.609	5.380	5.021	4.657	7.957	7.606	7.000	5.861	11.812	10.911	9.145	7.338
		2/3	7.569	7.211	6.681	6.072	11.854	11.336	9.992	8.166	19.924	18.575	14.260	10.968
	20	0	5.164	4.969	4.639	4.273	6.921	6.663	5.897	5.118	9.520	9.067	7.323	6.041
		1/3	7.473	6.924	6.372	6.014	11.192	10.721	8.989	7.824	17.586	16.469	12.911	10.114
		2/3	10.254	10.085	9.258	7.957	16.989	16.070	12.776	11.077	29.978	27.519	20.984	15.377
10	0	0	2.535	2.483	2.389	2.267	3.002	2.948	2.701	2.522	3.587	3.508	3.085	2.778
		1/3	3.285	3.264	3.105	2.881	4.219	4.111	3.702	3.411	5.570	5.362	4.604	4.023
		2/3	4.243	4.204	3.849	3.614	5.954	5.796	5.168	4.550	8.800	8.290	7.053	5.731

	10	0	3.337	3.310	3.224	2.927	4.074	4.003	3.598	3.316	5.038	4.902	4.201	3.716
		1/3	4.556	4.501	4.152	3.906	6.113	6.001	5.524	4.751	8.502	8.056	6.963	5.756
		2/3	6.045	6.000	5.703	5.017	8.909	8.725	7.437	6.507	13.963	13.356	10.843	8.442
	20	0	4.295	4.254	3.909	3.670	5.464	5.357	4.751	4.262	7.082	6.687	5.760	4.889
		1/3	6.060	6.017	5.723	5.046	8.565	8.373	6.820	6.337	12.640	11.906	9.790	7.924
		2/3	8.179	8.090	7.823	6.604	12.779	12.429	9.951	8.858	21.333	20.001	15.304	11.862
20	0	0	2.274	2.246	2.191	2.074	2.612	2.587	2.398	2.264	3.018	2.960	2.692	2.451
		1/3	2.817	2.793	2.651	2.531	3.455	3.391	3.146	2.910	4.324	4.212	3.715	3.335
		2/3	3.545	3.505	3.197	3.111	4.712	4.651	4.313	3.783	6.540	6.264	5.458	4.618
	10	0	2.952	2.930	2.831	2.652	3.471	3.420	3.174	2.937	4.116	4.021	3.575	3.222
		1/3	3.911	3.875	3.763	3.451	4.988	4.900	4.460	4.070	6.535	6.290	5.542	4.780
		2/3	5.089	5.041	4.951	4.361	7.088	6.938	5.999	5.463	10.395	10.005	8.278	6.857
	20	0	3.783	3.755	3.676	3.325	4.599	4.551	4.163	3.760	5.659	5.464	4.775	4.204
		1/3	5.214	5.165	5.071	4.479	6.970	6.837	5.930	5.443	9.644	9.392	7.798	6.581
		2/3	6.937	6.853	6.434	5.771	10.196	9.861	7.538	7.485	15.892	14.493	11.982	9.687

*Number of blocks: 471, Number of independent variables: 960

5.3 Shallow foundations

Shallow foundations can be subjected to vertical, horizontal, and moment loading, and collapse mechanisms can develop in various forms depending on the load. The failure mechanism beneath a footing is not necessarily constrained to a single dominant pattern. The optimal mechanism depends strongly on the loading condition. A mechanism that provides the lowest collapse load for a purely vertical loading case may no longer remain critical in the presence of horizontal or moment loads.

Experimental observations summarized in Section 4.1 show that soils do not follow the associative flow rule, and this discrepancy can lead to bearing capacity factors that differ markedly from classical predictions. To account for this effect, a substitution material representing non-associative flow rule is adopted. Strength parameters of a substitution material, c^* and ϕ^*, are determined using Eq. (5.4), following the derivation presented in Section 4.3.

5.3.1 Translational mechanisms

A central vertical force is the most straight-forward case of loading on a footing. Because such loading is symmetric only half of the collapse mechanism is considered. Fig. 5.15 shows the multi-block translational mechanism. This mechanism was first introduced by the author in Kim and Michalowski (2024). This rigid-body translational mechanism consists of multiple quadrangular and triangular blocks. The hodograph in Fig. 5.15(b) illustrates the block velocities and the velocity discontinuity vectors (velocity jumps). Velocity jumps at interfaces between blocks are inclined at an angle of internal friction to the block interfaces, Fig. 5.15(c). Inclinations of the block interfaces serve as independent geometric variables of the mechanism. Let m denote the total number of independent blocks, and let a denote the number of blocks bordering block a along piece-wise linear kinematic discontinuity AC, Fig. 5.15(a). The total number of independent variables can be found from formula $2\,(m-1)+a$. All independent variables are optimized to obtain the best estimate of the upper-bound to the true limit load.

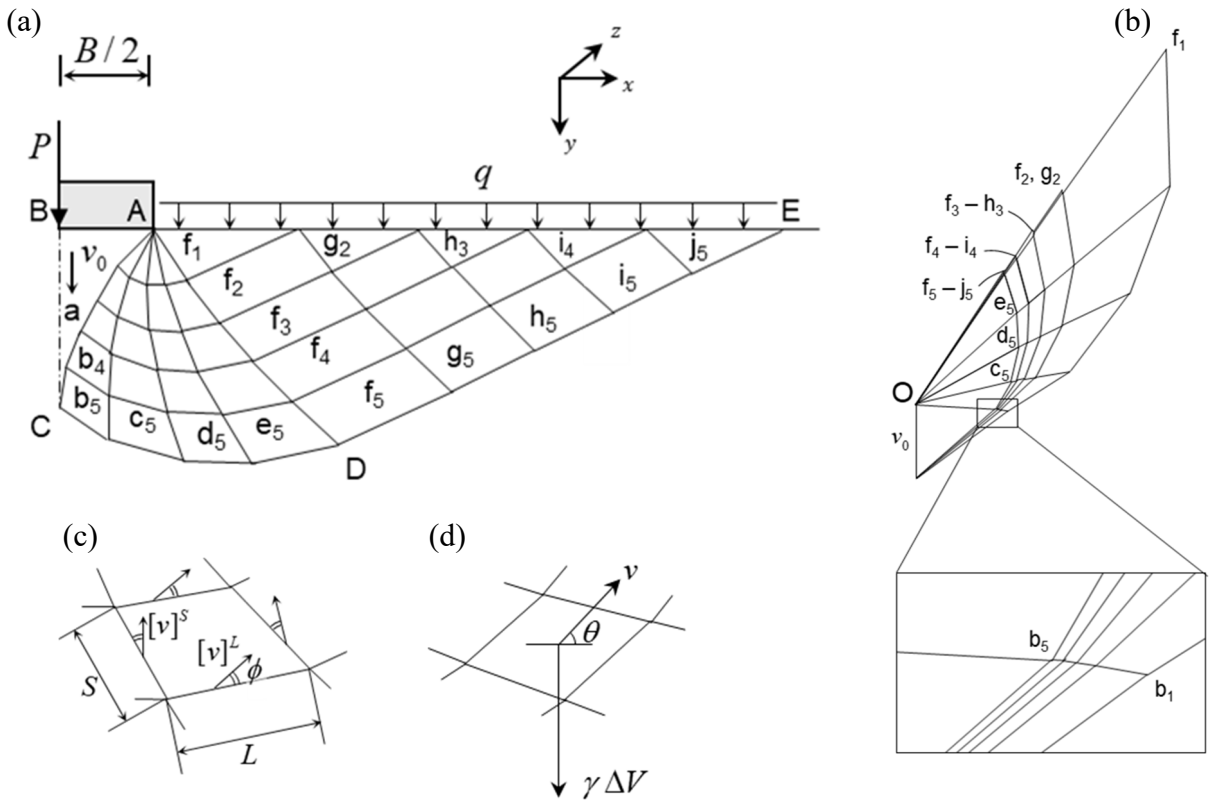


Figure 5.15: (a) Half of a symmetric translational mechanism, (b) hodograph, (c) example volume element used for calculating the work dissipation rate, and (d) example volume element used for calculating the work rate of soil weight

By conforming to the labeling convention of blocks in Fig. 5.15(a), inequality (4.12) can be rewritten as

$$P \leq \frac{D - W_\gamma - W_q}{v_0} \tag{5.10}$$

where P is the true limit load, W_γ is the work rate by the soil weight, W_q is the work rate by surcharge q, D is the work dissipation rate, and v_0 is the velocity shared by the footing and block a. Expressions for W_γ, W_q, and D can be written using the labeling convention of blocks in Fig. 5.15

$$
\begin{aligned}
D &= c\cos\phi([v]_a^L L_a + [v]_a^S S_a + [v]_{b_1}^L L_{b_1} + [v]_{b_1}^S S_{b_1} + \cdots + [v]_{j_5}^L L_{j_5} + [v]_{j_5}^S S_{j_5}) \\
W_\gamma &= -\gamma(V_a v_a \sin\theta_a + V_{b_1} v_{b_1} \sin\theta_{b_1} + V_{b_2} v_{b_2} \sin\theta_{b_2} + \cdots + V_{j_5} v_{j_5} \sin\theta_{j_5}) \\
W_q &= -q(l_{f_1} v_{f_1} \sin\theta_{f_1} + l_{g_2} v_{g_2} \sin\theta_{g_2} + l_{h_3} v_{h_3} \sin\theta_{h_3} + l_{i_4} v_{i_4} \sin\theta_{i_4} + l_{j_5} v_{j_5} \sin\theta_{j_5})
\end{aligned}
\tag{5.11}
$$

where γ is the unit weight of soil, q is surcharge load, θ is the counter-clockwise angle of the block's velocity vector from the x-axis, Fig. 5.15(d). $[v]^S$ and $[v]^L$ are velocity jumps at the interface of each block. S and L are lengths of the interfaces of each block, Fig. 5.15(c). l denotes the length of a side of a triangular block that is in contact with line AE, Fig. 5.16.

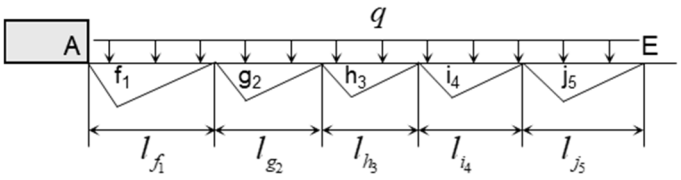


Figure 5.16: Elements for computing W_q and their corresponding horizontal lengths

The symmetric translational mechanism, Fig. 5.15, may be familiar in appearance, yet it represents the first formal proposal of this mechanism within analytical limit analysis. It proves especially effective when the footing is subjected solely to a vertical load. Among all constructed mechanisms, it consistently provides the most accurate upper-bound (for other mechanisms see Martin, 2005). When the load is not symmetric, one can expect the corresponding mechanism also to be non-symmetric. Fig. 5.17 shows the non-symmetric translational mechanism. The footing is subjected to vertical load P, horizontal load T, and surcharge load q. This rigid-body translational mechanism consists of multiple quadrangular blocks and triangular blocks. The hodograph in Fig. 5.17(b) illustrates the block velocities and the velocity discontinuity vectors across their interfaces. Velocity jumps at interfaces between blocks are inclined at an angle of internal friction to the block interfaces, Fig. 5.17(c). Inclinations of the block interfaces serve as independent geometric variables of the mechanism. All independent variables are optimized to obtain the best estimate of limit load P. Because only one external load can be treated as an independent unknown in limit analysis, the horizontal load is described as $T = kP$, with k defining the inclination of the load.

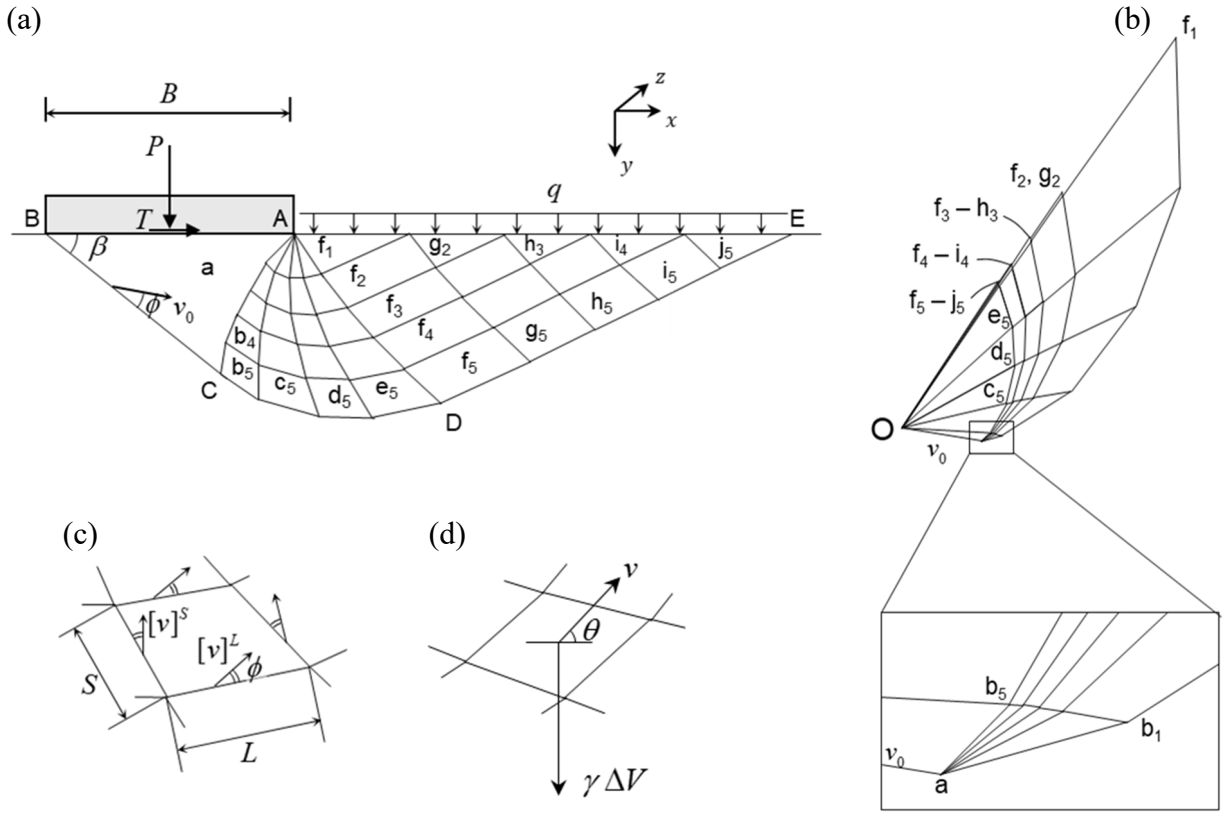


Figure 5.17: (a) Non-symmetric translational mechanism, (b) hodograph, (c) example volume element used for calculating the dissipation rate, and (d) example volume element used for calculating the work rate of soil weight

By conforming to the labeling convention of blocks in Fig. 5.17(a), inequality (4.12) can be rewritten as

$$P \le \frac{D - W_\gamma - W_q}{v_0[\sin(\beta-\phi) + k\cos(\beta-\phi)]} \tag{5.12}$$

where P is the true limit load, W_γ is the work rate by the soil weight, W_q is the work rate by surcharge q, D is the work dissipation rate, and v_0 is the rigid-body translational velocity shared by the footing and block a. W_γ, W_q, and D can be described as

$$\begin{aligned} D &= c\cos\phi([v]_a^L L_a + [v]_a^S S_a + [v]_{b_1}^L L_{b_1} + [v]_{b_1}^S S_{b_1} + \cdots + [v]_{j_5}^L L_{j_5} + [v]_{j_5}^S S_{j_5}) \\ W_\gamma &= -\gamma(V_a v_a \sin\theta_a + V_{b_1} v_{b_1} \sin\theta_{b_1} + V_{b_2} v_{b_2} \sin\theta_{b_2} + \cdots + V_{j_5} v_{j_5} \sin\theta_{j_5}) \\ W_q &= -q(l_{f_1} v_{f_1} \sin\theta_{f_1} + l_{g_2} v_{g_2} \sin\theta_{g_2} + l_{h_3} v_{h_3} \sin\theta_{h_3} + l_{i_4} v_{i_4} \sin\theta_{i_4} + l_{j_5} v_{j_5} \sin\theta_{j_5}) \end{aligned} \tag{5.13}$$

where γ, q, and θ are the unit weight of soil, the surcharge load, and the counter-clockwise angle of the block's velocity vector with respect to the x-axis, respectively. Velocity jumps at the interface of each block are $[v]^S$ and $[v]^L$. S and L represent lengths of block interfaces, Fig. 5.17(c). l denotes the length of a side of a triangular block that is in contact with line AE, Fig. 5.16.

5.3.2 Rotational and mixed mechanisms

Dual-rotation mechanism, which was first introduced by the author in Kim and Michalowski (2024). is shown in Fig. 5.18. It consists of two soil blocks rotating about each centers O and Q with identical angular velocity ω. The mechanism is separated by velocity discontinuity BC. Block ABCA rotates about point O and block BCDB rotates about point Q.

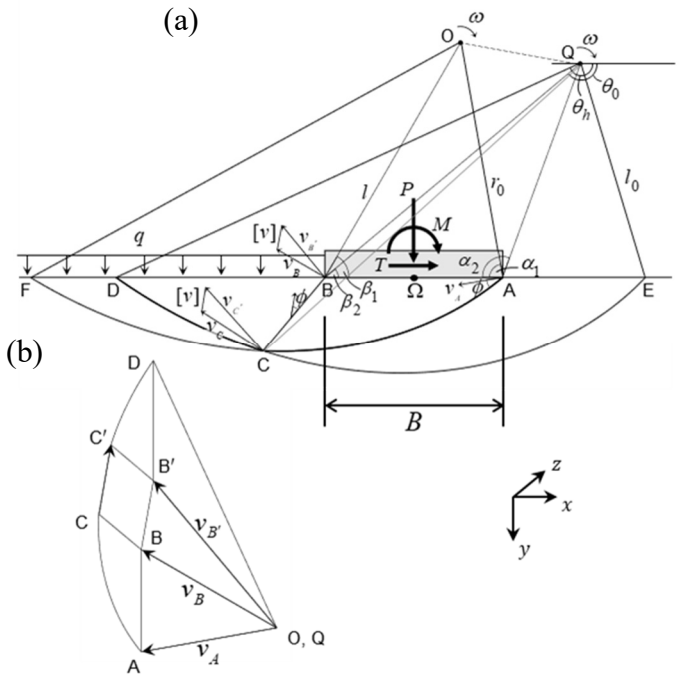


Figure 5.18: (a) Dual-rotational mechanism, and (b) hodograph

Dual-rotational mechanism only includes blocks ABCA and BCDB, with curve AC being a section of log-spiral ACD, and curve CD is a section of log-spiral ECD. Velocity jump $[v]$ along velocity discontinuity BC, has the direction perpendicular to line OQ. The hodograph in Fig. 5.18(b) shows the velocities in the dual-rotational mechanism.

The mechanism in Fig. 5.18(a) is fully defined by four independent variables, α_1, α_2, β_1, and β_2. α_1 and α_2 define the rotation center O, while β_1 and β_2 define the rotation center Q. The four independent variables are optimized to obtain the least estimate of the vertical force P. Since limit analysis only allows one variable for calculation, horizontal force T and moment M are taken as $T = kP$, $M = Pe$ (e being the eccentricity of the force). To obtain P, inequality (4.12) is specified as

$$P \le \frac{D - W_\gamma - W_q}{v_y^\Omega + k v_x^\Omega + e\omega} = \frac{D - W_\gamma - W_q}{\omega\left[\frac{B}{2} - l(\cos\beta_1 + k\sin\beta_1) + e\right]} \tag{5.14}$$

where P is the true limit load, v_y^Ω is the y component of velocity vector of the footing center Ω, v_x^Ω is x component of velocity vector of the footing center Ω, k defines inclination of P, e is its eccentricity, W_γ is the work rate by the soil weight, W_q is the work rate by surcharge q, D is the work dissipation rate, and l is the length of line OB. W_γ, W_q, and D can be obtained by the following equation

$$\begin{aligned} D &= \frac{cr_0\omega}{2\tan\phi}\left[e^{2(\pi-\beta_1-\alpha_1)\tan\phi} - 1\right] + \frac{cl_0\omega}{2\tan\phi}\left[e^{2(\theta_h-\theta_0)\tan\phi} - 1\right] + c[v]L_{BC}\cos\phi \\ W_\gamma &= -\gamma\int_V v\sin\theta\, dV \\ W_q &= -q\int_{L_{BD}} v\sin\theta\, dL \end{aligned} \tag{5.15}$$

where c is the cohesion, ϕ is the internal friction angle, r_0 is the length of line OA, l_0 is the length of line QE, θ_0 is the clockwise angle of inclination of line QC with respect to the x-axis, θ_h is the clockwise angle of inclination of line QD with respect to the x-axis, L_{BC} is the length of line BC, and θ is the counter-clockwise angle of velocity vector of the element, with respect to x-axis.

The second mechanism accounting for rotation and considered here is the mixed mechanism shown in Fig. 5.19. This mechanism is similar to that used by Salençon and Pecker (1995) and Michalowski and You (1998). This mechanism encompasses a rigid rotation, including the footing and soil region CDAC, both rotating about point O with angular velocity ω.

The soil internal friction angle is ϕ while the footing-soil interface friction angle is ϕ_w. Velocity v_C is inclined at an angle of ϕ_w, with respect to the footing-soil interface.

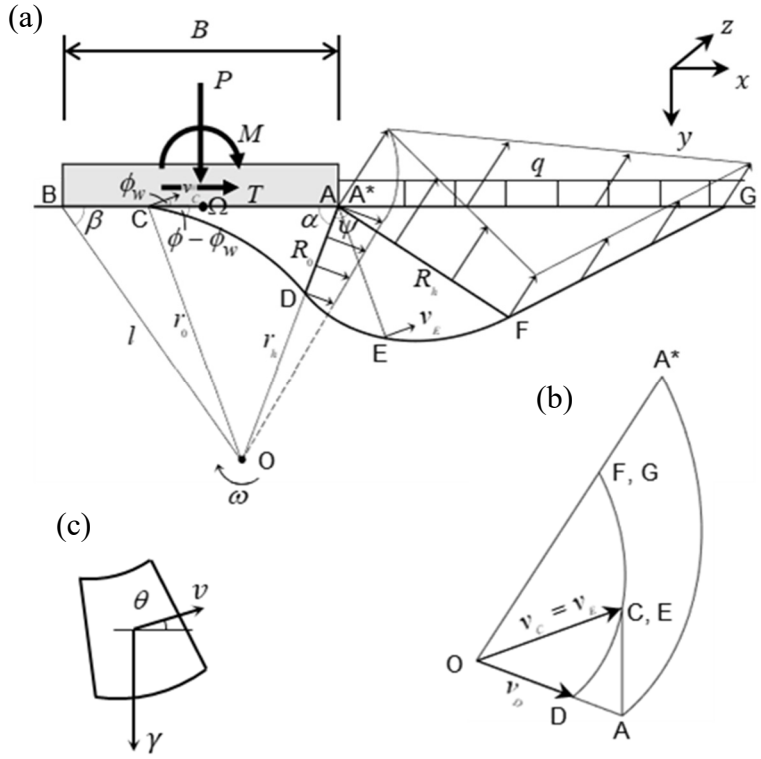


Figure 5.19: (a) Mixed mechanism, (b) hodograph, and (c) example volume element in region ADFA used for calculating the work rate of soil weight

As region CDAC is subjected to rigid rotation, line CD is a section of a log-spiral. As line CDEFG is smooth, the only velocity discontinuity is line CDEFG. Point D is an inflection point, and line DEF is a log spiral, region ADEFA is subjected to continual shear, not rigid rotation. Region AFGA is subjected to simple shear deformation and rigid translation. Point A is a singular point, so that velocity at point A takes a continuum of magnitudes and directions. Velocity at point A is represented in the hodograph by the log-spiral curve AA^*, Fig. 5.19(b).

Mixed mechanism, Fig. 5.19(a), can be fully described by three independent variables: α, β, and ψ. Three independent variables are optimized to obtain the best estimate of the true limit load. To obtain P, inequality (4.12) can be rewritten for mixed mechanism as

$$P \le \frac{D - W_\gamma - W_q}{v_y^\Omega + k v_x^\Omega + e\omega} = \frac{D - W_\gamma - W_q}{\omega\left[\frac{B}{2} - l(\cos\beta - k\sin\beta) + e\right]} \tag{5.16}$$

where P is the true limit load, v_x^Ω and v_y^Ω are the y component and x component of velocity vector of the footing center Ω, l is the length of line OB, β is ∠ABO, k defines inclination of P, e is its eccentricity, W_γ is the work rate by the soil weight, W_q is the work rate by the surcharge q, and D is the work dissipation rate. W_γ, W_q, and D can be obtained by the following equation

$$\begin{aligned} D &= D_{CD} + D_{DF} + D_{FG} + D_{ADFA} + D_{AFGA} \\ W_\gamma &= -\gamma \int_V v \sin\theta \, dV \\ W_q &= -q \int_{L_{AG}} v \sin\theta \, dL \end{aligned} \tag{5.17}$$

where θ is the counter-clockwise angle of velocity vector of the element, with respect to x-axis. When calculating the total work dissipation rate, the dissipation contributions must be evaluated separately depending on the type of deformation. For the planar kinematic discontinuities along curves CD, DF, and FG, the dissipation is computed from the velocity jump across each discontinuity surface. In contrast, regions ADFA and AFGA undergo plastic deformation, and the dissipation in these zones is evaluated using $\int_V \sigma_{ij}^{pl} \dot{\varepsilon}_{ij}^{pl} dV$. The total work dissipation rate is obtained by summing the contributions from all discontinuity lines and volumetric regions. Detailed formulation of each component can be found in Michalowski and You (1998).

5.3.3 Combined loads on footings

Prager (1959) introduced the concept of generalized loads and generalized velocities, which enables simultaneous consideration of vertical force P, horizontal force T, and overturning moment M within a single unified framework. This generalized load formulation leads to a three-dimensional surface in the load space, which represents the yield locus of a strip footing. Following this approach, combined loading on shallow foundation is examined in the normalized load space $P/\gamma B^2$, $T/\gamma B^2$, and $M/\gamma B^3$, where each coordinate represents a dimensionless load component

associated with a generalized term. Combined loads were obtained by prescribing a force inclination coefficient $k = T / P$ and a load eccentricity $e/B = M / PB$. For each prescribed value, the limit load was computed using collapse mechanisms, introduced in Sections 5.3.1 and 5.3.2. Prescribing k and e/B places the resulting limit load on the yield locus, at the cross-section with line OC in Fig. 5.20.

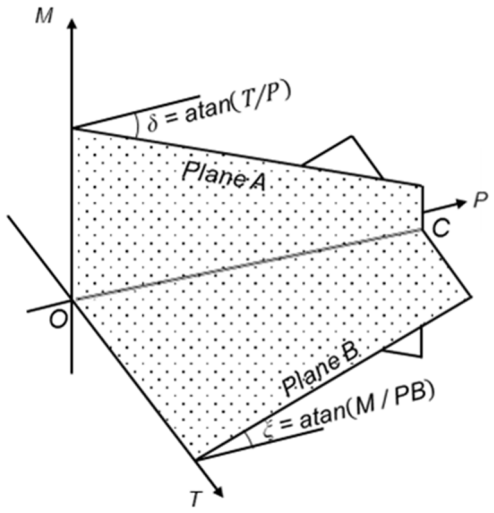


Figure 5.20: Proportional loading path OC in the multi-parameter load space

The computed limit load corresponds to a single point in the 3D normalized load space. Each point therefore reflects both the combined loads and the collapse mechanism governing under that combination. By assembling these points, the yield locus of the footing is obtained. The resulting yield surface is shown in Fig. 5.21, which illustrates how the governing mechanism shifts as the load combination varies.

The symmetric translational, non-symmetric translational, dual-rotation, and mixed mechanisms introduced in Section 5.3.1 and 5.3.2 are used to generate the 3D footing yield locus for the commonly assumed associative flow rule (the symmetric and non-symmetric translational mechanisms each consists of 471 blocks with 960 independent variables). Then, by applying the substitution material described in Section 4.3, the same computations are repeated for non-associative soil. Comparison of these two yield loci enables direct assessment of how non-associativity impacts the geometry of the 3D yield locus and the governing collapse mechanism in

the combined loading domain. Fig. 5.21 shows the yield locus for a strip footing obtained using associative soil that has strength parameters of $c = 0$ kPa and $\phi = 35°$, and substitution material that is an extreme case of incompressibility. The normalized surcharge is given as $q/\gamma B = 1$, and interface friction angle is given as $\phi_w = \frac{2}{3}\phi$. A small white region near the origin of the normalized load space corresponds to failure controlled by surface sliding at the footing-soil interface. Because the normality rule is enforced, the sliding direction, $\dot{p}$ in Fig. 5.21, does not align with the horizontal ground surface, but includes a dilative component. Short edges exist on the yield locus where the sliding region (white) meets the areas governed by mixed mechanism (red) and dual-rotation (blue). Other short edges exist on the yield where the area governed by translational mechanism (grey) meets the red and blue areas. Along these edges, the surface has no unique gradient, meaning that multiple mechanisms may be activated for the same load state.

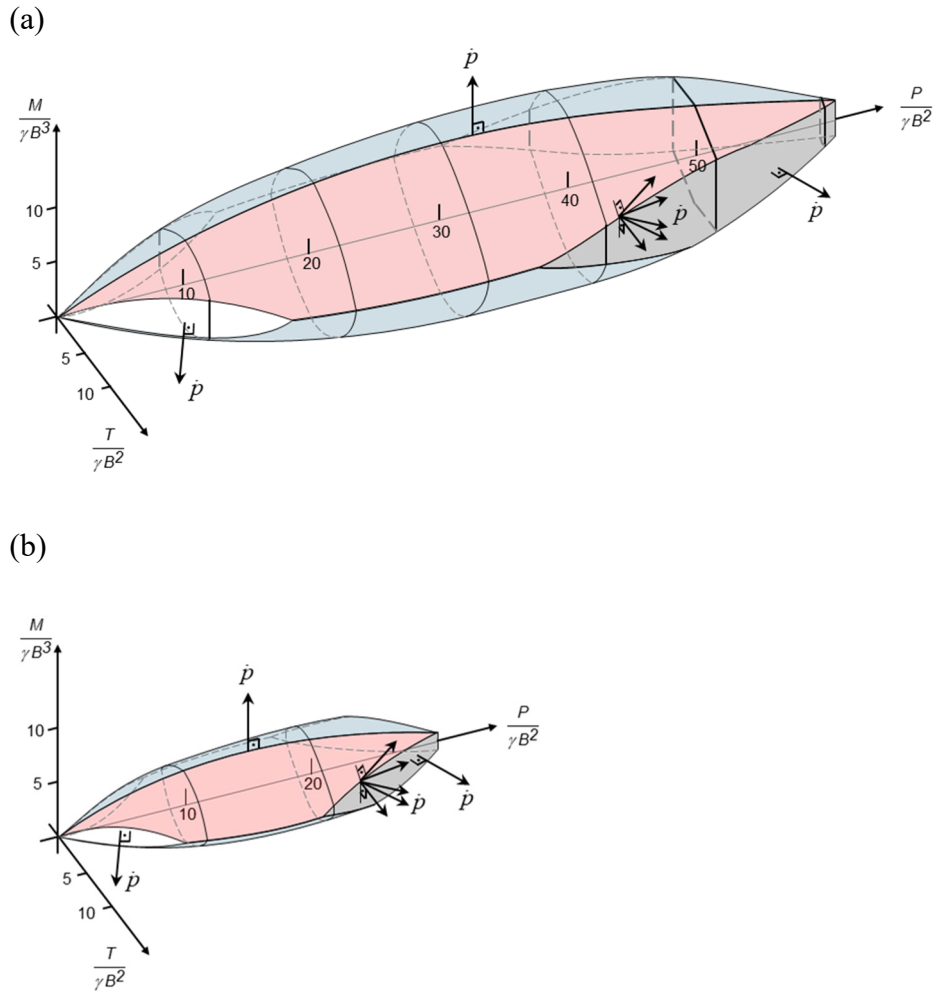


Figure 5.21: Yield locus for a strip footing with $\phi = 35°$, $\phi_w = 2/3 \cdot \phi$, and normalized surcharge load of $q/(\gamma B) = 1$: (a) associative soil; (b) non-associative soil with dilation angle $\vartheta = 0°$

The 3D footing yield locus exhibits a cigar-shaped form, and its shape is controlled by soil strength parameters c and ϕ, and the normalized surcharge parameter $q/(\gamma B)$. As the strength parameters or normalized surcharge parameter decrease, the entire surface contracts toward the origin, indicating that points farther away from the origin are more sensitive to non-associativity.

5.3.4 Impact of non-associativity on bearing capacity of footings

A common way to represent the bearing capacity of a strip footing is through a three-term formula, which separately accounts for the effects of soil cohesion, overburden load, and soil weight on the resistance of the soil to bear loads. To investigate how non-associativity influences each component in this formulation, it is convenient to express the results in terms of the bearing capacity. The symmetric translational mechanism, Fig. 5.15, is the most effective for vertical loading, and this mechanism is adopted to evaluate the corresponding changes in N_c, N_q, and N_γ with the change in dilation angle (the influence of non-associativity). Bearing capacity factors for different internal friction and dilation angles are given in Tables 5.10, 5.11, and 5.12, respectively, with the mechanism comprising 471 blocks and 960 independent variables.

Table 5.10: Bearing capacity factor N_c for footings subjected to a vertical load calculated using multi-block mechanism for different internal friction angles and dilation angles

$\phi = 15°$				$\phi = 20°$				$\phi = 25°$			
$\vartheta = \phi$	$\vartheta = \frac{2}{3}\phi$	$\vartheta = \frac{1}{3}\phi$	$\vartheta = 0$	$\vartheta = \phi$	$\vartheta = \frac{2}{3}\phi$	$\vartheta = \frac{1}{3}\phi$	$\vartheta = 0$	$\vartheta = \phi$	$\vartheta = \frac{2}{3}\phi$	$\vartheta = \frac{1}{3}\phi$	$\vartheta = 0$
10.977	10.941	10.837	10.674	14.835	14.708	14.358	13.832	20.721	20.339	19.337	17.932
$\phi = 30°$				$\phi = 35°$				$\phi = 40°$			
$\vartheta = \phi$	$\vartheta = \frac{2}{3}\phi$	$\vartheta = \frac{1}{3}\phi$	$\vartheta = 0$	$\vartheta = \phi$	$\vartheta = \frac{2}{3}\phi$	$\vartheta = \frac{1}{3}\phi$	$\vartheta = 0$	$\vartheta = \phi$	$\vartheta = \frac{2}{3}\phi$	$\vartheta = \frac{1}{3}\phi$	$\vartheta = 0$
30.140	29.069	26.468	23.188	46.124	43.203	36.810	29.753	73.313	67.274	51.986	37.761

Table 5.11: Bearing capacity factor N_q for footings subjected to a vertical load calculated using multi-block mechanism for different internal friction angles and dilation angles

$\phi = 15°$				$\phi = 20°$				$\phi = 25°$			
$\vartheta = \phi$	$\vartheta = \frac{2}{3}\phi$	$\vartheta = \frac{1}{3}\phi$	$\vartheta = 0$	$\vartheta = \phi$	$\vartheta = \frac{2}{3}\phi$	$\vartheta = \frac{1}{3}\phi$	$\vartheta = 0$	$\vartheta = \phi$	$\vartheta = \frac{2}{3}\phi$	$\vartheta = \frac{1}{3}\phi$	$\vartheta = 0$
3.941	3.920	3.859	3.763	6.400	6.314	6.079	5.731	10.662	10.370	9.614	8.581
$\phi = 30°$				$\phi = 35°$				$\phi = 40°$			
$\vartheta = \phi$	$\vartheta = \frac{2}{3}\phi$	$\vartheta = \frac{1}{3}\phi$	$\vartheta = 0$	$\vartheta = \phi$	$\vartheta = \frac{2}{3}\phi$	$\vartheta = \frac{1}{3}\phi$	$\vartheta = 0$	$\vartheta = \phi$	$\vartheta = \frac{2}{3}\phi$	$\vartheta = \frac{1}{3}\phi$	$\vartheta = 0$
18.401	17.476	15.272	12.594	33.296	30.442	24.390	18.066	64.195	55.311	39.174	25.272

Table 5.12: Bearing capacity factor N_γ for footings subjected to a vertical load calculated using multi-block mechanism for different internal friction angles and dilation angles

$\phi = 15°$				$\phi = 20°$				$\phi = 25°$			
$\vartheta = \phi$	$\vartheta = \frac{2}{3}\phi$	$\vartheta = \frac{1}{3}\phi$	$\vartheta = 0$	$\vartheta = \phi$	$\vartheta = \frac{2}{3}\phi$	$\vartheta = \frac{1}{3}\phi$	$\vartheta = 0$	$\vartheta = \phi$	$\vartheta = \frac{2}{3}\phi$	$\vartheta = \frac{1}{3}\phi$	$\vartheta = 0$
1.473	1.457	1.411	1.336	3.557	3.467	3.218	2.860	7.927	7.654	6.925	5.882
$\phi = 30°$				$\phi = 35°$				$\phi = 40°$			
$\vartheta = \phi$	$\vartheta = \frac{2}{3}\phi$	$\vartheta = \frac{1}{3}\phi$	$\vartheta = 0$	$\vartheta = \phi$	$\vartheta = \frac{2}{3}\phi$	$\vartheta = \frac{1}{3}\phi$	$\vartheta = 0$	$\vartheta = \phi$	$\vartheta = \frac{2}{3}\phi$	$\vartheta = \frac{1}{3}\phi$	$\vartheta = 0$
16.468	15.209	12.487	9.704	38.655	34.591	25.476	16.006	90.816	73.149	46.771	26.832

From results in Tables 5.10 through 5.12, it is evident that the impact of non-associativity becomes more pronounced as the internal friction angle increases. To visualize the variation of bearing capacity factors due to changes in dilation angle, Fig. 5.22 is presented. It is noted that $\vartheta / \phi = 1$ corresponds to the associative solution. Fig. 5.22 compares two representative cases, $\phi = 40°$ and $\phi = 20°$, to illustrate how the influence of the dilation angle differs depending on the soil's friction angle. For, $\phi = 40°$, Fig. 5.22(a), the variation of bearing capacity factors, N_c, N_q, and N_γ, with respect to ϑ / ϕ is significantly more pronounced than for $\phi = 20°$, Fig. 5.22(b).

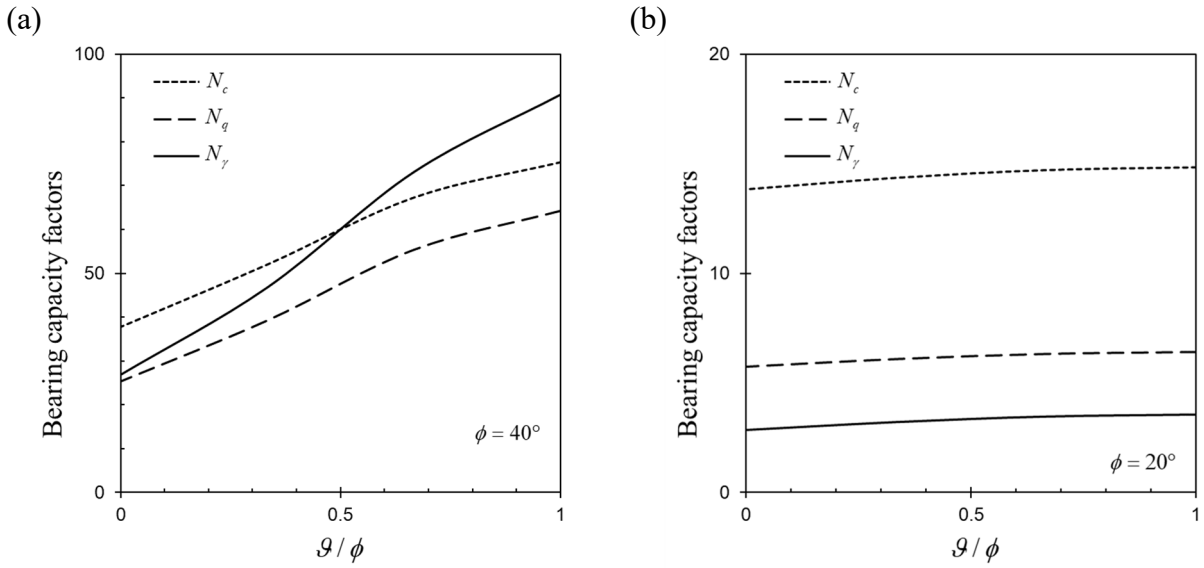


Figure 5.22: Bearing capacity factors for footings subjected to a vertical load for (a) $\phi = 40°$, and (b) $\phi = 20°$

To enable a quantitative assessment, reduction in bearing capacity factors is quantified as the non-associativity impact factor. λ is the non-associativity impact factor, while the subscripts in λ_c, λ_q, and λ_γ denote the corresponding contributions associated with cohesion, surcharge, and soil weight, respectively. The bearing capacity factors obtained from the substitution materials are denoted as N_c^*, N_q^*, and N_γ^*. Since the substitution material modifies the strength parameters, c and ϕ, comparisons involving cohesion must be made using cN_c rather than N_c alone. The relative impact of non-associativity is thus quantitatively evaluated using the following relation

$$\lambda_c = \frac{\left|cN_c - c^* N_c^*\right|}{cN_c} \cdot 100\,(\%)$$
$$\lambda_q = \frac{\left|N_q - N_q^*\right|}{N_q} \cdot 100\,(\%) \qquad (5.18)$$
$$\lambda_\gamma = \frac{\left|N_\gamma - N_\gamma^*\right|}{N_\gamma} \cdot 100\,(\%)$$

Eq. (5.18) provides a direct measure of the effect of non-associative flow rule on bearing capacity of shallow foundations. λ_c, λ_q, and λ_γ versus ratio of the dilation angle to the internal friction angle is shown in Fig. 5.23, $\vartheta / \phi = 1$ corresponding to the associative solution.

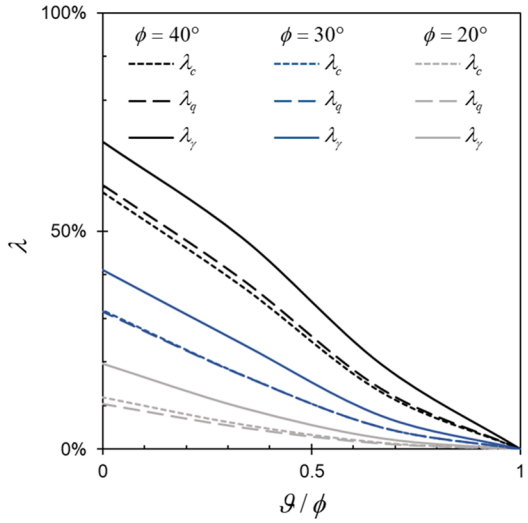


Figure 5.23: Impact of non-associativity on bearing capacity factors for footings subjected to a vertical load

It can be observed that for $\phi = 40°$, the magnitude of the impact follows order $\lambda_\gamma > \lambda_q > \lambda_c$. As the internal friction angle decreases, this order gradually changes to $\lambda_\gamma > \lambda_c > \lambda_q$. The reversal in λ_c and λ_q with increasing ϕ arises from the reduction of the ratio c^* / c as defined in Eq. (5.18). Parameter λ_γ consistently shows the largest values, and its magnitude increases with increasing ϕ. This is because overcoming the soil weight requires substantial work during failure. As the internal friction angle increases, the size of the failure mechanism expands, resulting in a larger volume of soil that must be uplifted, thereby increasing the influence of the soil weight term.

5.4 Discussion of impact

Figure 5.24 presents the non-associativity impact factor, defined by comparing the associative solution with an extreme non-associative flow rule, represented by $\vartheta = 0°$ (incompressible behavior). The result shows that non-associativity consistently leads to a reduction in the factor of safety for slopes, passive load for retaining wall, and bearing capacity of footings. In case of the active load, the computed load increases when non-associativity is considered. This occurs because kinematic limit analysis provides a lower-bound solution to the active earth load, while the actual force calculated corresponds to the reaction force. A stronger soil requires a smaller reaction force, whereas a weaker soil requires a larger reaction force.

Across the geotechnical structures examined, the magnitudes of the impact factors reveal a hierarchy in how strongly each structure is influenced by the non-associativity of plastic flow (or the magnitude of the dilation angle. Non-associativity has the least impact on slopes, with impact factor λ (Eq. 5.3) ranging from 13.40% to 23.40% when ϕ changes from 30° to 40°. Retaining wall loads are more affected, with wall active load impact factor λ_a (Eq. 5.8) ranging from 13.38% to 33.50% when ϕ changes from 30° to 40°, and with wall passive load impact factor λ_p (Eq. 5.9) ranging from 17.55% to 40.37% when ϕ changes from 30° to 40°. The largest impact occurs in bearing capacity factors for footings, where bearing capacity impact factors λ_c, λ_q, and λ_γ (Eq. 5.18) range from 31.87% to 58.97%, from 31.56% to 60.63%, and from 41.07% to 70.45%, respectively, when ϕ changes from 30° to 40°. Overall, problems with mechanisms mobilizing upward velocity are affected by non-associativity the most, whereas slopes remain less sensitive. This is because failure mechanisms that mobilize substantial uplift must do work against the soil weight. As the dilation angle increases, the predicted collapse mechanism for a foundation involves a larger soil mass. For mechanisms mobilizing upward velocities, this implies that the work required to overcome the resistance to failure provided by the soil weight increases with the increase in the dilatancy angle. This leads to a larger sensitivity to non-associativity and hence larger impact factors at higher dilation angles.

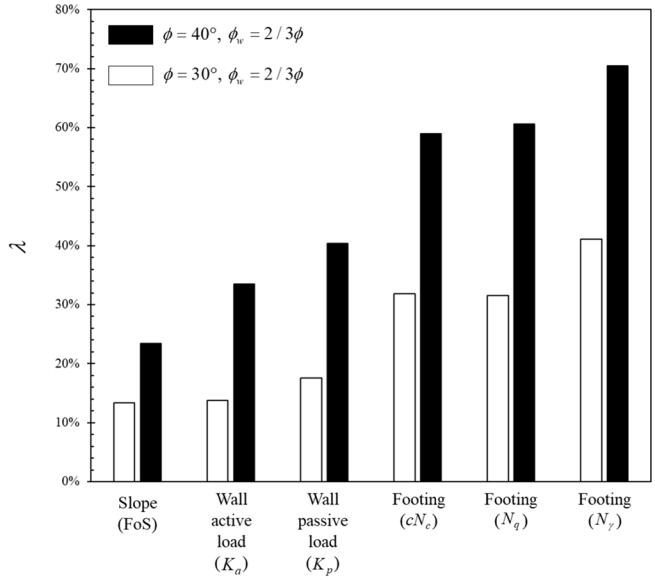


Figure 5.24: Extreme impact of non-associativity on slope stability, retaining wall loads, and bearing capacity factors obtained by comparing associative (ϑ/ϕ) and non-associative flow rule (ϑ=0°) for ϕ=30° and 40°

Chapter 6 Summary and Conclusions

Laboratory data on dense sands show that the measured dilation angles are below the internal friction angle of the soils inferred from the peak shear strength even at low confinement stresses. A similar trend appears in rocks. Tests on jointed or moderately weathered rock masses reveal rupture angles that are consistently smaller than those predicted by Hoek-Brown yield condition and associative plastic flow rule. These observations indicate that real geomaterials experience less volumetric strain than associative plastic flow rule would imply. Associativity exaggerates dilatancy and can produce inaccurate estimate of the limit loads on geotechnical structures. A more nuanced description of volumetric behavior is offered, for example, by critical state models such as Cam clay. Cam clay model adopts the associative flow rule, but it is a hardening-softening model with yield surface enabling it to represent both the contractive and dilative behavior, and also the asymptotic approach to the critical state. This capability makes Cam clay an effective constitutive model for capturing the evolution of volume change in clays. However, Cam clay model is not applicable in limit analysis. In practice, Mohr-Coulomb yield criterion remains the standard framework for stability analysis of geotechnical structures.

Despite experimental evidence to the contrary, current engineering practice in modeling efforts largely rests on associativity idealizations. In routine design, soils are most often modeled with Mohr-Coulomb yield criterion and associative flow rule. Standard bearing capacity factors, earth pressure coefficients, and factor of safety for slopes are calculated under the assumption of associativity. As a result, the impact of non-associativity in stability analyses is not considered in practical calculations, which has motivated several attempts to incorporate non-associative flow rule for soils in stability considerations.

Foundational contributions to non-associativity of soil plastic flow in limit analysis are due to Radenkovic (1962), broadened later by Josselin de Jong (1964), and also considered by Palmer (1966). They established theoretical bounds for non-associative materials, but their practical value proved limited. For the Mohr-Coulomb yield criterion, Radenkovic's theorems collapse to the classical associative solution in the upper-bound approach, and yield a trivial (often

zero) lower bound outcome. While conceptually different and developed in a later generation of research, the bipotential framework offers an alternative approach to non-associativity. The concept of bipotential developed by Saxcé and co-workers (e.g., Saxcé and Bousshine 1998, Chaaba et al 2010) provides a mathematical framework to treat non-associative flow rule within limit analysis. However, their reliance on iterative coupling between stresses and kinematics, together with the convergence difficulties highlight that the bipotential method is not easily applicable to a wide range of geotechnical boundary value problems. Limitations of existing approaches have motivated the use of the framework introduced by Davis (1968). Davis originated a technique to utilize the upper-bound approach of limit analysis to non-associative soil, explicitly defining tractions on velocity characteristics. Michalowski (1989) showed the equivalency of the work balance equation and force equilibrium in translational rigid-body mechanisms. Subsequently, Drescher and Detournay (1993) presented a technique to apply the kinematic theorem of limit analysis to non-associative soils, limited to analyses with translational rigid-block mechanisms.

This thesis focuses on how non-associative plastic flow rule affects solutions to classical geotechnical problems, using some of the developments made originally by Davis (1968). A kinematic limit analysis framework is adopted in which the *substitution material* concept is used to account for the influence of non-associativity. This approach allows the impact of non-associativity to be quantified in a systematic way over realistic ranges of internal friction and dilation angles. A study of three geotechnical problems including slopes, loads on retaining structures, and bearing capacity of shallow foundations highlights the impact of non-associativity on the solutions to different stability measures or limit loads. In all cases, associative solutions to a stability measure or a limit load were compared with solutions obtained using an extreme non-associative flow rule corresponding to incompressible soil behavior. The resulting differences were expressed using non-associativity impact factor λ. The non-associativity impact factor quantifies the relative difference in a stability measure or in a limit load when the associative flow rule is replaced by the non-associative one.

The following points summarize the main conclusions of this study.

- The study revealed that out of all attempts at evaluating the impact of non-associativity on stability measure or limit load on geotechnical structures, it is the approach originated by Davis (1968) that provides a most practical route to include non-associativity in kinematic limit analysis. The Davis's framework leads to computable upper-bounds for non-associative Mohr-Coulomb materials, in contrast to other contributions, which tend to yield trivial bounds or require a rather elaborate implementation in boundary value problems.

- Non-associativity impact factor λ_F for slopes was defined as the relative reduction in the factor of safety, as the dilatancy angle is reduced from its maximum (equal to the internal friction angle) to the true value, with a minimum of zero for incompressible plastic flow. The extreme non-associativity impact occurs as the dilatancy angle is reduced from its maximum value to zero, thus it is dependent on the internal friction angle. The extreme non-associativity impact factor for slopes ranges from 13.40% to 23.40% when the internal friction angle changes from 30º to 40º.

- Introducing the non-associative flow rule increases the computed active loads on the retaining walls. This is because the active wall load enters the kinematic theorem of limit analysis as a reaction force. Extreme non-associativity impact factor, defined as a relative difference in the active wall loads, ranges from 13.38% to 33.50% when the internal friction angle is increased from 30º to 40º. On the contrary, non-associativity decreases the computed passive load on the retaining wall. Extreme non-associativity impact factor for wall passive loads ranges from 17.55% to 40.37% when the internal friction angle changes from 30º to 40º.

- Of the three boundary value problems considered, the most impactful influence of non-associativity was found in bearing capacity of shallow foundations. In the classical bearing capacity calculations, the contribution of the cohesion, overburden, and soil weight components to the bearing capacity are treated independently. Consistently with the classical approach to calculating bearing capacity of shallow footings (Section 5.3.4), the

impact of non-associativity was evaluated separately for each bearing capacity factor. Accordingly, the impact factors are denoted by λ_c, λ_q, and λ_γ, where the subscripts follow those of bearing capacity factors. When the soil internal friction angle is 30º, the following extreme impact factors λ_c, λ_q, and λ_γ were obtained 31.87%, 31.56%, and 41.07%, respectively. For soil internal friction angle of 40º, impact factors λ_c, λ_q, and λ_γ increased to 58.97%, 60.63%, and 70.45%, respectively. Failure mechanisms involving significant uplift of soil mass expend work against gravity. As the dilation angle increases, the collapse mechanism involves a larger participating soil mass, increasing the required work against the soil weight to produce failure. This increases the sensitivity to non-associativity and results in large impact factors.

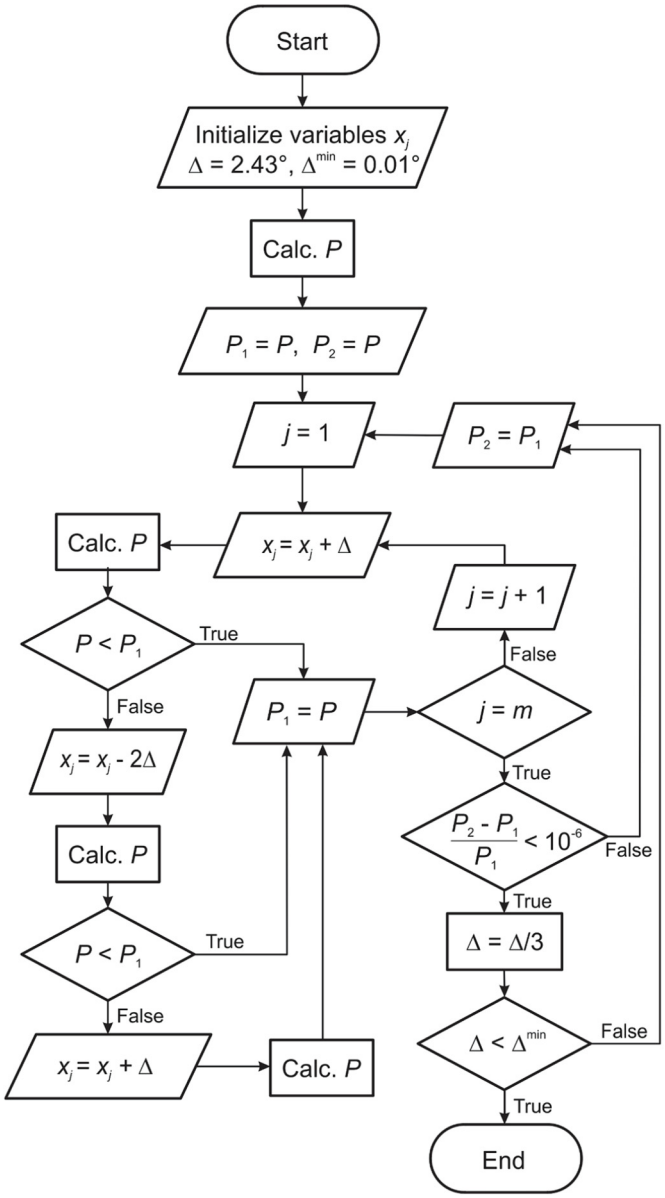
- The dual-rotation mechanism and the multi-block mechanism were developed in course of this study, in order to improve upper-bound solutions to geotechnical boundary value problems (Sections 5.3.1 and 5.3.2). The dual-rotation mechanism yields the most accurate solutions for bearing capacity of footings for certain combinations of non-symmetric (moment-force) loads. The multi-block mechanism is more flexible when compared with the classical multi-wedge failure patterns, and it provides accurate solutions for both bearing capacity of footings and for passive loads on retaining structures.

Appendices

Appendix A: Optimization Process

Optimization of the limit load solutions was conducted to identify the global minimum of the objective function representing the collapse load. While numerous optimization algorithms were explored, the nature of the limit analysis problem posed significant challenges. Due to the strict admissibility constraints associated with limit analysis, many trial solutions generated by numerous algorithms violated the admissibility conditions. Furthermore, the non-convexity of the solution space often caused the search process to converge to local minima instead of the global minima.

To address these challenges, a straight forward “brute-force” optimization method was adopted. Optimization was performed via a stepwise parameter sweep. Starting from an initially kinematically admissible set of independent variables, each variable was adjusted one at a time by an increment. The limit load was recomputed, and kinematic admissibility was rechecked every adjustment. The increment was progressively reduced to refine the minimum. The overall optimization workflow followed the schematic illustrated in Fig. A.1, taken from Kim and Michalowski (2024). In this process, the internal work rate and external work rate were computed for each admissible mechanism, and the limit load was determined by minimizing the ratio of these two quantities. The flow chart in Fig. A.1 represents the iterative evaluation process applied throughout this study. The “brute-force” optimization strategy proved robust across different types of problems such as bearing capacity and retaining wall analysis, ensuring global convergence.



Appendix Figure A.1: Flowchart for optimization of limit load P (Kim and Michalowski 2024)

Bibliography

Arzúa, J. and Alejano, L. R. "Dilation in granite during servo-controlled triaxial strength tests." International Journal of Rock Mechanics and Mining Sciences, 61, 43–56, 2013

Balmer G. "A general analysis solution for Mohr's envelope." Proc ASTM. 52: 1260–1271, 1952

Banerjee, P. K. and Stipho, A. S., "Associated and non-associated constitutive relations for undrained behavior of isotropic soft clays." International Journal for Numerical and Analytical Methods in Geomechanics, Vol. 2, pp. 35–56, 1978

Bishop, A. W. "The use of slip circle in the stability analysis of slopes." Géotechnique 5, No. 1, 7-17, 1955

Bleich, H. "Über die bemessung statisch unbestimmter stahltragwerke unter berücksichtigung des elastisch-plastischen verhaltens des baustoffes." Bauingenieur 13, 261–269, 1932

Bottero, A., Negre, R., Pastor, J., and Turgeman, S. "Finite element method and limit analysis theory for soil mechanics problems." Computer Methods in Applied Mechanics and Engineering, 22(1), 131–149, 1980

Chaaba, A., Bousshine, L., and de Saxcé, G. "Kinematic limit analysis of nonassociated perfectly plastic material by the bipotential approach and finite element method." Journal of Applied Mechanics. 77 (3), 031016, 2010

Chen, W. F. "Limit Analysis and Soil Plasticity." Elsevier, 1975

Chen, W. F. and Rosenfarb, J. M. "Limit analysis solutions of earth pressure problems." Soils and Foundations, 13(4), 45–60, 1973

Chen, X., Wang, D., Yu, Y., Lyu, Y. "A modified Davis approach for geotechnical stability analysis involving non-associated soil plasticity". Géotechnique 70, 1109–1119, 2020

Coulomb, C. A. "Essai sur une application des règles des maximis et minimis à quelques problèmes de statique relatifs, à l'architecture." Mem. Acad. Roy. Div. Sav., vol. 7, 343–387, 1776

Davis, E. H. "Theories of plasticity and the failure of soil masses." In Soil mechanics: selected topics (ed. I. K. Lee), 341–380. London: Butterworth, 1968

Drescher, A. and Detournay, E. "Limit load in translational failure mechanisms for associative and non-associative materials." Géotechnique, 43, No. 3, 443–456, 1993

Drucker, D. C. and Prager, W. "Soil mechanics and plastic analysis or limit design." Quarterly of Applied Mathematics, 10(2), 157–165, 1952

Drucker, D.C., Prager, W., and Greenberg, H.J. "Extended limit design theorems for continuous media." Quart. Appl. Math. 9(4), 381–389, 1952

Griffiths, D. and Marquez, R., "Three-dimensional slope stabilityanalysis by elastoplastic finite elements." Géotechnique 57 (6), 537–546, 2007

Gvozdev, A. A. "The determination of the value of the collapse load for statically indeterminate systems undergoing plastic deformation." (in Russian). In Conference on Plastic Deformations 1936, Galerkin BG (ed.). Akademia Nauk SSSR: Moscow and Leningrad, 1938; 19–38, 1936

Hill, R. "The Mathematical Theory of Plasticity." Oxford University Press, 1951

Hoek, E., and Brown, E. "Empirical strength criterion for rock masses." J. Geotech. Eng. Div. 106, 1013–1035, 1980

Hoek E., Carranza-Torres C., and Corkum B. "Hoek-Brown failure criterion-2002 edition." Proceedings of NARMS-Tac. 1:267–273, 2002

Hoek, E. and Brown, E. "The Hoek-Brown failure criterion and GSI – 2018 edition." J. Rock Mech. Geotech. Eng. 11(3):445–463, 2019

Huber, M. T. "Specific work of strain as a measure of material effort." Czasopismo Techniczne, 22, 81-88, 1904

Janbu, N. "Earth pressures and bearing capacity calculations by generalized procedure by slices." Proc. 4th Int. Conf Soil Mech., London 2, 207-212, 1957

Josselin de Jong, G. "Lower bound collapse theorem and lack of normality of strainrate to yield surface for soils." IUTAM Symp. Rheology and Soil Mechanics, Kravtchenko, J. and Sirieys, P.M. eds., Grenoble, 69-78, 1964

Kim, Y. S. and Michalowski, R. L. "Moment load impact on resistance of foundation soils to seismic loads." Comput Geotech 172, 106405, 2024

Koiter, W.T. "General theorems for elastic-plastic solids." Sneddon I.N., Hill R. (Eds.), Progress of Solid Mechanics, pp. 167-221, 1960

Kumar, P. "Shear failure envelope of Hoek-Brown criterion for rock mass." Tunn Undergr Space Technol. 13(4):453–458, 1998

Lade, P. V. "Triaxial Testing of Soils." Wiley-Blackwell. ISBN-13: 978-1-119-10662-3, 2016

Lee, K. L. and Seed, H. B. "Drained strength characteristics of sands." Journal of the Soil Mechanics and Foundations Division, ASCE, 93(SM6), 117–141, 1967

Lyamin, A. V. and Sloan, S. W. "Lower bound limit analysis using nonlinear programming." International Journal for Numerical Methods in Engineering, 55(5), 573–611, 2002a

Lyamin, A. V. and Sloan, S. W. "Upper bound limit analysis using linear finite elements and nonlinear programming." International Journal for Numerical Methods in Engineering, 55(5), 613–646, 2002b

Makrodimopoulos, A. and Martin, C. M. "Lower bound limit analysis of cohesive-frictional materials using second-order cone programming." International Journal for Numerical Methods in Engineering, 66(4), 604–634, 2006

Martin, C. "Exact bearing capacity calculations using the method of characteristics." Proc. IACMAG. Turin 11, 441–450, 2005

Melan, E. "Der spannungsgudstand eines Henky-Mises schen Kontinuums bei Verlandicher Belastung." Sitzungberichte der Ak Wissenschaften Wien (Ser 2A). 147, 73, 1938

Michalowski, R. L. "Three-dimensional analysis of locally loaded slopes." Géotechnique 39, No. 1, 27-38, 1989

Michalowski, R. L. "Stability of slopes: limit analysis approach." Rev. Engng Geol. 10, 1995

Michalowski, R.L. "Limit Analysis and Stability Charts for 3D Slope Failures." J. Geotech. Geoenviron. Eng. 136 (4), 583–593, 2010

Michalowski R. L. and A. Drescher. "Three-Dimensional Stability of Slopes and Excavations." Géotechnique 59 (10): 839–850, 2009

Michalowski, R.L. and Park, D. "Three-dimensional ridge collapse mechanism for narrow soil slopes." Int. J. Numer. Anal. Meth. Geomech. 45 (13), 1972–1987, 2021

Michalowski, R.L. and You, L. "Non-symmetrical limit loads on strip footings." Soils Found. 38 (4), 195–203, 1998

Mohr, O. "Welche Umstände bedingen die Elastizitätsgrenze und den Bruch eines Materials" Zeitschrift des Vereins Deutscher Ingenieure, 44, 1524-1530, 1900

Morgenstern, N.R. and Price, V. E. "The analysis of the stability of general slip surfaces." Géotechnique 17 (1): 79–93, 1967

Mroz, Z. "Non-associated flow laws in plasticity." Journal of the Mechanics and Physics of Solids, 11(3), 163-175, 1963

Palmer, A. C. "A limit theorem for materials with nonassociated flow laws." J. Me´canique 5, No. 2, 217–222, 1966

Pastor, J. and Turgeman, S. "Mise en œuvre numérique des méthodes de l'analyse limite pour les matériaux de von Mises et de Coulomb standards en déformation plane." Mechanics Research Communications, 3, 469-474, 1976

Prager, W. "An introduction to plasticity." Addison-Wesley, Reading, Massachusetts, U.S.A, 1959

Prandtl, L. "Über die härte plastischer körper." Nachrichten von der Gesellschaft der Wissenschaften zu Göttingen, Mathematisch-Physikalische Klasse, 1920, 74-85, 1920

Radenkovic, G. " Limit analysis of structures of perfectly plastic material with non-associated flow law." Journal of the Mechanics and Physics of Solids, 10(4), 255-262, 1962

Roscoe, K. H. and Burland, J. B. "On the Generalized Stress-Strain Behaviour of Wet Clay." In: Engineering Plasticity, Cambridge, 535-609, 1968

Roscoe K. H., Schofield A. N. and Wroth C. P. "On the yielding of soils." Géotechnique, 8:22–53. 1958

Saint-Venant, A. J. C. B. "Memoire sur la torsion des prismes avec des considerations sur leur flexion." Mémoires présentés par divers savants à l'Académie des Sciences, 14(2), 233-560, 1870

Salençon, J. and Pecker, A. "Ultimate bearing capacity of shallow foundations under inclined and eccentric loads. Part I: purely cohesive soil. " Eur. J. Mech., Series A Solids 14 (3), 349–375, 1995

Saxcé, G. and Bousshine, L. "Limit analysis theorems for implicit standard materials: Application to the unilateral contact with dry friction and the non-associated flow rules in soils and rocks." International Journal of Mechanical Sciences, 40(4), 387–398, 1998

Schofield, A. N. and Wroth, C. P. "Critical state soil mechanics." London, UK: McGraw-Hill. 1968

Sloan, S. W. "Lower bound limit analysis using finite elements and linear programming." International Journal for Numerical and Analytical Methods in Geomechanics, 12(1), 61–77, 1988

Sloan, S. W. "Upper bound limit analysis using finite elements and linear programming." International Journal for Numerical and Analytical Methods in Geomechanics, 13(3), 263–282, 1989

Sloan, S. W. "Geotechnical stability analysis." Géotechnique, 63(7), 531-572, 2013

Soubra, A. H. "Static and seismic earth pressure coefficients on rigid retaining structures." Can. Geotech. J., 37, 463–478, 2000

Sokolovskii, V. V. "Statics of Granular Media." Pergamon Press, 1965 (First edition published in Russian in 1943)

Taylor, D. W. "Stability of earth slopes." J. Boston Soc. Civil Eng., 24(3). Reprinted in: Contributions to Soil Mechanics 1925 to 1940, Boston Society of Civil Engineers, 337–386, 1937

Tresca, H. "Memoire sur l'écoulement des corps solides soumis à de fortes pressions." Comptes Rendus de l'Académie des Sciences, 59, 754-758, 1864

Tschuchnigg, F., Schweiger, H.F., and Sloan, S.W. "Slope stability analysis by means of finite element limit analysis and finite element strength reduction techniques. Part I: Numerical studies considering non-associated plasticity." Comput Geotech 70, 169–177, 2015

Von Mises, R. "Mechanik der festen Körper im plastisch-deformablen Zustand." Nachrichten von der Gesellschaft der Wissenschaften zu Göttingen, Mathematisch-Physikalische Klasse, 582-592, 1913

Wood D. M., "Soil Behaviour and Critical State Soil Mechanics." Cambridge Press, 1990

Wang, D., Chen, X., Yu, Y., Jie, Y., and Lyu, Y. "Stability and deformation analysis for geotechnical problems with nonassociated plasticity based on second-order cone programming." Int. J. Geomech. 19 (2), 04018190, 2019